



**Institute for Water
and Energy Sciences
(incl. Climate Change)**



**PAN-AFRICAN UNIVERSITY
INSTITUTE FOR WATER AND ENERGY SCIENCES
(including CLIMATE CHANGE)**

Master Dissertation

**Submitted in partial fulfillment of the requirements for the Master degree in
CLIMATE CHANGE ENGINEERING**

Presented by

Ricardo da Crescência MAPULENDE

TITLE :

**Annual Trend and Interactions between the Ozone Layer, Vegetation Cover, and
Climate in Africa - Insights from 2003 to 2023 Reanalysis Data**

Defended on 15/04/2025 Before the Following Committee:

Chair	Tatiana G. Grandón, Dr.	NTNU, Germany
Supervisor	Abdeslam Megnounif, Prof.	University of Tlemcen, Algeria
External Examiner	ANABELLA FERRAL, Dr.	Instituto Gulich, Argentina
Internal Examiner	Bedrane Sumeya, Prof.	University of Tlemcen , Algeria

**Annual Trend and Interactions between the Ozone Layer, Vegetation
Cover, and Climate in Africa - Insights from 2003 to 2023 Reanalysis Data**

Approval page

Statement of the Author

I, Ricardo da Crescencia MAPULENDE, declare that this master's thesis is my independent research and has not been wholly or in part presented in this university or any other university for the award of a degree, grant, or publication purpose. I also declare that all information and materials from other works presented here have been fully cited and referenced following academic rules and ethics.

STUDENT: RICARDO DA CRESCÊNCIA MAPULENDE

Signature:



Date: 15-04-2025

SUPERVISOR

This is to certify that this thesis was prepared by Ricardo da Crescência MAPULENDE (PAUWES/2023/MCCE14) under my supervision for an M.Sc. degree at the Pan African University of Water and Energy Sciences (Including Climate Change) jointly with the University of Tlemcen, Algeria.

Supervisor: Prof. Abdeslam Megnounif

Signature:



Date: 15-04-2025

Biographical Sketch

Ricardo da Crescencia MAPULENDE is a young and motivated professional pursuing a Master's degree in Climate Change Engineering from the Pan African Institute of Water and Energy Sciences, including Climate Change (PAUWES), and holds a BSc degree in Physical Oceanography from the University of Eduardo Mondlane (UEM). He is determined to improve his skills and promote prosperity through his work while protecting the environment, tackling climate change problems, and saving lives. He is a quick, adaptable learner with excellent organizational, communication, accountability, and analytical skills.

Ricardo has gained valuable work experience at the National Institute of Meteorology, where he acquired expertise in climate data observation, management and storage, and the preparation of climate information for daily forecasts. Additionally, he has worked as a hydrographer trainee at the Port of Maputo, where he developed skills in team management and coordination, project management, dredging planning, and execution. He also acquired knowledge of marine safety principles and interpersonal working skills that are crucial for life.

Acknowledgements

I want to express my sincere acknowledgements to the African Union Commission for awarding me this prestigious scholarship and to PAUWES for facilitating this program. I also express my sincere gratitude to Professor Abdesselam Megnounif, my supervisor, for his mentorship and guidance throughout my research. Professor Megnounif's help has been fundamental to the success of this research.

I am grateful to Professor Avelino Landa from Eduardo Mondlane University for his mentorship and guidance prior to and during PAUWES.

I express my gratitude to my Family, parents, and siblings for their constant encouragement during this period of my life, which culminated in the preparation of the present thesis. I am grateful to my father Sebastião Mapulende, my mother Crescencia Fernando, my pastor Pedro Matsimbe, and my mentor mother Julia Cumbana for their constant care and guardianship even in distant communications. I thank my sister Lucrência Mapulende for her exceptional care during my stay in Algeria.

I thank my fellow PAUWES scholars for this excellent companionship during these two years. I especially thank Mfundo, Maziya, Gobosaone Mokokwe, Ahmed Olajowon, Ezira Mbalebulha, and all who contributed for an efficacious engagement in Algeria.

I am grateful to the Tlemcen community for the excellent fraternity that has been available, which has enabled more significant results. I thank Father John, my friends Maryann Kirumba, Abbey Lowemba, Vianney and Mark Avin, Admire Tadiwanashe. I Thank my friends from the Mozambican community in Algeria, Naira Boa, John Chungamu, Juben Kandja, Niclasse Bondo, Anita Paixao, for the fraternal experience we had.

I express my gratitude to all my friends and family who directly or indirectly have contributed for the success of my journey at PAUWES in Algeria.

Thank you!

Abbreviations and Acronyms

°C	Degrees Celsius
3CS	Copernicus Climate Change Service
Å	Angstrom
ABCs -	Atmospheric Brown Clouds
AMSU-B -	Advanced Microwave Sounding Unit-B
AOD_550	Aerosol Optical Depth at 550 nm
AOD_865	Aerosol Optical Depth at 865 nm
BDC	Brewer and Dobson Circulation
BDRF	Bidirectional Reflectance Distribution Function
Br	bromine
CAMS -	Copernicus Monitoring Service
CC -	Climate Change
CDR	Climate Data Record
CFCs	chlorofluorocarbons
CH4	methane
CH4	Methane
Cl	chlorine
CLIMCAPS	Comprehensive Quality Control Gridded Monthly
CLMS	Copernicus Global Land Monitoring Service
CO	carbon monoxide
CO ₂	Carbon Dioxide
co22_vmr_uppertrop	CO ₂ Volume Mixing Ratio in the Upper Troposphere
COS	carbonyl sulfide
CS ₂	carbon disulfide
CT	chemical transport
DMS	dimethyl sulphide
DMSP	Defense Meteorological Satellite Program
DU	Dobson Units
EAC4	CAMS global reanalysis
ECDGJRC	European Commission Directorate-General Joint Research Centre

ECMWF	European Centre for Medium-Range Weather Forecasts
EGG4	CAMS Greenhouse Gases Reanalysis
ENSO	El-Nino Southern Oscillation
GAM	Generalized Additive Model
GBOV	Ground Based Observation for Validation
GEWEX	Global Energy and Water Exchanges
GHGs	greenhouse gases
GMS	Geostationary Meteorological Satellite
GOES	Geostationary Operational Environmental Satellite
GPCP	Global Precipitation Climatology Project
H₂S	hydrogen sulfide
halons	halogenated hydrocarbons
IFS	ECMWF Integrated Forecasting System
IR	Infrared radiation
ITCZ	Intertropical Convergence Zone
ITD	Intertropical Discontinuity
kyr	thousand years ago
LGM	Last Glacial Maximum
LULCC	Land Use and Land Cover Change
Ma	million years ago
Meteosat	EU Meteorological Satellite
MLR	Multivariate Linear Regression
mm/year	Millimeters per year
MOCAGE	Large-Scale Atmospheric Chemistry Model (Modèle de Chimie Atmosphérique à Grande Échelle)
MOZART	Model for Ozone And Related chemical Tracers
N₂O	nitrous oxide
NDVI	Normalized Difference Vegetation Index
NOAA	USA National Ocean and Atmospheric Administration
NO_x	Nitrogen Oxides
ODS	ozone-depleting substances
PC	Principal component
PCA	Principal Component Analysis

ppm	parts per million
Si	Silicon
SNDRAQIL3MCCP_2	dataset (SIPS: AQUA AIRS IR-only Level 3 CLIMCAPS Version 2)
SO2	Sulfur dioxide
SO4	sulfate
SSM/I	Sensor Microwave/Imager
SST	Sea Surface Temperature
TCO	Total Column Ozone
UTLS	Upper troposphere lower stratosphere
UV	Ultraviolet radiation
VIF	Variance Inferred Factor
VOCS	Volatile Organic Composts
WCRP	World Climate Research Program
XCH4	Mean molar fraction of Methane (CH4)
XCO2	Mean molar fraction of Carbon Dioxide (CO2)

Table of Contents

Approval page.....	i
Statement of the Author	ii
Biographical Sketch.....	iii
Acknowledgements.....	iv
Abbreviations and Acronyms.....	v
Table of Contents	viii
List of Tables.....	xi
List of Figures	xii
Abstract.....	xiv
1. Introduction.....	1
1.1. General Background	1
1.2. Problem Statement.....	2
1.3. Objectives	4
2. Climate Change in Africa – A review from past research.....	5
2.1. Introduction.....	5
2.1.1. Objective of the Session.....	5
2.2. Atmospheric Composition and Interaction with CC.....	5
2.2.1. The Crescent Release of GHGs and Climate Change.....	5
2.2.2. Ozone Depletion and Climate Change.....	9
2.2.3. Atmospheric Aerosols and Climate Change	10
2.2.4. Land Use and Land Cover Change and Climate Change	13
2.3. Review of past and Future Climate Change in Africa	14
2.3.1. Multidecadal climate change and variability	14
2.3.2. African paleoclimate	15
2.3.3. African GHG Emissions during the pre-and post-industrial era.....	21

2.3.4.	Distribution and variability of Aerosols over Africa.....	23
2.3.5.	Temporal and Spatial Variability of Ozone in Africa.....	24
2.3.6.	Temporal and spatial variability of land use land cover change (LULCC) in Africa	26
2.4.	Summary.....	28
3.	Data and Methodology.....	29
4.	Data and Methodology.....	29
4.1.	Data.....	29
4.1.1.	Global Precipitation Climatology Project (GPCP)	32
4.1.2.	Copernicus Atmosphere Monitoring Service (CAMS) global reanalysis (EAC4)	33
4.1.3.	Normalized Difference Vegetation Index (NDVI).....	34
4.1.4.	Greenhouse Gases – Methane (CH ₄) and Carbon Dioxide (CO ₂).....	36
4.2.	Data preprocessing.....	37
4.3.	Spatial Variability, Trends, and Homogeneity	37
4.4.	Statistical Modelling	38
4.4.1.	Multivariate Linear Regression (MLR)	39
4.4.2.	Principal Component Analysis (PCA)	39
4.4.3.	Generalized Additive Model (GAM).....	39
4.5.	Modelling variables and Training and Validation datasets	40
5.	Results and Discussions.....	41
5.1.	Results Description	41
5.1.1.	Estimation of CO ₂ and CH ₄ total column mean molar fraction	41
5.1.2.	Descriptive Summary of the Dataset	42
5.1.3.	Spatial Variability.....	49
5.1.4.	Trend Analysis and Homogeneity for Temperature, Rainfall, TCO, and NDVI	54
5.1.5.	Multivariate Linear Regression.....	58

5.1.6.	Principal Component Analysis.....	63
5.1.7.	Generalized Addictive Model	65
5.2.	Summary and Discussion.....	71
5.2.1.	Description of the dataset.....	71
5.2.2.	Spatial Variability.....	72
5.2.3.	Trend Analysis and Homogeneity for Temperature, Rainfall, TCO, and NDVI 74	
5.2.4.	Statistical Modeling: Multivariate Linear Regression; Principal Component Analysis; Genialized Additive Models.	76
6.	Conclusions and Recommendations	79
7.	References.....	81

List of Tables

Table 1. Eith of the major GHGs and their Radiative potential from historical data (Tuckett, 2021)	8
Table 2. Most abundant tropospheric aerosols, their sources, interactions, and global emissions estimates (Haywood, 2021)	11
Table 3. Summary of the dataset and sources used for the present research	31
Table 3. Correlation coefficients for the variables analyzed to Temperature, Precipitation, TCO (O3), and NDVI	59
Table 4. Multivariate Linear Regression Coefficients for Temperature, Precipitation, TCO, and NDVI Models.....	62
Table 5. Loading of Principal Components for the Variables Examined in This Study	64
Table 6. Summary of the GAM Model for Temperature. The smoothing function used was Thin Plate Regression Splines (TPRS).....	66
Table 7. Summary of the GAM Model for Precipitation. The smoothing function used was Thin Plate Regression Splines (TPRS).....	67
Table 8. Summary of the GAM Model for Ozone. The smoothing function used was Thin Plate Regression Splines (TPRS).....	68
Table 9. Summary of the GAM Model for NDVI. The smoothing function used was Thin Plate Regression Splines (TPRS).....	69

List of Figures

Figure 1. Illustration of the Brewer-Dobson circulation and representation of vertical ozone distribution (averaged for each zone) in March 2004 (“Optical Spectrograph and InfraRed Imager System (OSIRIS)” measurements from the Odin satellite). The black arrays represent the Brewer-Dobson circulation. Source: (Dameris, 2010).....	9
Figure 2. Processes governing aerosol supply, formation, transport, and removal from the stratosphere (Kremser et al., 2016)	13
Figure 3. Schematic representation of Wind patterns and pressure systems over Africa, highlighting the seasonality of wind. Dotted lines represent the ITCZ and the dashed lines indicate the Congo Air Boundary. Source: (Gasse, 2000).	18
Figure 4. Tentative representation for the African Atmospheric circulation, during the late Pleistocene (20 – 12 kyr). Dark shading represents areas that had more rainfall than today, and light shading areas represent areas with less precipitation than today. Inset lines represent the position of the ITCZ in winter and summer. Source: (S. E. Nicholson & Flohn, 1980).	19
Figure 5. Tentative reconstruction of wind patterns during the Early to mid-Holocene (10 – 8 kyr). Dark shading represents areas that had more rainfall than today, and light shading areas represent areas with less precipitation than today. The dashed line represents the position of the ITCZ in summer and winter. Source: (S. E. Nicholson & Flohn, 1980).	20
Figure 6. Tentative reconstruction of wind patterns during the mid-Holocene (6.5 – 4.5 kyr). Dark shading represents areas with more rainfall than today, and hatching represents the areas drier than previous periods but wetter than today. The dashed line represents the position of the ITCZ in summer and winter. Source: (S. E. Nicholson & Flohn, 1980).	21
<i>Figure 7. Flow chart of the methodology used for the present research. The trend analysis was performed only on the 4 variables whose interactions are spotted in this research (Temperature, Precipitation, TCO, and NDVI.</i>	30
Figure 8. Training results for different linear regression polynomial models, with the biquintic model (e) showing the best performance in estimating CO ₂ , were used for the analysis in this work.	42
Figure 9. Study Area Regional Boundaries for Dataset Description	43
Figure 10. Provide a general description of the dataset in the Northern Region. The signs of U and V wind represent the direction of the wind, and the module represents the strength of that component. For the U wind, the negative sign represents the westward winds, and the positive	

sign represents the eastward winds. For the V wind, the negative sign represents the southward wind, and the positive sign represents the northward wind.45

Figure 11. Provide a general description of the dataset in the Central Region. The signs of U and V wind represent the direction of the wind, and the module represents the strength of that component. For the U wind, the negative sign represents the westward winds, and the positive sign represents the eastward winds. For the V wind, the negative sign represents the southward wind, and the positive sign represents the northward wind.47

Figure 12. Provide a general description of the dataset in the Southern Region. The signs of U and V wind represent the direction of the wind, and the module represents the strength of that component. For the U wind, the negative sign represents the westward winds, and the positive sign represents the eastward winds. For the V wind, the negative sign represents the southward wind, and the positive sign represents the northward wind.49

Figure 13. Mean annual values for the variables analyzed are presented. A unique analysis is conducted on the Mean Wind Speed and Direction, where the wind speed is calculated using the formula for vector direction resultant: $w = \sqrt{u^2 + v^2}$, where w represents the wind speed, u is the U wind component, and v is the V wind component (j, in the Figure 13-continued). ...52

Figure 14. Trend Analysis for Annual Temperature, Precipitation, TCO, and NDVI. For the homogeneity test, the gray color on the map represents homogeneous series that do not exhibit a breakpoint or loss of stationarity.55

Figure 15. Performance results for Temperature, Precipitation, O3 and NDVI MLR modes. 63

Figure 16. Performance Results for Temperature, Precipitation, O3, and NDVI GAM models.70

Abstract

The present research examines the annual trends and interactions among the ozone layer, vegetation cover, and climate variables in Africa from 2003 to 2023 using reanalysis data. The aim was to illustrate the temporal and spatial variability of total column ozone (TCO), the normalized difference vegetation index (NDVI), temperature, and precipitation; analyze their yearly trends; and assess the statistical significance of various factors influencing their variability. Our methodology utilized descriptive statistics and trend analysis—specifically, the Mann-Kendall test, Sen's slope, and Buishand test—along with statistical modeling techniques, including multivariate linear regression, principal component analysis, and generalized additive models. The results revealed a widespread warming trend across the continent, with significant temperature increases noted in 59.21% of Africa, particularly after 2013. Precipitation trend results were more complex, reflecting both upward and downward changes that highlight regional climate variability. The Total Column Ozone (TCO) exhibited a generally positive trend, indicating a potential recovery of the ozone layer, likely linked to the enforcement of the Montreal Protocol. NDVI analysis revealed a varied pattern of vegetation changes, with both gains and losses observed throughout the continent. Statistical modeling results indicated significant correlations between climate factors and the target variables. Multivariate linear regression highlighted the roles of atmospheric dynamics and air quality in shaping regional temperatures. At the same time, principal component analysis (PCA) consolidated complex interactions, emphasizing the impacts of air quality, temperature, atmospheric composition, and vegetation. Generalized additive models (GAMs) elucidated non-linear relationships by identifying the influences of latitude, wind patterns, and greenhouse gases on temperature, precipitation, and ozone levels. These findings highlight the complex relationships between climate, vegetation, and ozone dynamics in Africa, offering valuable insights into climate modeling and future climate change projections. They also emphasize the necessity for continuous monitoring and improved modeling methods.

1. Introduction

1.1. General Background

The interactions between the ozone layer, vegetation cover, and climate are complex and multifaceted, influencing regional and global environmental conditions. The total column ozone (TCO) specially the stratospheric ozone, plays a crucial role in protecting life on earth by absorbing harmful ultraviolet radiation (Dameris, 2010). Recent developments highlight spatial and temporal increase in TCO concentrations linked to meteorological and socio-economic factors (P. Zhou et al., 2022), influenced by both natural atmospheric processes and anthropogenic activities that can lead to changes in precursor emissions and subsequent ozone formation (Rupakheti et al., 2018a).

Furthermore, tropospheric ozone, a significant air pollutant and greenhouse gas, plays a crucial role in affecting vegetation by inhibiting photosynthesis and altering stomatal conductance, impacting evapotranspiration and climate conditions (Lu et al., 2019; X. Zhou et al., 2024). High level pollution can lead to warmer and drier conditions, as observed in regions like eastern United States and China, where increased surface temperatures and altered heat dynamics have been observed (X. Zhou et al., 2024).

Vegetation is both sink and ozone precursor, including hydrocarbons and nitrogen oxides, and its interactions with ozone can lead to significant changes in atmospheric chemistry and climate dynamics (Simpson et al., 2014). The impact of the ozone layer on vegetation is further complicated by factors such as nitrogen enrichment and climate change, which can exacerbate the effects of ozone on plant growth and carbon allocation (Mills et al., 2016). Furthermore, the vegetation feedback process is influenced by innumerable factors comprehending environmental conditions, highlighting the need for more comprehensive studies to understand these interactions (Mills et al., 2016; Savi et al., 2020).

Climate change influences ozone levels through various mechanisms, comprehending changes in natural precursor emissions, chemical kinetics, and atmospheric transport patterns (Lu et al., 2019), leading to significant regional and global variations in ozone levels, with potential implications for air quality, climate, and ecosystem health (Lu et al., 2019; Simpson et al., 2014). The interplay between ozone and climate is further complicated by the ongoing shifts in ozone precursors emissions and the effects of greenhouse gases, which can alter atmospheric circulation patterns and ozone distribution (Ball et al., 2020; Cooper et al., 2020).

Actual records show recovery and trends on the ozone layer to be influenced by various factors, including the implementation of international agreements such as the Montreal Protocol, which has led to positive trends in the ozone recovery at mid-latitudes (Y. Li et al., 2020; Rupakheti et al., 2018). However, the recovery is not uniform across all the regions globally, with some regions experiencing significant positive trends while others show negative or insignificant changes (Coldewey-Egbers et al., 2022). Therefore, the interplay between ozone trends and climate enhanced through the influence of greenhouse gases and atmospheric circulation patterns which can modulate ozone levels and distribution (Dietmuller et al., 2021; J. Zhang et al., 2019).

Climate change, one of the significant threats to human life, is expected to increase ozone concentration in Africa, especially in urban and biomass-burning areas, due to changes in atmospheric chemistry and emission, in a process called the ozone climate penalty (F. Brown et al., 2022). In South Africa, variations in stratospheric ozone can influence surface air temperature and precipitation, with increasing ozone leading to higher temperature and reduced rainfall (Manatsa & Mukwada, 2019). Across Africa, vegetation dynamics are significantly influenced by climate variability, where increasing temperatures and decreasing rainfall have been observed affecting vegetation greenness and leading to peril of certain plant species (Nooni et al., 2024; Nzabarinda et al., 2021). In East Africa, vegetation trends have complex responses to climate factors, with precipitation having a more significant impact on vegetation than temperature (Kalisa et al., 2019; Xu et al., 2023). In the rangelands, climate change has led to both greening and browning trends, affecting the balance between woody and herbaceous vegetation (D'Adamo et al., 2021). There is a significant positive relationship between vegetation cover and total column ozone in West Africa, suggesting that changes in vegetation can influence ozone levels (Ogunjo et al., 2019). Therefore, deforestation and biomass burning contribute to changes in both vegetation cover and ozone levels, exacerbating climate impacts (Abera et al., 2018; Aghedo et al., 2007).

1.2. Problem Statement

Several studies have explored the relationship between vegetation cover and total column ozone (TCO) in Africa. Ogunjo et al. (2019) focusing on West Africa found a significant positive linear relationship between the Normalized Difference Vegetation Index (NDVI) and TCO, suggesting that activities such as bush burning and deforestation contribute to increased ozone levels and global warming. Other studies examining the influence of Intertropical

Discontinuity (ITD) on TCO variation over West Africa, reveal that regions north of the ITD have higher TCO concentrations, particularly during the wet months of June to August (Arowolo & Oluleye, 2022).

Research in different parts of Africa has shown that climate factors impact significantly vegetation dynamics. Kalisa et al. (2019) analyzing the impact of climate on vegetation dynamics from 1982 to 2015, found a positive trend in NDVI before 1998 followed by a negative trend, indicating complex responses of vegetation to climate and non-climate drivers. The study found that the correlation between NDVI and precipitation was stronger than with temperature, highlighting the importance of precipitation in vegetation growth. Similarly, a study on African rangelands identified climate change as a dominant driver of vegetation dynamics, with greening trends associated with increased woody cover and browning trends linked to a decline in woody cover (D'Adamo et al., 2021). Furthermore, increasing temperatures and decreasing rainfall influenced negatively vegetation cover in Africa leading to the extinction of many plant species affecting environmental sustainability (Nzabarinda et al., 2021).

Other studies, on the variability of TCO over West Africa and interplay with weather, observed a seasonal distribution with wet seasons observing maximum ozone levels and dry seasons observing minimum levels (Oluleye & Okogbue, 2013). Laban et al. (2020) conducted statistical modeling of surface ozone variability factors in continental South Africa identifying temperature and relative humidity as the primary drivers of ozone variability. Still, in South Africa, studies have shown a positive trend in tropospheric ozone, influenced by industrial pollution and biomass burning, while stratospheric ozone levels have decreased (Bencherif et al., 2020; Clain et al., 2009). An old study by Combrink et al. (1995) found that the relationship between the free tropospheric and the total column ozone in South Africa indicated that photochemical ozone production contributed significantly to the background ozone levels, with seasonal variations consistent across the region.

However, studies presenting a holistic view of the climate patterns and variabilities across the continent and related to the ozone and vegetation variability are still few, and references are difficult to find. The purpose of this research is to assess the relationships between the ozone layer (TCO), vegetation cover, and climate variability in Africa. Increasing knowledge in this field holds significant promises for enhancing the accuracy and skill of climate model predictions and forecasts. By deepening our understanding of how the ozone layer and

vegetation influence atmospheric dynamics, temperature distribution, and weather patterns, this study can provide crucial data for refining climate models. Improved models will offer more reliable information, which is essential for developing effective adaptation strategies and preparedness plans. This, in turn, enables policymakers, communities, and industries to take proactive, climate-resilient actions that mitigate risks and capitalize on opportunities in a changing climate.

1.3. Objectives

General Objective:

- Analyze the annual trends and statistical relationships between Ozone Layer, vegetation cover, and climate in Africa from 2003 to 2023

Specific Objectives:

- Describe the variability of total column ozone, normalized difference vegetation index, temperature, and precipitation from 2003 to 2023.
- Analyze the annual trend of total column ozone, Normalized Difference Vegetation Index, temperature, and precipitation from 2003 to 2023.
- Determine the statistical importance of different independent variables on total column ozone, normalized difference vegetation index, temperature, and precipitation variability from 2003 to 2023.

2. Climate Change in Africa – A review from past research

2.1. Introduction

Climate Change (CC) has been a subject of discussion in many fields of expertise, from the geologic point of view to physics, anthropology, sociology, and psychology. This shows its interconnectedness with the evolution of life and society throughout time and how the different climates observed on Earth influenced the evolution of human beings in the throughout the ages (Baarsch et al., 2020; Collins, 2011; Henderson et al., 2017; Holmgren & Öberg, 2006; Hulme et al., 2001; Mccann, 1999; Ofori et al., 2021). Important emphasis has been made noticeable since the beginning of the last century when CC has been the center of environmental and sustainability development research (Conway, 2011). This started at the beginning of the Industrial Revolution, which brought the development of ozone-depleting substances (ODS) and the release of greenhouse gases (GHGs) into the atmosphere. The industrial revolution came with the release of GHGs, which started some 160 years ago, and ODS, some 35 years ago, accounting for the major contributors to CC and global temperature increase (Ramanathan et al., 1987; Ramanathan & Feng, 2009). This was enhanced by the releasing of aerosols and dust into the atmosphere which gave negative feedback on the increasing atmospheric temperature over the years (Collins, 2011; Hulme et al., 2001; S. E. Nicholson, 2000, 2001a). These phenomena of CC have impacted human life worldwide, and societies have had to adapt and mitigate them throughout the years, with lots of economic and infrastructure investment and losses.

2.1.1. Objective of the Session

This session aims to provide an in-depth review of previous studies on stratospheric ozone depletion and recovery, GHGs, Aerosols, and Changes in Land Cover and Land Use influences in Climate Change and Variability in Africa.

2.2. Atmospheric Composition and Interaction with CC

2.2.1. The Crescent Release of GHGs and Climate Change

Greenhouse gases (GHGs) originate from natural processes such as the decomposition of organic materials, and volcanic eruption. They also have origin from human activities, such as burning fossil fuels, agriculture, and household activities. GHGs compose a group of gases that form the greenhouse effect, which in its normal course serves as a climate stabilizer on the earth preventing the earth from heating up in the presence of solar radiation or from cooling

drastically when it's not available, thereby balancing the earth's energy budget. With the rapid progress of industrialization during the last century leading to the burning of fossil fuels, the amount of GHGs in the atmosphere has been increasing significantly resulting in global warming and climate change. Amongst the most powerful GHGs are carbon dioxide (CO₂), methane (CH₄), nitrous oxide (N₂O), and chlorofluorocarbons (CFCs). CO₂ and CH₄ make the most impacting GHGs recently, due to their high concentration and radiative effect respectively.

The GHG effects extend to chemical processes in both the troposphere and stratosphere. For instance, the crescent release of CH₄ can contribute to the indirect formation of tropospheric ozone (a pollutant gas that contains greenhouse effect in this region of the atmosphere), through chemical processes involving Nitrogen Oxides (NO_x), volatile organic compounds (VOCs), and sunlight (Ramanathan et al., 1987).

GHG release into the atmosphere has shown to have a great feedback mechanism both in warming and cooling the earth's surface, with the earlier carrying more impact than the latter (Ramanathan & Feng, 2009; Tuckett, 2021). Positive feedback mechanisms have been observed in many contexts, for instance, warming due to GHG causes ice melting which reduces surface albedo resulting in more climate-raising temperatures (Moore et al., 2015; Ramanathan et al., 1987; Tuckett, 2021). The melting of ice bodies such as permafrost results in the release of age-long stored methane, which is a potent GHG with a radiative potential as much as twice the radiative forcing of CO₂. Water vapor constitutes a potent GHG with positive feedback, along with ocean warming which results in ocean acidification and acidic rains which result in biodiversity and CO₂ sequestration reduction (Tuckett, 2021). These effects are counterposed by the cloud formation, and release of some aerosols that have cooling impacts that range from local to regional impact (Ramanathan & Feng, 2009). Atmospheric dynamic processes contribute to the transport of air aerosols in a process that forms Atmospheric Brown Clouds (ABCs) causing surface dimming and atmospheric heating (Ramanathan & Feng, 2009). According to (Ramanathan & Feng, 2009), this process is recurrent in regions such as South Asia and North Africa where in the last decade the large north-south gradient in the ABC dimming had a cooling impact on sea surface temperatures and land-ocean surface temperature gradients resulting in deceleration of the monsoon circulation and reduced precipitation over the continents.

GHGs have different radiative forcings and lifespan in the atmosphere, thus recovery from the residual gases available in the atmosphere today even with net zero would still take time up to a century (Tuckett, 2021). Table 1 presents a summary of 8 of the major GHGs their radiative potential/efficiency, concentrations, and lifespan in the atmosphere (Tuckett, 2021). Note that, although the radiative efficiency of other gases such as CH₄ (3.63×10^{-4}) is higher than the one of CO₂ (1.37×10^{-5}), CO₂ outstands all other GHGs due to its concentrations in the atmosphere (407ppmv) a number of times greater than the other GHGs.

Table 1. Eith of the major GHGs and their Radiative potential from historical data (Tuckett, 2021)

Greenhouse gas	CO ₂	CH ₄	N ₂ O	CF ₂ Cl ₂	O ₃	NF ₃	SF ₆	CF ₃ SF ₅
				[all CFCs]				
Concentration (2018) (<i>mmol/mol or ppmv</i>)	407	1.86	0.33	5.0×10^{-4} [8.0×10^{-4}]	c.0.040	c. 1.0 $\times 10^{-6}$	9.6×10^{-6}	c. 2.0×10^{-7}
Change in concentration (1748-2018) (<i>mmol/mol or ppmv</i>)	129	1.14	0.06	5.0×10^{-4} [8.0×10^{-4}]	c.0.015	c. 1.0 $\times 10^{-6}$	9.6×10^{-6}	c. 2.0×10^{-7}
Radiative efficiency, a_o (<i>W/m²/ppbv</i>)	1.37×10^5	3.63 $\times 10^{-4}$	3.00 $\times 10^{-3}$	0.32 [0.20-0.32]	3.33×10^{-2}	0.20	0.57	0.59
Total radiative forcing (<i>W/m²</i>)	2.04	0.51	0.20	0.16 [0.30]	c.0.04	2.0×10^{-4}	5.5×10^{-3}	1.2×10^{-4}
Contribution from long-lived secondary greenhouse gases, excluding ozone, to overall greenhouse effect (%)	66 (58)	16 (15)	6 (6)	5 (5) [10 (9)]	0 (11)	0.006 (0.006)	0.18 (0.16)	0.004 (0.003)
Lifetime, (τ/a or years)	c.50-200	12.4	121	100 [45-1020]	c.days - weeks	500	3200	800
Global warming potential (100 year projection)	1	28	265	10,200 [4660-13,900]	-	16,000	23,500	17,400

2.2.2. Ozone Depletion and Climate Change

Ozone is a substance composed of three atoms of oxygen, organized with 1.26 Å (Angstroms) amongst oxygen atoms, and its cyclical structure is perceptible through absorption at the infrared region (Bocci, 2002) and Ultra-Violet (Dameris, 2010) of the electromagnetic spectrum. Its major concentrations are available in the upper stratosphere, around 10 to 40 km above the earth's surface. The stratospheric ozone, often called the ozone layer, is highly influenced by atmospheric dynamic processes that affect its distribution, in a process called Brewer-Dobson circulation, a large-scale atmospheric circulation in the stratosphere that is responsible for air transport from the tropics to the higher latitudes, characterized by upwelling in the tropics and downwelling in higher latitudes (Minganti et al., 2020; Seviour et al., 2012). The highest concentrations at the equator are found around 40-50 km and at polar regions at around 10km near the ground (Figure 1; Dameris, 2010).

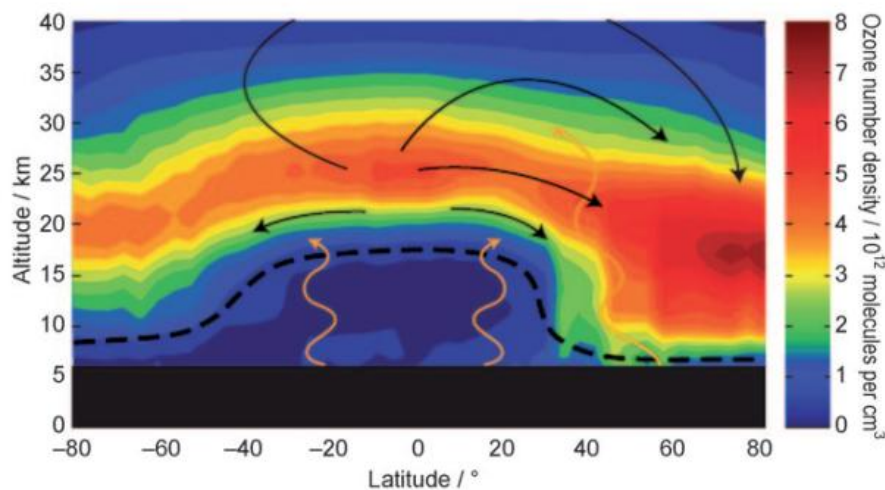


Figure 1. Illustration of the Brewer-Dobson circulation and representation of vertical ozone distribution (averaged for each zone) in March 2004 (“Optical Spectrograph and InfraRed Imager System (OSIRIS)” measurements from the Odin satellite). The black arrays represent the Brewer-Dobson circulation. Source: (Dameris, 2010).

The ozone layer is essential for keeping human life, it is responsible for filtering Ultraviolet (UV) radiation (~ 100–380 nm), especially UV-B (~ 280-320nm) which is harmful to human health, plants, and life in the upper layers of water bodies (Dameris, 2010), reducing immunology, causing skin cancers in humans, and impacting the photosynthesis processes in plants and water life depending on the intensity. The UV absorption impact results in the warming of the upper part of the stratosphere, which in turn results in the stabilization of atmospheric vertical circulation, impacting positively the earth’s climate (Dameris, 2010).

With the discovery and production of ODS between the 1960s and 1980s, substances that contain chlorine (Cl) and bromine (Br) in their composition, the CFCs and the halogenated hydrocarbons (halons), such as methane ethane and their derivatives (Sigmond et al., 2023), the ozone concentrations in the upper stratosphere began to shrink and the Antarctic ozone hole was observed (Dameris, 2010) causing a weakening of the absorption of UV radiation and impacting human health. Other implications of ODS production and industrial use contributed to the formation of ground (tropospheric ozone) which is a potent GHG (Dameris, 2010), as a matter of fact, ODSs themselves carry very high radiative properties, as hundreds as the CO₂ radiative potential (Sigmond et al., 2023). Therefore, efforts to mitigate and phase out all the ODS have been observed since the Montreal Protocol in 1987, however, the effectiveness of its effect remains uncertain (Fang et al., 2019). Thus, further research is needed to determine the spatial and temporal interactions between the O₃ and other climate determinants.

The effects of ODSs on the climate are well-studied and documented. Nonetheless, interactions with other gases such as GHG form a more complex non-linear process that influences the ozone formation/decline due to chemical and physical transport processes (Meul et al., 2015; Zeng et al., 2022). Interactions between GHGs, such as CH₄, have a positive impact on tropospheric and stratospheric ozone formation through its oxidation processes that liberate water that reduces reaction with ODSs reducing availability in the atmosphere (Zeng et al., 2022). CO₂ and N₂O are among the contributors to ozone depletion in the middle stratosphere caused by the catalytic impact of N₂O and the cooling effects of CO₂ in the stratosphere (Zeng et al., 2022). A positive CO₂ impact is shown also in the upper stratosphere, especially in polar regions where the CO₂ cooling impact enhances Ozone formation (Zeng et al., 2022). The impact of non-traditional climate forcings, such as NO_x, VOCs, and carbon monoxide (CO), are potent contributors to ozone formation, mainly in the troposphere, through undergoing photochemical reactions (Zeng et al., 2022). To conclude, GHG interacts with ODS in ozone formation or sinking in nonlinear parameters, where tropospheric and stratospheric interactions air mass circulation play a crucial impact (Bandoro et al., 2018; Langematz, 2018; Meul et al., 2018).

2.2.3. Atmospheric Aerosols and Climate Change

Atmospheric aerosols are a group of particles mixed with atmospheric gases, that mostly reflect the UV and Infrared (IR) radiation to space, contributing to cooling the climate of the Earth (Haywood, 2021; Kremser et al., 2016; Stenchikov, 2021). Their origin, characteristics, and interaction with chemical and physical processes in the atmosphere determine their location

and life duration in the troposphere and stratosphere. Tropospheric aerosols are composed mainly of aerosols supplied by anthropogenic activities such as fossil fuel burning, biomass burning, industrial and agricultural dust, and deforestation, among others, and have their life duration from days to months (Haywood, 2016, 2021). Table 2 presents some of the most common aerosols found in the troposphere, their origin, and their global emission estimates (Haywood, 2021). *Primary* aerosols represent the type of aerosols that are found in the original form of the emission sources, while *secondary* aerosols are formed through interactions with other atmospheric gases and particles (Haywood, 2016, 2021).

Table 2. Most abundant tropospheric aerosols, their sources, interactions, and global emissions estimates (Haywood, 2021)

	Global emission (Tg/yr)	² Burden (mg/m ²)	Primary or secondary	Accumulation or coarse	Anthropogenic sources	Natural sources
Sulfate (as sulfur)	98–127 [1]	1.0 ± 0.0	S	A/C	Fossil fuel burning, biomass burning, smelters	Dimethyl sulfide from plankton, SO ₂ from volcanoes
Mineral dust	1000–4000 [1]	88.2 ± 7.3	P	C	Industrial and agricultural dust from building and ploughing	Windblown dust from arid regions, and from deserts
Sea salt	1400–6800 [1]	50.3 ± 0.1	P	C	N/A	Breaking waves
Fossil fuel black carbon	3.6–6 [1]	0.5 ± 0.0	P	A	Fossil fuel burning, particularly diesel fuels	N/A
Biomass burning	29–85 [1]	1.8 ± 0.1	P/S	A	Deforestation, agricultural waste, biofuels	Lightning-initiated wildfires
Biogenic carbon	440–720 [1]	2.2 ± 0.0	S	A/C	N/A	Monoterpenes, isoprene
Fossil fuel organic carbon	~13 [2]	0.4 ± 0.0	P/S	A	Fossil fuel burning	N/A
Nitrate (N)	~80 [3]	0.2 ± 0.0	S	A/C	Mainly in the form NH ₄ NO ₃ from NO _x from fossil fuel burning and NH _x emissions from agriculture	Soils, oceans, lightning

The burdens shown represent a multiyear mean derived from the model, and the ± estimates show the variability in the model and do not represent the full variability of the emissions and intermodel variability. “P” represents primary, while “S” represents secondary aerosols. “A” represents accumulation-mode aerosols, and “C” represents coarse-mode aerosols.

Stratospheric aerosols, such as volcanic ash and black and organic carbon, are mostly available in the atmosphere through natural processes, mostly volcanic eruptions, and forest fires (Kremser et al., 2016; Stenchikov, 2021), while black carbon from fossil fuels burning contributes a percentage more or less than 1% of the total stratospheric aerosols, which are produced through anthropogenic activities and transported to the stratosphere through Upper troposphere lower stratosphere (UTLS) interactions (Kremser et al., 2016). Stratospheric aerosols from volcanic eruption contain a large amount of compost, including carbonyl sulfide (COS), sulfur dioxide (SO₂), short-lived compounds (carbon disulfide (CS₂), dimethyl sulfide (DMS), and hydrogen sulfide (H₂S), and non-sulfate compounds (volcanic ash (composed of silicon (Si), glass, crystals, and gas bubbles), and black carbon and organic carbon) (Kremser et al., 2016). Volcanic aerosols, except for the non-sulfate compounds, interact with ozone at the lower stratosphere and form sulfate (SO₄) a potent aerosol, that lasts from years to decades reflecting sunlight and cooling the earth (Kremser et al., 2016; Stenchikov, 2021). Other sources of stratospheric aerosols are space dust from the explosion of meteors that enter the stratosphere through the upper atmosphere (Kremser et al., 2016).

The composition and color of the aerosols have different impacts and feedback mechanisms on the Earth's climate, depending on the actual earth composition beneath them. For example, white aerosols above a white surface like snow, have a heating effect compared to the same aerosols over a dark surface like ocean water, green forests, etc. (Haywood, 2021). Black aerosols, such as black carbon from fossil fuel burning and biomass, have absorbing characteristics, nevertheless, they can contribute to cooling the surface when they are in the stratosphere acting as the ozone layer (Kremser et al., 2016), in this case, white and black aerosols have the same cooling effect. On the other hand, the climate has been shown to have an impact on the aerosols that are absorbed into the atmosphere. When desertification increases, minerals are released into the atmosphere which causes extra heating and expands the arid lands in a positive feedback loop (Haywood, 2021).

Different mechanisms contribute to the transport of aerosols to the upper troposphere and stratosphere, among them are physical processes (including the troposphere to stratosphere direct supply from volcanic eruption through the tropical tropopause layer, and the stratospheric wind transport through the Brewer and Dobson Circulation (BDC)), and chemical and microphysical processes that include aerosol formation from supplemental elements, growth, and casting out through physical processes such as sedimentation and air transport to extratropical tropopause (Kremser et al., 2016; Stenchikov, 2021). Figure 2 presents an

overview of the processes governing aerosol supply, formation, transport, and removal, on the stratospheric aerosols (Kremser et al., 2016).

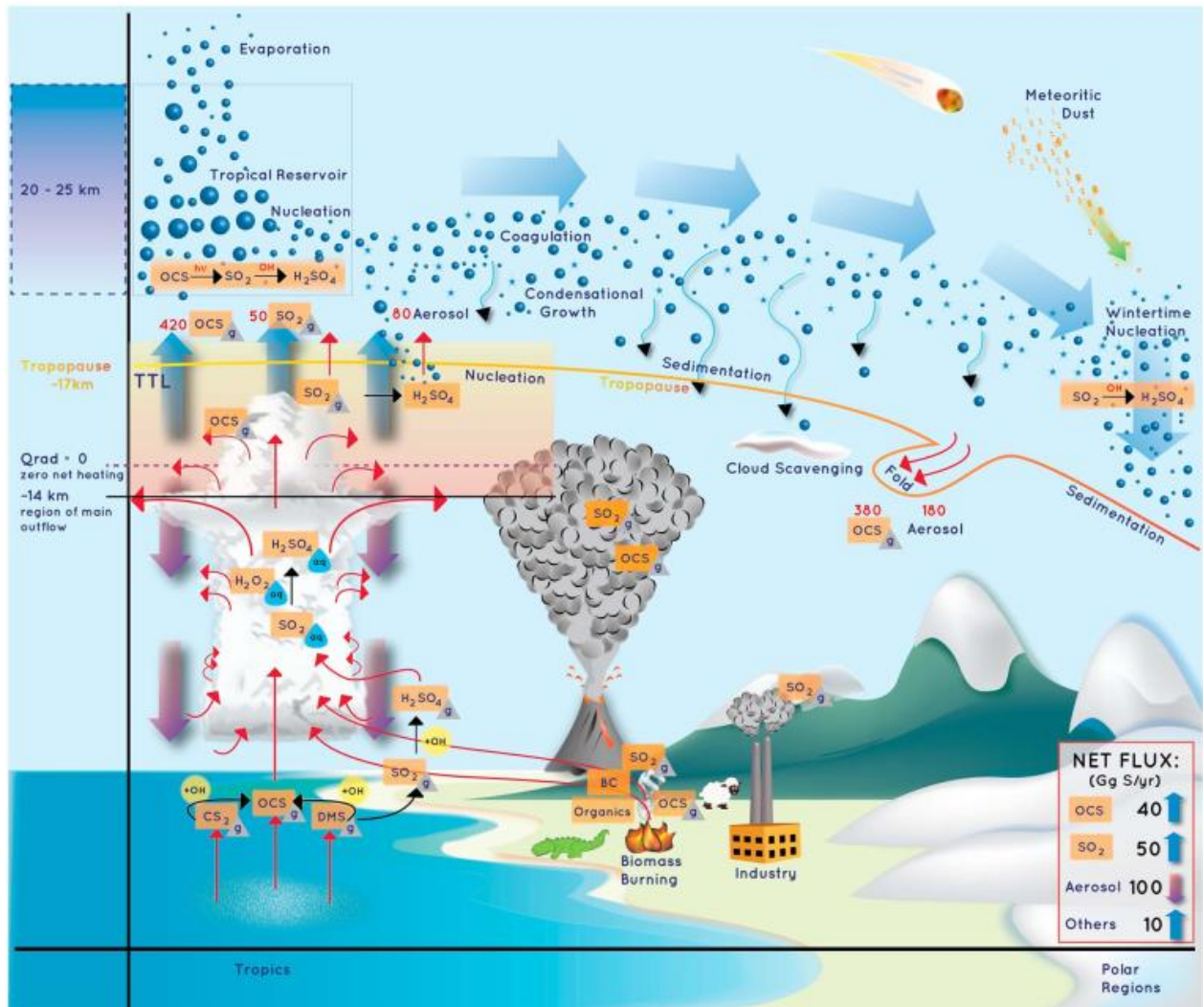


Figure 2. Processes governing aerosol supply, formation, transport, and removal from the stratosphere (Kremser et al., 2016)

2.2.4. Land Use and Land Cover Change and Climate Change

Land Use and Land Cover Change (LULCC) have an impact on the climate through mainly two processes, which comprise the biogeochemical effects and the biophysical effects, with the former impacting the global scale and the latter mostly on a local scale with a high level of interaction between the two processes (Duveiller et al., 2020; Orlov et al., 2023). BGC effects comprise the effects of LULCC on global GHG emissions leading to a global change in the climate, while the BPH effects comprise the more locally presented effects of LULCC in the

energy budget from the sun, for instance, the increased heat during summer/daytime and very cold nights/winters for deserted areas (Duveiller et al., 2020). The biophysical effects are responsible for the reduction in ecological and ecosystem services of deforestation and negative impacts on human health, morbidity, and mortality (Orlov et al., 2023).

In general, LULCC in the world is mostly impacted by human activities due to agriculture, industry, and urbanization while climate change plays a small role on the rate of LULCC in the global scale (Gogoi et al., 2019; Lambin et al., 2003; Mahmood et al., 2016; Salazar et al., 2015). Nevertheless, LULC has been one of the main causes of global, regional, and local climate change and global warming (Gogoi et al., 2019; Lambin et al., 2003; Riebsame et al., n.d.; Salazar et al., 2015) with huge impacts in human health (Orlov et al., 2023).

2.3. Review of past and Future Climate Change in Africa

Many have attempted to document the past and future African climate, which resulted in a wealth source of information one can stand upon to develop new approaches in climate research in Africa, from continental, and regional, to local scale. However, most of the studies have relied only on investigating temperature and rainfall variability and trends over the past decades to millenniums (Chase et al., 2024; Collins, 2011; Donmez et al., 2024; Hannaford & Nash, 2016; Henderson et al., 2017; Holmgren & Öberg, 2006; Hulme et al., 2001; Mccann, 1999; Muthoni et al., 2019; S. E. Nicholson, 2000, 2001b, 2001a; Nielsen & Reenberg, 2010; Ofori et al., 2021; Ongoma & Chen, 2017; Sanogo et al., 2015), with projections for future climates (Garland et al., 2014; Gbetibouo et al., 2010; Hulme et al., 2001; Jenkins et al., 2002; Kotir, 2011; Ongoma & Chen, 2017; Tyson, 1993).

2.3.1. Multidecadal climate change and variability

During the last two to one century, temperatures in Africa have been increasing consistently, with enhanced warming observed after the Industrial Revolution and the burning of fossil fuels. Many studies have highlighted the role of GHGs in shaping temperature patterns in Africa and the world. In studying observed climate change over the past century, (Hulme et al., 2001), observed an increasing temperature and reduction in rainfall, having observed a continent-wide drought in the years 1983 and 1984, although they did not find GHGs causation for this case, nevertheless the warming climate would be the root cause of the depletion of water resources over the continent. These results are supported by a similar study by (Nicholson, 2000, 2001), which observed trends on precipitation and temperature over the past 2 centuries, having observed that 30 year average rainfall over the past centuries have been decreasing by 30-40%

overs the 1930s to 1960s and 1960/7s to 1990s, with an arid climate spreading over the continent during the 1980s, with desertification impacts over the Sahel region (Nicholson, 2001). (Nicholson, 2001) suggests that this rainfall patterns are caused by increased warming of the oceans, but also, relations with vegetation land cover GHGs and aerosols have been observed to be of influence in African climate over the last 2 centuries. (S. E. Nicholson, 2000) shows that rainfall interannual variability in Africa, with enhanced effect in East Africa, are dominated by the El-Nino Southern Oscillation (ENSO), while interdecadal variability are strongly influenced by Sea Surface Temperature (SST) changes. Nevertheless, other factors have shown to influence rainfall variability over some regions in Africa, for example, the earth-atmosphere feedback systems over the Sahara region, that culminates with its expansion over the years (S. E. Nicholson, 2000). Observations of rainfall and temperature prior to 1800s is not available for most of the continent, therefore estimations of rainfall are made based on proxy data and historical observations of drought and famine (Mccann, 1999; S. E. Nicholson, 2000), however, proxy data such as tree rings, lake bed core and glaciers are still less available or understudied (Mccann, 1999). According to (Mccann, 1999) most of the African continent is affected by intra-annual variations more than the interannual and decadal variations, since they rely on rain fed agriculture, therefore, focus on this subject requires attention from climate research. Recent studies on the impacts of climate change on African agriculture confirm this theory (Mccann, 1999).

2.3.2. African paleoclimate

Many authors have not considered a pan-African approach to paleoclimate given the dynamics and efforts needed to conduct that level of research, nevertheless, studies on African paleoclimate research have brought its attention to regional climate. African paleoclimate analysis dating from the Pliocene (last period of the Neogene) and Pleistocene, from marine sediments cores, reveal that fluctuations between drier and humid climates have been occurring throughout the evolution of time, caused by changes in the orbital variations and formation and melting of glaciers in polar regions (deMenocal, 2004). The periods with the occurrence of megadroughts and aridity included approximately 2.8 million years ago (Ma), 1.7 Ma, and 1.0 Ma, which are correlated with the occurrence of peak intensification of high-latitude glacial cycles (deMenocal, 2004). Humid regimes are perceived to have occurred around 2.9-2.4 Ma and after 1.8 Ma, which coincided with the occurrence of a suitable climate for the evolution of faunal species such as mammals and eventually the origin of the *Homo* (human species) (deMenocal, 2004). A more detailed review conducted by (Gasse, 2000), observed that most

proxy records indicated intense droughts in tropical climates in both northern and southern hemispheres during the Last Glacial Maximum (LGM) dated around 23 – 18 thousand years ago (kyr), which were associated with lower tropical land and SST. However, fluctuations between drier and wetter conditions have prevailed throughout time. The first occurrence of a humid climate was observed between 17 and 16 kyr ago, caused by an accelerated warming in Antarctica. This event was followed by another two arid-humid transit periods that persisted between 15-14.5 kyr and 11.5-11 kyr prevailed through the equatorial and northern Africa, which were correlated with Greenland warming events and switching the oceanic thermohaline circulation to modern mode. The last period of arid megadroughts was observed during the Holocene around 8.4-8 kyr and 4.2-4 kyr in the northern hemisphere dominated by monsoons (Gasse, 2000).

Therefore, specific to East Africa, many studies have attempted to study the climatology of this region using evidence gathered from sediment cores from lakes and riverbeds (Johnson & Odada, 2019). Research published in (Johnson & Odada, 2019) shows that East African climate change in this region, which has the same tendency as observed by the above-mentioned studies, was highly influenced by Milankovitch cycles, interannual variabilities such as Indian Ocean Dipole (IOD) and ENSO, as well as long-term trends in glacial maximum formation in polar regions, highlighting as well the role of plate tectonics, which is the principal cause of lake formation in this region. To reconstruct the tropical precipitation change using drill cores from Lake Malawi (East Africa), (Scholz et al., 2007) observed megadroughts in this region between 135 and 75 kyr, characterized by severe aridity which reduced the levels of the lake by more than 95%, similar results were also observed in other lakes such as Lake Tanganyika (East Africa) and lake Lake Bosumtwi (West Africa). The authors observed that these phenomena were more severe than the LGM arid desiccation, the most arid period of the Quaternary, and changes in Earth-Sun orbital eccentricity, which resulted in precession. After approximately 70 kyr the authors observed an overall increase in lake level due to increased humidity in the region (Scholz et al., 2007).

Global temperatures have been fluctuating at the same rhythm as paleontological hydrological fluctuations. Research by (Marcott et al., 2013) that analyzed temperatures for the past 11300 years (11.3 kyr) from globally distributed records, showed that a warming period during the early Holocene (10 to 5 kyr) which was followed by a cooling period in the order of 0.7°C during the late Holocene (<5 kyr) driving into the late phase of the Little Ice age which observed cooling in order of 2°C, around 200 years ago. These results were also observed by (S. E.

Nicholson et al., 2013) when analyzing the temperature variability over Africa during the last 2000 years, observing that both in Africa and in the world the current rising of temperatures is highly unprecedented in any observed paleoclimate reconstruction (Marcott et al., 2013; Neukom et al., 2019; S. E. Nicholson et al., 2013), and future projections are to be more accentuated under the influence of GHG emission scenarios (Marcott et al., 2013).

a) Wind variability

African climate is driven by the interactions between surface winds and low-altitude pressure systems, which result from high-altitude atmospheric circulation (Gasse, 2000; S. E. Nicholson & Flohn, 1980), presenting a zonal characteristic climate and seasonal precipitation patterns. Mediterranean-like temperate climates characterized by winter rains and summer droughts are predominant over the northern and southern edges of the continent, in response to the equatorward displacement of the mid-latitude westerlies (Gasse, 2000). These regions are bordered by the Namib Desert in the southwest and the Sahara Desert in the north, regions highly dominated by persistent tropical and subtropical anticyclones (Figure 3). These two regions, are separated by a wide belt dominated by tropical climates is dominant, which are characterized by the seasonal migration of the ITCZ, which culminates with monsoonal-driven climate, characterized by summer rains and winter droughts, along with a humid equatorial zone that observes a double rainfall maximum (Figure 3; Gasse, 2000).

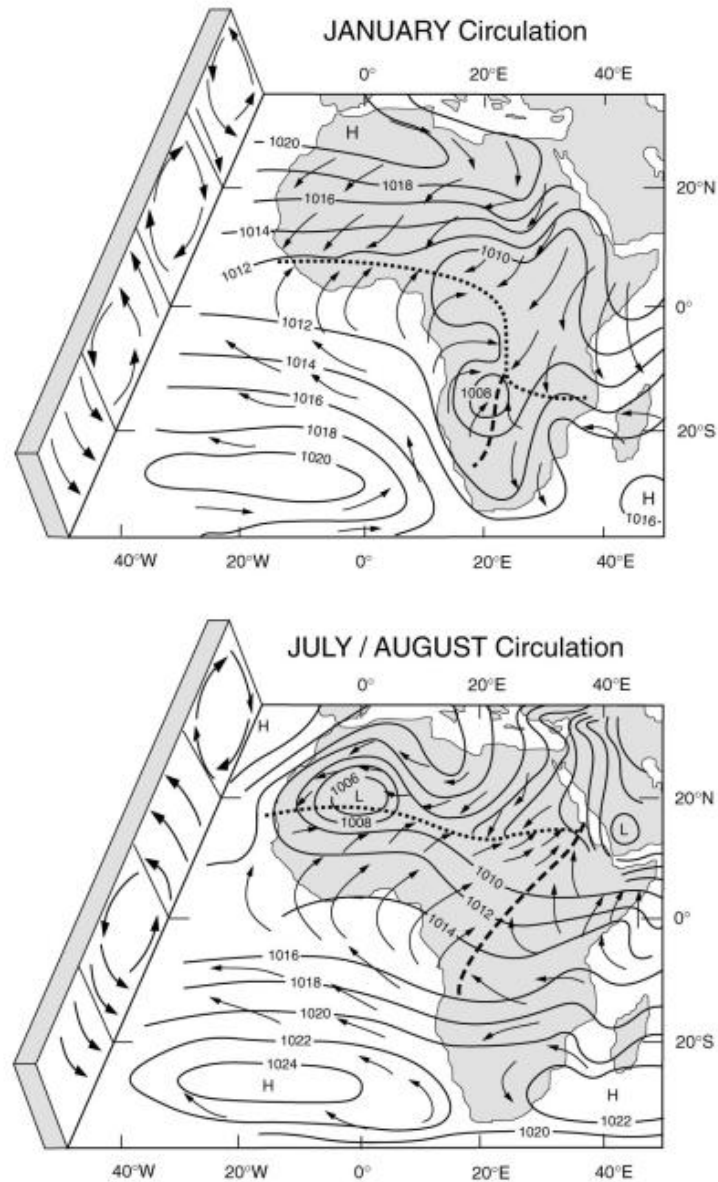


Figure 3. Schematic representation of Wind patterns and pressure systems over Africa, highlighting the seasonality of wind. Dotted lines represent the ITCZ and the dashed lines indicate the Congo Air Boundary. Source: (Gasse, 2000).

Other factors, including topography and ocean conditions, influence these zonal and seasonal patterns. While highlands are the drivers of surrounding lowland rainfall patterns, altering both temperatures and moisture distributions, the cold Benguela Current and the warm Agulhas Current are responsible for large of the East-West climate asymmetries, along with the ENSO and temperature fluctuations in the Indian and Atlantic Ocean, which influences rainfall variability in East Africa, highlighting the teleconnections of African climate to the global climate and atmospheric and oceanic circulation (Gasse, 2000).

b) Paleoclimatology of winds

Reconstructions documented in (S. E. Nicholson & Flohn, 1980) made it possible to draw schematic representations of the wind patterns prevalent during three important geological ages, namely, the Late Pleistocene, Early to Mid-Holocene, and Late Holocene.

During the Late Pleistocene, particularly at the peak of the Last Glacial Maximum around 18 kyr, African wind patterns were dominated by global cooling and high-pressure systems, where the subtropical high-pressure belts, including the South Atlantic and Indian Ocean highs, were strengthened and shifted equatorward, reducing rainfall in a large part of the continent (Figure 4; Nicholson & Flohn, 1980). Cooler SST and reduced solar heating contributed significantly to the weakening of the West African Monsoon circulation leading to the formation of arid conditions, predominantly in North Africa, while the northwest winds strengthened and became the transport mechanism for dust from the Sahara Desert to the Atlantic, intensifying also the dry and dusty Harmattan winds (S. E. Nicholson & Flohn, 1980). During this period the ITCZ was displaced southward reducing the rainfall in regions north of the equator (Figure 4).

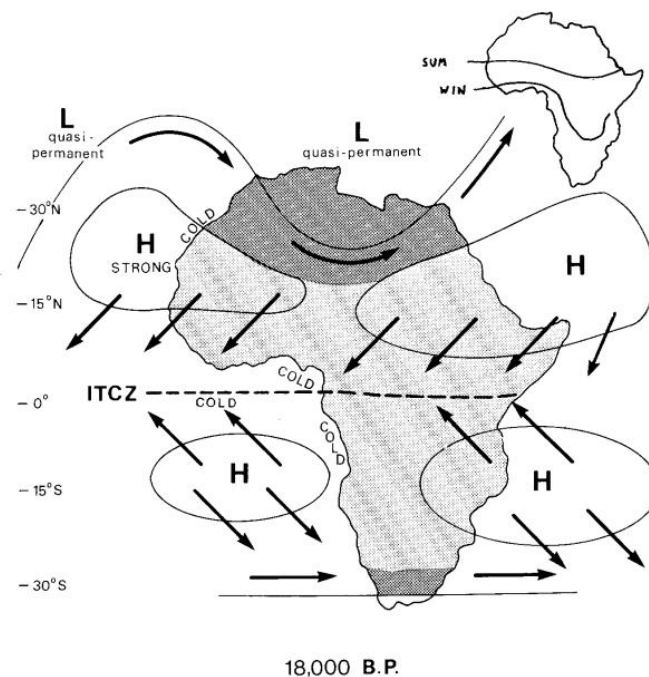


Figure 4. Tentative representation for the African Atmospheric circulation, during the late Pleistocene (20 – 12 kyr). Dark shading represents areas that had more rainfall than today, and light shading areas represent areas with less precipitation than today. Inset lines represent the position of the ITCZ in winter and summer. Source: (S. E. Nicholson & Flohn, 1980).

During the Early Holocene (around 10 – 8 kyr), a shift in precipitation patterns occurred, where much of the continent was humid and warmer, due to increased solar insolation by then, which strengthened the monsoonal circulation driving the ITCZ northwards compared to the present-day position (S. E. Nicholson & Flohn, 1980). These events contributed to widespread precipitation in areas that later became deserts, including the Sahara Desert, which was by then covered by lakes, rivers, and savannas (S. E. Nicholson & Flohn, 1980). The intensification of the monsoonal winds, carrying moisture from the Atlantic Ocean into the interior region of the Sahel and northern Africa, was noticed, along with the weakening of the northwest trade winds that contributed to the reduction of aridity of these regions leading to persistent humidity in many regions (Figure 5; Nicholson & Flohn, 1980).

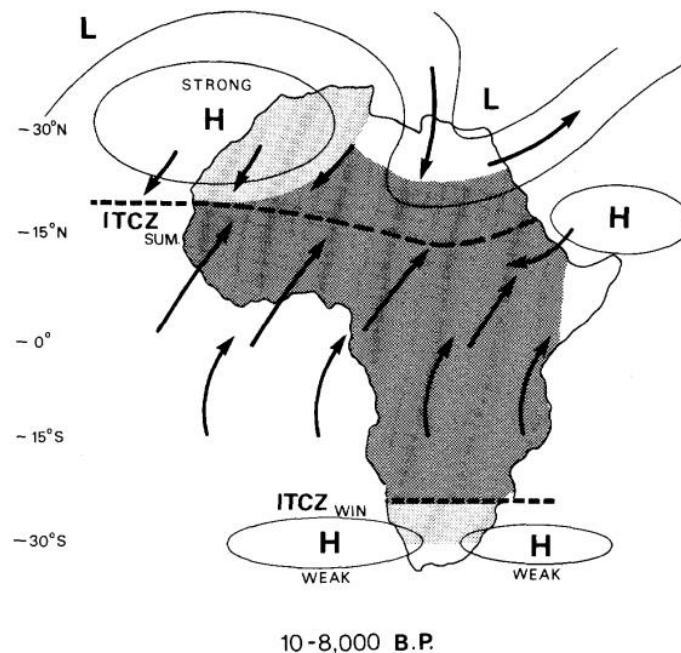


Figure 5. Tentative reconstruction of wind patterns during the Early to mid-Holocene (10 – 8 kyr). Dark shading represents areas that had more rainfall than today, and light shading areas represent areas with less precipitation than today. The dashed line represents the position of the ITCZ in summer and winter. Source: (S. E. Nicholson & Flohn, 1980).

Lastly, during the Mid-Holocene (6.5 – 4.5 kyr) the solar insolation decreased and the continent observed a weakening of the monsoonal systems and the southward movement of the ITCZ, a transition that marked the African Humid Period, resulting in the re-expansion of the deserts, including the desert of Sahara, along with the beginning of arid conditions in northern and eastern Africa (Figure 6; Nicholson & Flohn, 1980). The northeast trade winds strengthened contributing to the increased desertification and dust transport observed during this period,

especially from the Sahara Desert. During this period, modern atmospheric circulation, including the Harmattan winds and the seasonal shifts of the ITCZ, were established, culminating in the actual rainfall patterns across Africa, influencing establishment of ecosystems that allowed human life settlement and development during the Holocene (S. E. Nicholson & Flohn, 1980).

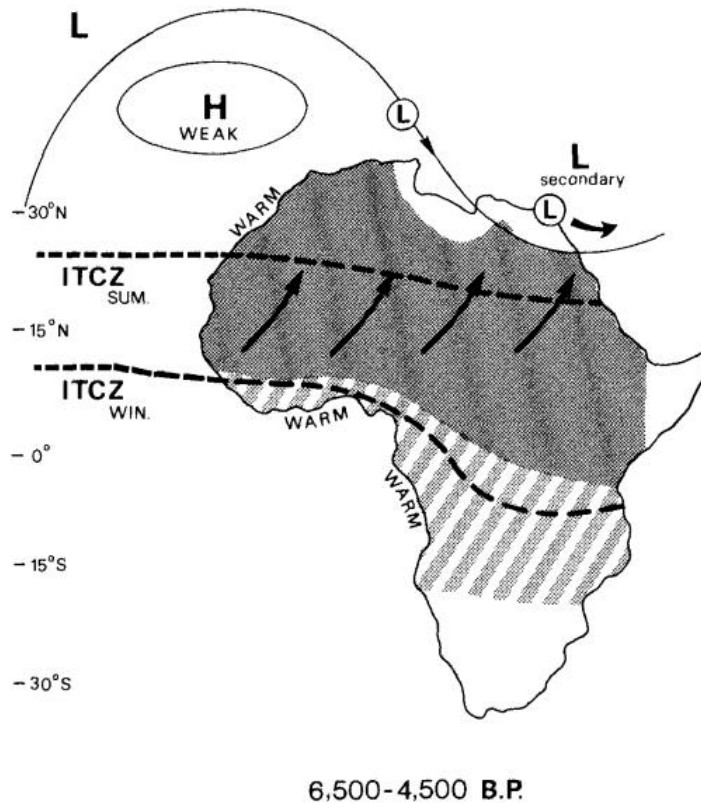


Figure 6. Tentative reconstruction of wind patterns during the mid-Holocene (6.5 – 4.5 kyr). Dark shading represents areas with more rainfall than today, and hatching represents the areas drier than previous periods but wetter than today. The dashed line represents the position of the ITCZ in summer and winter. Source: (S. E. Nicholson & Flohn, 1980).

2.3.3. African GHG Emissions during the pre-and post-industrial era

The GHG emissions have been fluctuating following the glaciation and deglaciation of the earth. Accessible literature reports the evolution of GHG emissions and sinks dating from the late pre-Cambrian Era. Two prominent compilations by (Stanley & Luczaj, 2014) and (Summerhayes, 2015) along with relevant research made using proxy data, allow us to draw perspectives of the evolution of GHG emissions throughout the ages of the earth (Goudie, 2005; Hoffman et al., 1998; Royer et al., 2007). During the pre-Cambrian (4.6 Billion (Byr) – 541 Million years ago (Myr), the early ages of the earth's creation, controlled by volcanic

outgassing and hydrothermal vents, the earth's atmosphere was composed mainly of CO₂, CH₄, and water vapor with negligible oxygen levels (Stanley & Luczaj, 2014; Summerhayes, 2015). About around 3.5 Byr, the concentration of CO₂ began to reduce due to the advent of photosynthetic activity by cyanobacteria, which culminated with the Great Oxidation Event (approx. 2.4 Byr) that led to drastic reductions of CH₄ levels contributing to the cooling episodes observed during this era. During the later ages of the Pre-Cambrian, during the Neoproterozoic (approx. 720 – 635 Myr), the snow age ended due to volcanic emissions of CO₂ and plate tectonic activities, leading to a warmer earth (Hoffman et al., 1998).

The Paleozoic Era (541 – 252 Myr), was characterized by fluctuating levels of CO₂, leading to significant reductions due to extensive vegetation growth (Hoffman et al., 1998; Summerhayes, 2015). During the Mid-Paleozoic, the Carboniferous period (approx. 359-299 Myr) observed a significant absorption of atmospheric CO₂ due to the expansion of vast coal-forming forests, a pattern that shifted during the End-Permian (approx. 252Myr) which observed an accentuated increase of CO₂ and CH₄ concentrations due to large-scale volcanic activity in the Siberian Traps, that lead to intense global warming by then (Stanley & Luczaj, 2014; Summerhayes, 2015). According to (Royer et al., 2007) patterns that reflect CO₂ radiation effects have been consistent since the Paleozoic era around 420 Myr, estimated between 1.5°C to 6°C per CO₂ concentration doubling, emphasizing the role of the CO₂ radiative effects in shaping earth's climate throughout history.

The Mesozoic Era (approx. 252-66 Myr) was marked by the splitting of the Pangea, inducing large-scale volcanic activity contributing to the releasing of large amounts of CO₂ that contributed to a historically warm GHG climate throughout a large part of this era (Stanley & Luczaj, 2014). Furthermore, a balance between CO₂ emissions and sinks was obtained through biological productivity and marine sedimentation, processes that sequestered part of CO₂ into carbonate rocks (Summerhayes, 2015), while extensive vegetation and marine productivity acted as both sources and sinks of CO₂, especially during the Cretaceous Period (approx. 145-66 Myr)(Stanley & Luczaj, 2014; Summerhayes, 2015). The Cretaceous period was also one where most tectonic processes were observed over Africa leading to the current hydrological shape of the river, and lake basins, with high interactions with the climate (Goudie, 2005).

The Cenozoic Era (approx. 66 Myr - Present) marked the age of the modern continents and of most human evolution, is also marked by an overall decrease of atmospheric CO₂ in the long term caused mainly by the dissolution of silicate rocks and carbon burial in the ocean floor.

This gradual decrease in GHG has involved very important changes in the climate (Stanley & Luczaj, 2014; Summerhayes, 2015). A remarkable one that has been documented well was the Paleocene-Eocene Thermal Maximum (PETM) which occurred about 56 Mya; a sudden burst of methane, CH₄, and CO₂ into the atmosphere led to global warming and ocean acidification (Stanley & Luczaj, 2014; Summerhayes, 2015). After that some 34 million years ago, the earth was in an “Icehouse Climate,” which includes developments of the Antarctic ice sheets (Stanley & Luczaj, 2014; Summerhayes, 2015). This change in Earth’s climate to cooler conditions in the later part of the Cenozoic was further reduced due to more decrease in GHG levels and proved that the atmospheric composition was the key factor in the control of the climate of this oration (Stanley & Luczaj, 2014; Summerhayes, 2015).

The Anthropocene (1750 yrs to present) is characterized by monumental human interferences in the Earth and Climate through the debut of industrial processes, deforestation, and burning of fossil fuels (Adzawla et al., 2019; Ernst et al., 2024; Gaiduk et al., 2010; López-Ballesteros et al., 2018; Ramanathan et al., 1987; Ramanathan & Feng, 2009; Tongwane & Moeletsi, 2018; Tuckett, 2021) which activities have greatly elevated the level of GHGs, such as CO₂, CH₄, and N₂O in the atmosphere at a level that is unprecedented in the modern world, causing the current climate change scenario and global warming. Further, other positive climate forcing are exacerbating these anthropogenic emissions such as the thawing of permafrost and sea ice, with lower albedo enhancing the absorption of solar radiation as it frees up carbon that had been locked in permafrost and reducing the planet’s solar radiation reflectivity making climate change accentuated and more severe (Stanley & Luczaj, 2014; Summerhayes, 2015; Tuckett, 2021).

2.3.4. Distribution and variability of Aerosols over Africa

The distribution and variability of aerosols over Africa present strong climate feedback effects, influencing weather patterns and air quality, while they are dominated by the continent’s landscape and atmospheric circulation patterns that govern the continent and are composed mainly of dust minerals, biomass burning, and anthropogenic emissions, and following a strong seasonal and regional pattern. The West African region, the Sahelian region is dominated by a transition between mineral dust abundance during the dry season and biomass burning and sulfate aerosols following the beginning of the West Africa Monsoon (Cavalieri et al., 2010; Matsuki et al., 2010). A similar pattern was observed in East Africa, where monsoon cycles dominate the variability of aerosol optical properties, with higher optical depths predominant

during dry seasons caused by increased supplies from biomass burning emissions and desert dust (Boiyo et al., 2017; de Graaf et al., 2010).

Atmospheric dynamics have been shown to greatly impact the vertical distribution of aerosols along with different transport mechanisms. For instance, over the Namibian coast, the composition of the aerosol consists primarily of polluted dust and smoke from biomass burning, which are transported up to the troposphere reaching up to 6km above sea level (Cavalieri et al., 2010). During dry in the Sahel region, biomass burning dominates the atmospheric aerosol composition, increasing concentrations with altitude, while in the Sahara Desert dust aerosols are dominant during the summer, with the same vertical variability exceeding over 6km altitude (Cavalieri et al., 2010). Interconnections are observed between the Sahara Desert dust to Europe, being transported through long-range atmospheric transport mechanisms which culminate with the formation of high-altitude plumes of dust in the earlier-mentioned regions (Marinou et al., 2017).

As the mechanisms of transport and distribution vary across Africa, along with its composition, aerosol optical properties also vary in different regions of Africa, where in Southern West Africa, biomass-burning aerosols are characterized by high indexes of absorption properties, where the single scattering albedo (SSA) values from 0.81 to 0.92 at 550 nm, indicating strong light absorption (Denjean et al., 2020). On the other hand, in the South African savannah, the regional new particle formation due to anthropogenic activities such as industrial activities that release sulfur, and the burning of biomass producing CO₂ dominate the diurnal variability (Vakkari et al., 2013). At the same time, the occurrence of dry and wet seasonal variability leads to low density during wet seasons and high densities during dry seasons, which in count influence the absorption/scattering of solar energy (Vakkari et al., 2013).

From a geological timescale the aerosol production varied between wet and dry periods and transported through the different regimes of atmospheric circulation that prevailed during the time (see section 2. c. on the Paleontology of winds).

2.3.5. Temporal and Spatial Variability of Ozone in Africa

The temporal variability of ozone concentrations over Africa has been highly impacted by natural processes and human activities, especially after the Industrial Revolution, when tropospheric, ozone due to the release of NO_x and VOCs, started to increase concentration while stratospheric concentrations of ozone started depleting, due to the emissions of ODS.

Global levels of tropospheric ozone levels were comparably low during the pre-industrial revolution, due to low levels of human contributors to the ozone formation, however, after the industrial revolutions studies account for approximately 40% of the increase in tropospheric ozone compared to the pre-industrial era, with Africa contributing to the global trends due to population growth and industrialization (Hansen et al., 1998; Lindsey Valich, 2019; Lyu et al., 2023), which capitalized on the anthropogenic dominance in the post-industrial Revolution era tropospheric ozone emissions through the burning of fossil fuels, deforestation, and agricultural expansion, pronounced particularly in recent decades of accelerated urbanization and industrialization in many African regions (Marufu et al., 2000; Y. Zhang et al., 2021). Biomass burning through slash-and-burn agriculture, wildfires, and cooking fires, positioned Africa as a global hotspot of tropospheric ozone emissions since these activities release CO and NO_x, which are pertinent to elevated ozone levels, and studies have shown that ozone produced by fires in Africa can be transported across the tropics reaching regions such the western pacific (Bauer et al., 2019; C. Sullivan, 2016). Regionally, high ozone concentrations have been dominant in some regions in interior South Africa due to the local air quality conditions, attributed to industrial emissions, vehicle exhaust, and seasonal agricultural fires (Fisher et al., 2021; Leah Laban et al., 2018). While biomass burning and biogenic emissions are the main precursor of surface ozone formation, with up to 50ppbv during burning seasons (Aghedo et al., 2007), lightening is the dominant precursor in the upper tropical troposphere, specifically over the Atlantic Ocean and Western Africa, NO₂ is the main contributor to tropospheric formation in this region, particularly above 12km altitude (Tadic et al., 2021). In regions such as the Indian Ocean, the main process responsible for ozone formation, biomass burning emissions, is enhanced through photochemical processes during transport, capable of producing about 2.5-3ppbv/day (Taupin et al., 2002).

Transport and variability of ozone are governed by regional and global atmospheric circulation patterns, where in regions of West Africa, ozone levels increase from fostered areas to the Sahelian region caused by enhanced photochemical production and deposition processes, and northward transport of trace gases by monsoon fluxes, during the monsoon season (Saunois et al., 2009). On the other hand, ozone formed in Africa is transported to Asia, primarily through the upper ramification of the Hadley cell and subtropical westerlies, showing a strong seasonal variability and contribution to Asia's ozone levels in the upper troposphere during spring (Han et al., 2018). Also, global atmospheric circulation contributes to the transport of biomass-

burning ozone across the tropics to regions such as the Western Pacific (Bauer et al., 2019; C. Sullivan, 2016).

Recent trends in global tropospheric ozone show an increase in concentrations between 1980 and 2010, with regions such as Southeast Asia and Africa playing significant roles in global emissions, due to the continued rise of emissions orchestrated by the rapid growth of population, urbanization, and limited environmental policies, contrasting well-developed countries that observe reductions in ozone precursor emissions due to enhanced regulations (Y. Zhang et al., 2016, 2021). Other observations show that about 4% of the global total atmospheric ozone, which includes the tropospheric and stratospheric ozone, has been depleted between 1979 and 2020, governed primarily by the stratospheric ozone reductions caused by the ODS, however, with less relevance to the dynamics of Africa's tropospheric ozone, which are governed by local and regional emissions (EPA, 2024).

Due to the release of ODS, since the 1970s, including CFCs, global and African stratospheric ozone has been depleting, which was enhanced over the 20th century, leading to the increased UV radiation reaching the earth's surface (NASA, n.d.; Staehelin et al., 2018). However, since the implementation of the Montreal Protocol in 1987, stratospheric ozone have been recovering gradually, and current projections suggest that global stratospheric ozone levels will return to 1980 levels by 2040, nevertheless, regional variability still introduces some uncertainties (EEA, 2024; Staehelin et al., 2018). This trend will contribute to the total column ozone (total atmospheric ozone) which is predicted to increase in future scenarios due to increasing emissions of tropospheric ozone from industrialization, transportation, and agriculture, enhancing the potential of exacerbating health issues, reducing agricultural productivity and impacting positively to the climate change (F. Brown et al., 2022; Fisher et al., 2021).

2.3.6. Temporal and spatial variability of land use land cover change (LULCC) in Africa

Apart from the temporal changes imposed by the changes in the earth and atmosphere compositions during the geological time scale, changes observed during the Anthropocene are mainly due to the combination of both natural and human actions and generally, LULCC has been following a seasonal and long-term trend. For instance, from 1990 to 2010, the African forest cover experienced a loss of about 75 million hectares, approximately 10% of the total forest area, in a rate of 0.36% per year, due to expansion to areas of agricultural uses, representing the second highest rate of land cover change after Southeast Asia with 0.71%

change per year (Michigan State University, n.d.). Other observations show that between 1998 and 2022, cropland expanded intensely, expanding from 10.9% to 51.98% of the total land area, accompanied by decreased forest land (Arfasa et al., 2023).

Regional analysis shows different patterns across the continent. In sub-Saharan Africa interannual land cover change driven by climate variability predominant in semiarid regions that led to modifications in rainfall availability led to a 4% loss of vegetation between 1982 and 1991 (Xiao et al., 2022). In West Africa, studies have shown an important decline in natural vegetation by 1.6% between 1975 and 2013, driven by a change from natural to human-managed landscape, with a significant increase of cropland (107.8%) and settlements (140%) (Asenso Barnieh et al., 2023; Barnieh et al., 2020; Herrmann et al., 2020). In Burkina Faso, loss in natural vegetation was estimated in 17.9% in the period 1999-2011 (Zoungrana et al., 2015). In East Africa, studies conducted in the Lake Baringo catchment in Kenya show dramatic reductions in forest cover exceeding 40% in 14 years due to human activities and climate change (Kiage et al., 2007). Additionally, an increase in cropland in the order of 34.8% was observed in East Africa between 1998 and 2017, where countries including Ethiopia, Kenya, Uganda, Malawi, Rwanda, Tanzania, and Zambia, lost large quantities of woody vegetation classes (Bullock et al., 2021). In Uganda, grassland around Mpologoma is predicted to be replaced by subsistence agriculture farms by 2039 (Bunyangha et al., 2021). In South Africa, rural areas also follow the same pattern, although registering losses in agriculture land cover due to low productivity caused by limited precipitation between 1984 and 2022 (Mogonong et al., 2024).

2.4. Summary

CC in Africa has been a function of many contributors, from the natural to the anthropogenic stressors of the climate. During the Geological time scale from the creation/formation of the earth, the climate has been a function of changes in the earth's atmosphere composition, along with the cyclic periods of glaciation and deglaciation, where the plate tectonic movements and volcanic activities played a great role in releasing GHGs, and aerosols to the atmosphere.

Current research accounts that in the current Anthropocene, the globe and Africa are being affected by human activities that contribute to the emission of GHGs and ozone-depleting substances as well as ozone precursors. Changes in Land Use and Land Cover or vegetation cover contribute significantly to the warming of the continent while being influenced by rainfall patterns variable across many regions of the continent. While the total column ozone is increasing in many regions, the increasing of the tropospheric ozone leads a pathway to the increment of GHGs and planet warming.

Other Factors such as atmospheric composition and dynamics have been shown to contribute significantly to the climate dynamics as well as the transport of atmospheric constituents such as aerosols from many parts of Africa to the world. Such dynamics including changes in atmospheric circulation and rainfall and temperature patterns contributed to the desertification of the Sahara region as well as forest formation throughout the central Africa region, with an impact on aerosol formation and composition throughout the ages. Atmospheric dynamics and composition, influenced by other factors such as volcanic activities and glaciation cycles, shown to be the principal agent that controls the climate dynamics in Africa.

3. Data and Methodology

4. Data and Methodology

The methodology used in this research is summarized in the flowchart presented in Figure 7. The process began with data collection from various sources, followed by adjustments for the incomplete dataset covering the entire analysis period, which employed estimations through linear regression methods. The data was resampled to a 0.75-degree spatial resolution and generated annual summaries.

4.1. Data

The present study utilizes total ozone column data, total aerosol optical depth at 550 nm and 820 nm (AOD_550 and AOD_865), 2-meter temperature, atmospheric water vapor content, atmospheric pressure, Methane (CH₄) total column concentrations (XCH₄), and U and V wind components from the Copernicus Monitoring Service (CAMS) global reanalysis (EAC4; Inness et al., 2019) for the period from 2003 to 2023. Atmospheric precipitation data from the Global Precipitation Climatology Project (GPCP; Copernicus Climate Change Service -3CS, 2021) was obtained for the same period. Normalized Difference Vegetation Index (NDVI) data from the Copernicus Global Land Monitoring Service (CLMS; European Commission Directorate-General Joint Research Centre (ECDGJRC), 2017, 2021) also spans from 2003 to 2023. The total column means molar fraction of Carbon Dioxide (CO₂) (XCO₂) was sourced from the CAMS Greenhouse Gases Reanalysis (CAMS-EGG4; Copernicus Atmosphere Monitoring Service (CAMS), 2021) for the period of 2003 to 2020. To complete the dataset for the study period (2003 – 2023), the XCO₂ utilized for statistical and linear regression analysis were estimated using auxiliary data: the CO₂ Volume Mixing Ratio in the Upper Troposphere (co22_vmr_uppertrop), which was obtained from the Sounder SIPS: AQUA AIRS IR-only Level 3 CLIMCAPS: Comprehensive Quality Control Gridded Monthly Version 2 (SNDRAQIL3CMCCP_2; Barnet, 2019) covering 2003 to 2023, applying Linear Regression Analysis, with account for non-linearities among variables using exponential approximations. In summary, the dataset used in this study encompasses the entire African continent, covering a latitude range from 37°N to 35°S and a longitude range from 22°W to 55°E, within the timeframe of 2003 to 2023. Table 7 presents a summary description of the data set utilized in the analysis conducted for this research.

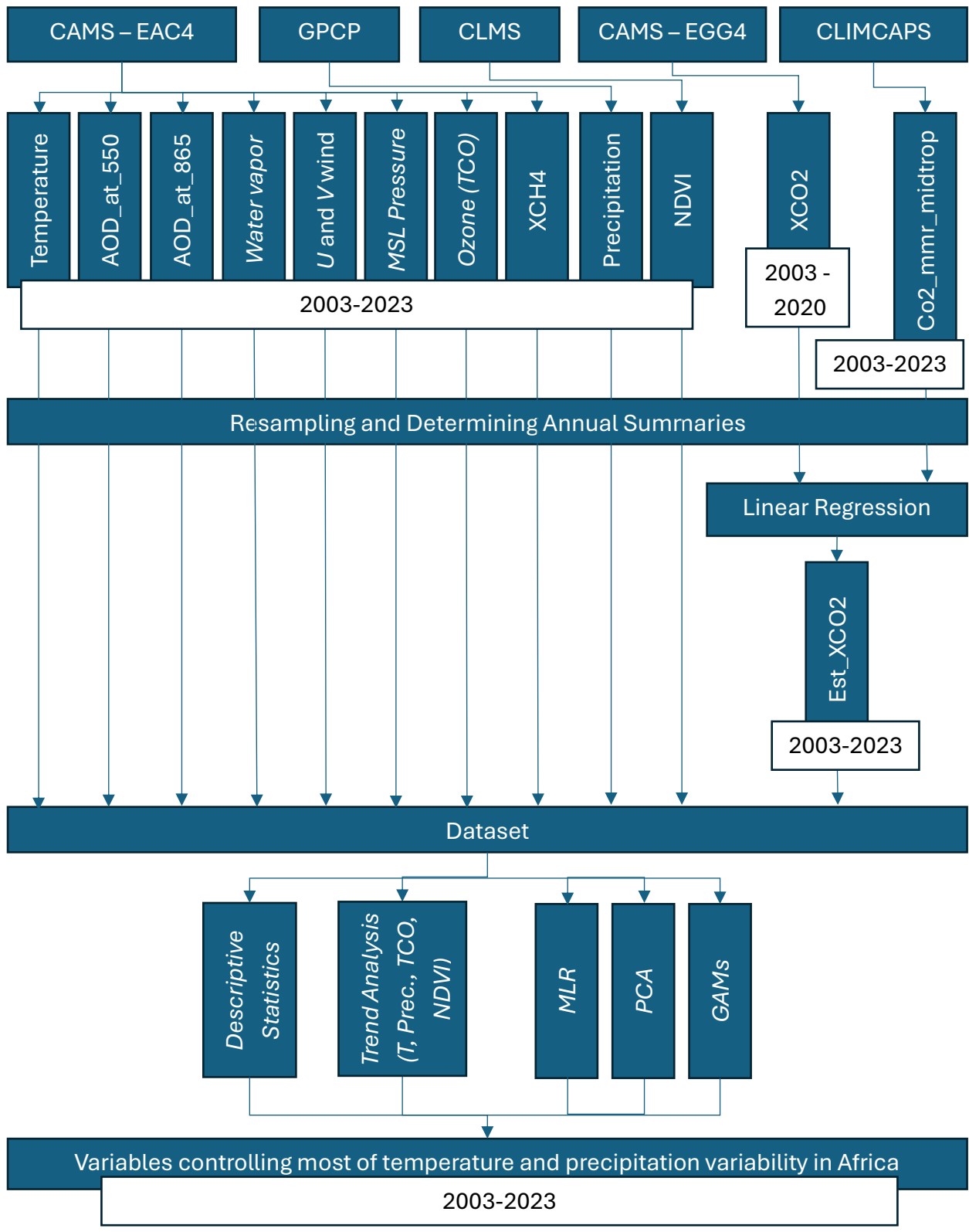


Figure 7. Flow chart of the methodology used for the present research. The trend analysis was performed only on the 4 variables whose interactions are spotted in this research (Temperature, Precipitation, TCO, and NDVI).

Table 3. Summary of the dataset and sources used for the present research

Variable	Source	Spatial resolution	Temporal resolution	Temporal Coverage	Citation
Ozone total column (TCO)	CAMS - EAC4	0.75°x0.75°	3 hours	2003-2023	(Inness et al., 2019)
Total aerosols optical depth at 550nm	CAMS - EAC4	0.75°x0.75°	3 hours	2003-2023	(Inness et al., 2019)
Total aerosols optical depth at 820nm	CAMS - EAC4	0.75°x0.75°	3 hours	2003-2023	(Inness et al., 2019)
2 meters Temperature	CAMS - EAC4	0.75°x0.75°	3 hours	2003-2023	(Inness et al., 2019)
Atmospheric content of water vapor	CAMS - EAC4	0.75°x0.75°	3 hours	2003-2023	(Inness et al., 2019)
Atmospheric Pressure	CAMS - EAC4	0.75°x0.75°	3 hours	2003-2023	(Inness et al., 2019)
U and V components of wind	CAMS - EAC4	0.75°x0.75°	3 hours	2003-2023	(Inness et al., 2019)
Precipitation	GPCP	1°x1°	1 day	2003-2023	(3CS, 2021)
NDVI	CLMS - NDVI 1998-2020 (raster 1km) version 2	1km	10 days	2003-2020	(ECD-GJRC, 2017)
	CLMS - NDVI 2020-present	300m	10 days	2021-2023	(ECD-GJRC, 2021)

(300m) version						
2						
Methane (XCH4)	CAMS	–	0.75°x0.75°	3 hours	2003	- (Inness et al., 2019)
	EAC4				2023	
Carbon Dioxide (XCO2)	CAMS	–	0.75°x0.75°	3 hours	2003	- (CAMS, 2021)
	EGG4				2020	
*CO₂ Volume Mixing Ratio in the Upper Troposphere (co2_vmr_uppertrop)	CLIMCAPS	-	1°x1°	monthly	2003	- (Barnet, 2019)
	SNDRAQIL3				2023	
	CMCCP_2					

* Auxiliary data used to estimate co2 and ch4 concentrations for the study period (2003-2023).

4.1.1. Global Precipitation Climatology Project (GPCP)

The protocol of measurement and quality assurance of the GPCP daily precipitation analysis Climate Data Record (CDR) version 1.3, involves the integration of data from multiple satellite sensors and rigorous validation techniques to produce global, high-resolution precipitation estimates (3CS, 2021; Adler et al., 2017; Huffman et al., 2001). The dataset relies on passive microwave sensors, including the Sensor Microwave/Imager (SSM/I) aboard Defense Meteorological Satellite Program (DMSP) satellites and the Advanced Microwave Sounding Unit-B (AMSU-B) on NOAA satellites, which provide direct and accurate precipitation measurements over land and oceans (Adler et al., 2017). Complementary data from infrared sensors on geostationary satellites like the GOES (Geostationary Operational Environmental Satellite) series, Meteosat, and GMS (Geostationary Meteorological Satellite), is used, which comprises extensive temporal and spatial coverage although with less precision for precipitation estimation (Adler et al., 2017). Data sources are integrated using advanced merging algorithms such as those provided by the World Climate Research Program (WCRP) and Global Energy and Water Exchanges (GEWEX) projects, which take advantage of the accuracy of the microwave observation and temporal resolution of the infrared data (Huffman et al., 2001). Calibration using in situ global observations is made to ensure that satellite-derived estimates reflect ground-level conditions (Adler et al., 2017; Huffman et al., 2001). The validation process includes cross-comparison with independent datasets, such as radar observations and regional precipitation records, offering a platform for evaluating the dataset's

accuracy and identifying biases (Adler et al., 2017). This quality control addresses the uncertainties related to sensor limitations caused by cloud interference (Huffman et al., 2001).

The GPCP dataset has been used to study global and regional precipitation trends, having observed that, while no significant global trend was observed over the past two decades, regional variations, such as those related to El Niño Southern Oscillation (ENSO) events, have been identified, which show distinct patterns in both hemispheres and ENSO-related anomalies extended into high latitudes (Adler et al., 2017). It also has been used to study the impact of volcanic eruptions and ENSO events on precipitation patterns, showing a reduction in tropical rainfall during major volcanic events and individual ENSO-related precipitation anomalies (Adler et al., 2017). Some limitations of the GPCP daily precipitation data were observed in its homogeneity, which saw complications in representing small signals over short periods, however, efforts to incorporate new satellite information will provide higher spatial and temporal resolution, improving the overall accuracy of the product (Huffman et al., 2021, 2023).

By combining these sophisticated methodologies and high-quality datasets, the GPCP provides a robust, globally consistent, and scientifically validated resource essential for studying precipitation patterns, modeling hydrological systems, and assessing climate variability and change (Adler et al., 2017; Huffman et al., 2001).

4.1.2. Copernicus Atmosphere Monitoring Service (CAMS) global reanalysis (EAC4)

The CAMS reanalysis (EAC4) is a product by the European Centre for Medium-Range Weather Forecasts (ECMWF), and covered initially a period from 2003 to 2016, which is updated annually covering now up to 2023 (Inness et al., 2018, 2019). Along with key climate variables, it includes a three-dimensional, time-consistent field of atmospheric composition, such as aerosols and various chemicals, in a horizontal resolution of 80km, using the ECMWF Integrated Forecasting System (IFS), offering more chemical variables at better temporal resolutions as an improvement of the previous versions of the reanalysis (Inness et al., 2019) due to the inclusion of modules for atmospheric chemistry and aerosols that allow the assimilation of satellite retrievals of atmospheric composition (Garrigues et al., 2022; Inness et al., 2019). The data assimilation method integrates observations of various atmospheric components, such as ozone, carbon monoxide, and nitrogen dioxide, employing a 4D-Var data assimilation method at 80km horizontal resolution (Y. Wang et al., 2019, 2020). The IFS uses updated chemistry modules, such as Carbon Bound 2005 (CB05), the French Large-Scale

Atmospheric Chemistry Model (MOdèle de Chimie Atmosphérique à Grande Échelle – MOCAGE), and the chemical transport (CT) Model for OZone And Related chemical Tracers (MOZART) version 3.5, providing a representation an enhanced quality of air quality forecasts while modeling secondary organic aerosols such as NO_x and SO_x (Huijnen et al., 2021; Inness et al., 2019) It also includes an aerosol climatology derived from CAMS reanalysis, which provides an understanding of regional aerosol radiative forcing in the medium-range weather forecasts (Bozzo et al., 2020).

The IFS assimilation process has led to smaller biases in the dataset when compared to previous versions of the system, particularly in ozone, carbon monoxide, nitrogen dioxide, and aerosol optical depth observations (Inness et al., 2019; Wagner et al., 2021) constraining effectively stratospheric and tropospheric ozone, with some challenges observed in certain regions and seasons (Wagner et al., 2021). The CAMS reanalysis has been extensively evaluated against independent observations, demonstrating a stable and accurate representation of global reactive forces over time, reproducing successfully observed concentrations of assimilated chemicals, such as ozone and carbon monoxide, with biases generally less than 20% (Y. Wang et al., 2019, 2020). However, it tends to underestimate primary hydrocarbons and secondary organic species, and discrepancies exist for fast-reacting radicals such as OH and HO₂ (Y. Wang et al., 2020), with long-term stability affected by drifts in time series biases for some species (Y. Wang et al., 2019). Nevertheless, CAMS reanalysis is valuable for computing climatologies, studying trends, and evaluating models, serving also as a benchmark for other reanalysis and providing boundary conditions for regional models (Inness et al., 2018, 2019).

4.1.3. Normalized Difference Vegetation Index (NDVI)

The Normalized Difference Vegetation Index (NDVI) used for this research was obtained through two datasets, the first covering the period 2003 to 2020 was the Copernicus Global Land Monitoring Service (CLMS) NDVI 1998-2020 (raster 1km) 10 daily version 2 (ECD-GJRC, 2017), and the second covering the period 2021-2023 was the CLMS NDVI 2020-present (raster 300m) 10 daily version 2.

The CLMS NDVI 1998-2020 (raster 1km) - 10 daily - version 2 is a combination of various measurements, from 1998 to 2014 makes use of SPOT-VEGETATION data, and the rest of the period 2014 to 2020 it utilizes data from PROBA-V data to compute long term series of high-resolution spatial NDVI data (Bórnez et al., 2020; León-Tavares et al., 2021). The CLMS uses a Bidirectional Reflectance Distribution Function (BDRF) correction methodology to improve

accuracy and provide quality proof earth observation data (León-Tavares et al., 2021) combined with other methodologies for gap filling to ensure continuity especially for regions with predominant cloud cover (Verger et al., 2015; X. Zhang, 2015). This dataset has been validated using a threshold-based approaches which showed agreement with ground data while deriving phenological data from NDVI to compute start and end of growing season (Bórnez et al., 2020), making it fit to develop climate analysis. The validation process includes the Copernicus Ground Based Observation for Validation (GBOV) that provides high resolution reference maps for evaluating NDVI, hence, actual observations showed that Copernicus Global Land Service products demonstrated strong agreement with reference data, though some biases remained in sparse vegetation and forest environment (L. A. Brown et al., 2020).

The CLMS NDVI 2020-present (raster 300m) - 10 daily - version 2, part of the efforts to ensure continuity of NDVI data availability and vegetation monitoring, provides data at global scale from July 2020 to the present at a spatial resolution of about 300m (ECD-GJRC, 2021). Being made possible through the integration observations from new Sentinel satellites such as the Sentinel-3 crucial for ensuring accuracy and usefulness of the data for global change studies (L. A. Brown et al., 2020; Fuster et al., 2020). Data obtained from the VEGETATION program that includes SPOT-4, SPOT-5, and SPOT-V, is used for directional effects correction, for removing high-frequency noise caused by varying observation and illumination geometries, providing accurate data for analysing temporal and spatial patterns in vegetation indices (León-Tavares et al., 2021). The CLMS's 300m products, including NDVI follow the same methodology for validation with ground observation as the earlier 1km products, thus enhancing its precision and temporal variability, which have been consistent with other satellite products such as MODIS (L. A. Brown et al., 2020; Fuster et al., 2020), ensuring reliability for various application and climate studies (Fuster et al., 2020).

NDVI data from CMLS is widely used for environmental monitoring and land use classification, for example, aiding in producing forest cartography and assessing habitat quality and decay of urban areas (Salata, 2021; Spadoni et al., 2020). Nevertheless, the dataset is crucial for global change studies and provides relevant information on vegetation dynamics and their impact on climate change (M. Li et al., 2023). The availability of high-resolution and frequently updated NDVI data is an asset for detailed analysis of vegetation trends at both local and global scales (Buchhorn et al., 2020; M. Li et al., 2023).

4.1.4. Greenhouse Gases – Methane (CH₄) and Carbon Dioxide (CO₂)

The GHG used in this research comprehend Methane (CH₄) and Carbon Dioxide (CO₂). The methane data was obtained from the CAMS EAC4 described above, while the CO₂ was obtained from the CAMS-EGG4. The CAMS-EGG4 is a reanalysis dataset that includes carbon dioxide (CO₂), amongst other GHG variables, which are crucial for understanding atmospheric dynamics and climate change (CAMS, 2021). The dataset is developed using a self-supervised fusion method that has been developed to address the sparsity of the satellite observations and improve accuracy (Y. Wang et al., 2023). This method integrates data from GOSAT, OCO-2, and CAMS-EGG4 to produce seamless daily global XCO₂ (CO₂ total column mean molar fraction, respectively) products (Y. Wang et al., 2023). The fusion method significantly enhances accuracy, correcting biases in the CAMS-EGG4 products and matching data with independent measurements, providing data that accurately reflects long-term and seasonal changes in CO₂ (Y. Wang et al., 2023). The CAMS-EGG4 CO₂ reanalysis product has been evaluated using ground-based measurements from over 160 stations worldwide, showing that the reanalysis captures general CO₂ distribution features, including seasonal cycles and global trends (Custódio et al., 2022). However, some weaknesses are observed in regions with high anthropogenic CO₂ fluxes, leading to uncertainty and biases, particularly in continental areas with high emissions (Custódio et al., 2022).

The auxiliary variable `co2_vmr_uppertrop` was obtained from the Sounder SIPS: AQUA AIRS IR-only Level 3 CLIMCAPS: Comprehensive Quality Control Gridded Monthly Version 2 (SNDRAQIL3CMCCP_2) dataset. The SNDRAQIL3CMCCP_2 dataset is derived from the Atmospheric Infrared Sounder (AIRS) aboard NASA's Aqua satellite (Barnet, 2019), and utilizes the CLIMCAPS (Community Long-term Infrared Microwave Coupled Product System) algorithm, which applies an Optical Estimation approach to retrieve atmospheric parameters such as temperature, water vapor, ozone, carbon dioxide, carbon monoxide, sulphur dioxide, and methane (Monarrez, 2021; Smith & Barnet, 2019). The dataset provides gridded monthly averages with global coverage at a 1° x 1° (latitude x longitude) resolution. The validation process for the SNDRAQIL3CMCCP_2 dataset follows a process that includes comparisons with other satellite and ground-based observations, with uncertainty estimates included to account for instrumental calibration, retrieval assumptions, and atmospheric conditions (Smith & Barnet, 2019). Nonetheless, some factors, such as thick cloud cover, aerosol loading, and instrumental anomalies, remain challenges to data quality improvement (Barnet, 2019; Smith & Barnet, 2019). This dataset is widely used in climate research, offering

a platform for analysing the distribution and variability of atmospheric constituents related to climate change, while serving as a valuable data source for atmospheric studies composing different layers of the atmosphere and serves as a benchmark for validating atmospheric models improving their skill for modelling atmospheric dynamics (Barnet, 2019; Smith & Barnet, 2019). This dataset was used to estimate CO₂ total column mean molar fraction using Linear Regression Methods, which offers an algorithm to estimate a variable by its predictors, applying exponential factors to consider non-linear interactions. With the CH₄ obtained from CAMS EAC4, this variable is essential for modelling the interaction between GHGs and climate.

4.2. Data preprocessing

Data preprocessing will be performed to ensure data quality and relevance. This preprocessing includes several steps. All datasets will be converted to annual summaries and resampled to 0.75°x0.75° spatial resolution. If the dataset is large, the data is cleaned by removing missing values. Missing values were filled using the Last Observation Carried Forward (LOCF) Method.

4.3. Spatial Variability, Trends, and Homogeneity

The study aims to thoroughly investigate the spatial variability of trends and the homogeneity of each variable across the vast African continent. This analysis will explore Africa's diverse geographical and climatic regions to understand how different variables behave spatially. By examining trends, the study seeks to identify any patterns or shifts in these variables over space and time, shedding light on potential regional differences or similarities. Additionally, assessing homogeneity provides insights into the consistency and uniformity of these variables across various locations, helping to determine if there are any significant disparities or if they exhibit a coherent pattern across the continent. Through this comprehensive spatial analysis, the study intends to contribute valuable knowledge regarding Africa's environmental and climatic dynamics. The trend analysis is conducted using the Mann Kendal's and the Sens slope estimator, while homogeneity is examined using the Buishand test.

The Mann Kendall test is widely applied in climate and environmental studies as a non-parametric statistical method for detecting monotonic trends in time series data without requiring normality or linearity assumptions. It evaluates the null hypothesis of “no trend” against the alternative hypothesis of a monotonic increasing or decreasing trend by comparing the relative magnitudes of sample data points over time (F. Wang et al., 2020). The test statistic

(S) is computed by comparing all pairs of observations, where positive differences indicate an increasing trend and negative differences indicate a decreasing trend. For large datasets, S follows a normal distribution, and a standardized Z-score is used to assess statistical significance. A significant Z-score indicates the presence of a trend, with results interpreted based on predefined significance levels.

Sen's slope, also called the Theil-Sen estimator, estimates the slope of a trend line in a time series. It is useful, particularly for data that may not meet the assumptions for parametric methods. The Sen's slope is calculated as the median of all possible pairwise slopes between data points in a time series, making it robust to outliers and suitable with non-normal distributions (Akritas et al., 1995; Sievers, 1978; Vannest et al., 2012). Its strengths make it widely used in environmental and atmospheric sciences, where data often exhibit autocorrelation and non-normality. It is capable of handling censored data, which is common in open-source datasets. It involves using a version of Kendall's tau statistic to accommodate the censored nature of the data (Akritas et al., 1995).

The homogeneity test for time series in this study is based on the Buishand test, a statistical method designed to detect breaks in data consistency. This test identifies abrupt shifts in the means of observations, which may indicate changes in the data collection process or climatic variations. It relies on the cumulative sum of deviations from the mean and compares the results to critical thresholds to assess the presence of structural changes. Widely applied in climatology and hydrology, the Buishand test ensures data reliability before performing trend analysis.

4.4. Statistical Modelling

Three statistical models will be used to analyze the causality between the variables (Laban et al., 2020): the multivariate linear regression (MLR), Principal Component Analysis (PCA) and Regression (PCR), and Generalized Additive Model (GAM). All the statistical models will be performed interactively to determine the variables' dependency. The statistical modeling methods utilized in this research aimed to examine the primary variables affecting ozone distribution over industrial zones in South Africa. These methods have proven to be excellent for statistically analyzing interactions between climate elements, both locally and especially.

4.4.1. Multivariate Linear Regression (MLR)

The MLR uses a standard equation (Equation 1; Laban et al., 2020) which describes the response of the variable Y to the explanatory variables $X_1; X_2; \dots X_p$ with the regression coefficients $\beta_1; \beta_2; \dots \beta_p$ and the ε error term or residual value represents the difference between the observed and modeled values.

$$Y_i = \beta_0 + \beta_1 X_{i1} + \beta_2 X_{i2} + \dots + \beta_p X_{ip} + \varepsilon_i \quad (1)$$

The method suggests applying the Ordinary Least Squares procedure to determine the coefficients and the Root Mean Squares Error, R-squared, and adjusted R-squared to determine the residual effects.

4.4.2. Principal Component Analysis (PCA)

The PCA was used to analyze the dependencies between the most related variables (total ozone layer column, temperature, precipitation, water vapor, GHGs, wind, and, aerosol optical depth), and explain the variables that have the greater influence on the variability of the dataset. The general equation describing PCA is presented in Equation 2 (Laban et al., 2020).

$$Z_i = a_{i1}X_1 + a_{i2}X_2 + a_{i2}X_2 + \dots + a_{ip}X_p \quad (2)$$

Where Z_i is the principal component, “a” is the component loading, and “X” is the measured variable.

To determine the influence of each principal component, a single variable linear regression was performed, and the R and R-squared coefficients were determined.

4.4.3. Generalized Additive Model (GAM)

Generalized Additive Models (GAMs) expand upon traditional linear models by accommodating response variables with non-normal error distributions and allowing for non-linear relationships between dependent and independent variables. In GAMs, the response variable is modelled as an additive combination of smoothing functions of individual predictors, which can be either parametric or non-parametric. The model equation involves an intercept, smooth functions for each predictor, and an error term (Equation 3; Laban et al., 2020).

$$g(E(Y_i)) = \beta_0 + s_1(X_{i1}) + s_2(X_{i2}) + \dots + s_p(X_{ip}) + \varepsilon_i \quad (3)$$

Where, Y_i is the response variable, $E(Y_i)$ denotes the expected value and $g(.)$ is the link function that links the expected value to the predictor variables X_{i1}, \dots, X_{ip} , β_0 is the intercept and ε_i is an independent and identically distributed random error.

Unlike Multiple Linear Regression (MLR), GAMs utilize a back-fitting procedure to control the effects of other predictors, enabling the identification of relevant covariates without prior knowledge of their relationship to the response variable. Smooth parameters are automatically selected using the Akaike information criterion (AIC), ensuring the best-fitting model. Evaluation of GAMs includes metrics such as R-squared values and generalized cross-validation scores.

4.5. Modelling variables and Training and Validation datasets

All the statistical and machine learning models training was done using data from 2003 to 2020 (80%), and the remaining 2021 to 2023 (20%) were used for model validation and accuracy determination. All the models were built to assess the contribution of each of the analysed variables in temperature, precipitation, ozone and NDVI variation. The accuracy of the models was assessed using R-squared and mean absolute error between the modeled values and the observed values.

5. Results and Discussions

5.1. Results Description

5.1.1. Estimation of CO₂ total column mean molar fraction

The mean molar fraction of the total CO₂ column obtained from the EGG4 reanalysis spanned only 17 years (2003 – 2020) of the study period. Consequently, for a thorough analysis conducted in this research, the CO₂ column was estimated using the auxiliary CO₂ volume mixing ratio in the upper troposphere, referred to as auxiliary data (CO₂), through linear regression modeling. The data from 2003 to 2017 was utilized to train the model, while the remaining data from 2017 to 2020 served for testing and validation. Polynomial interactions were applied, extending from the simple linear model to the sixth degree (Bihexic) to account for non-linearity among the variables. Subsequently, we employed the best model fit to estimate CO₂ using the auxiliary CO₂ data, covering the entire study period (2003 – 2023). The model training for CO₂ estimation was conducted in the R environment utilizing the base *lm()* function.

Training results for CO₂ (Figure 8) indicate that the quintic polynomial (5th degree; Figure 8.e) exhibited the best performance among the trained models, with an MAE of 0.63628 CO₂-ppm and an R-squared value of 0.97993 (97.99% fit to the EGG4 CO₂ test data). Therefore, it was deemed suitable to estimate the CO₂ total column mean molar fraction for the entire study period (2003 – 2023).

Studies using Polynomial Linear Regression have shown that polynomials with orders higher than one tend to be more accurate in data modeling and are widely used for data filling, providing an effective platform for representing missing data. While linear regression is straightforward, it may not capture complex interactions within the dataset (Siemsen et al., 2010). Quadratic regression, which accounts for parabolic interactions, can better handle intricate interactions in the dataset (Sipakov et al., 2024; Sun & Wang, 2020; C. Wang et al., 2019; Yao & Müller, 2010) while managing relationships between variables (C. Wang et al., 2019). Cubic and higher-order polynomials can capture more complex non-linear relationships, enabling the modeling of data with multiple inflections and providing flexibility in adapting to structural changes (Poirier, 1973; Simon, 1989). Nevertheless, there is a need to balance overfitting and model complexity (Sipakov et al., 2024; Tanaka & Lee, 1998), leading to the use of a limited order of polynomials during model training. Regarding model performance, numerous studies in regression analysis indicate that an R-squared value exceeding 90% is

suitable for data forecasting or estimation (Athey et al., 2019; Genuer et al., n.d.; Probst et al., 2018; Schonlau & Zou, 2020; Sipakov et al., 2024).

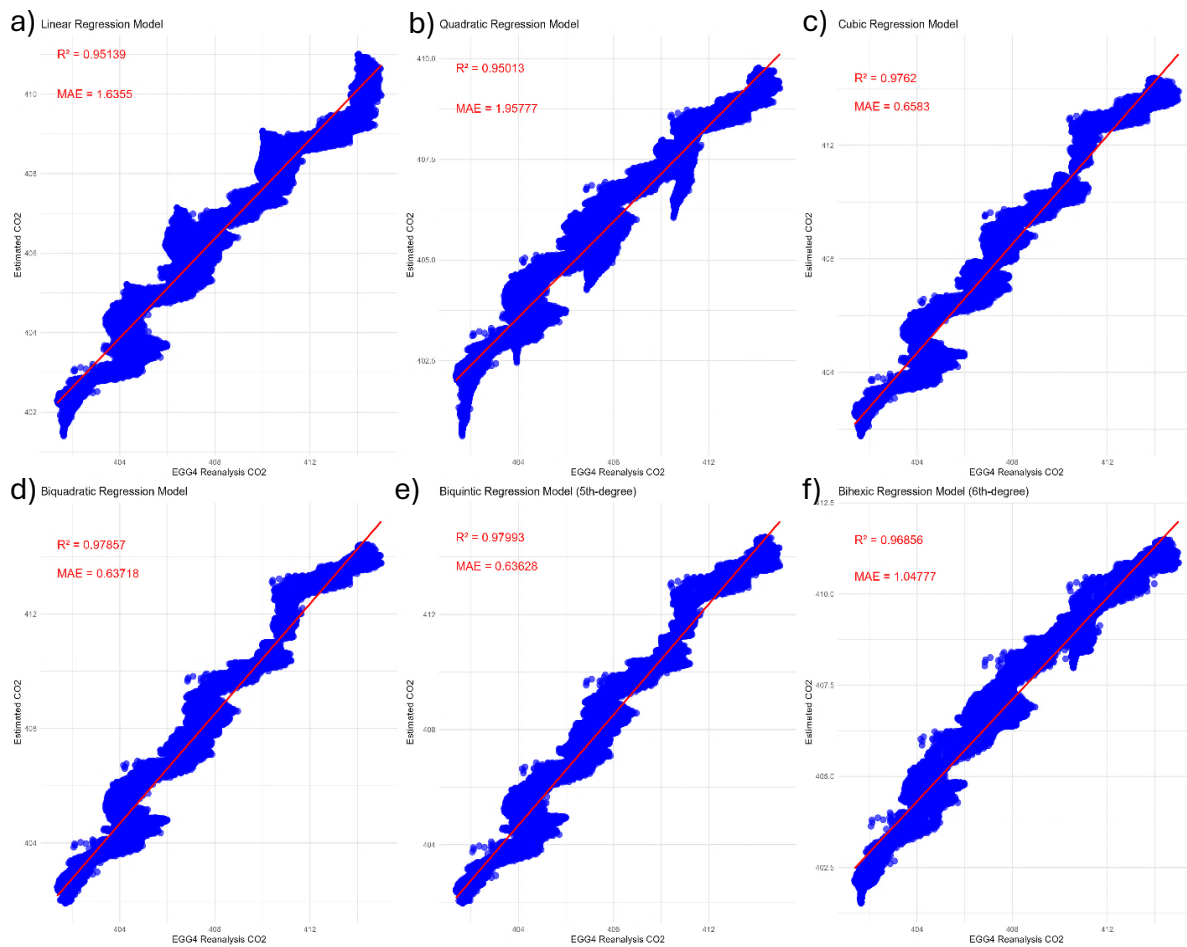


Figure 8. Validation results results for different linear regression polynomial models, with the biquintic model (e) showing the best performance in estimating CO₂, were used for the analysis in this work.

5.1.2. Descriptive Summary of the Dataset

Figure 13 presents a descriptive summary of the dataset used for the analysis carried out in this work. The variables show varied distributions, with outliers observed in most analyzed variables. For a summary of the dataset, the study area was divided into three (3) central regions: the northern region ranging from 37°N to 13°N, the central region from 13°N to 11°S, and the southern region ranging from 11°S to 35°S (Figure 9).

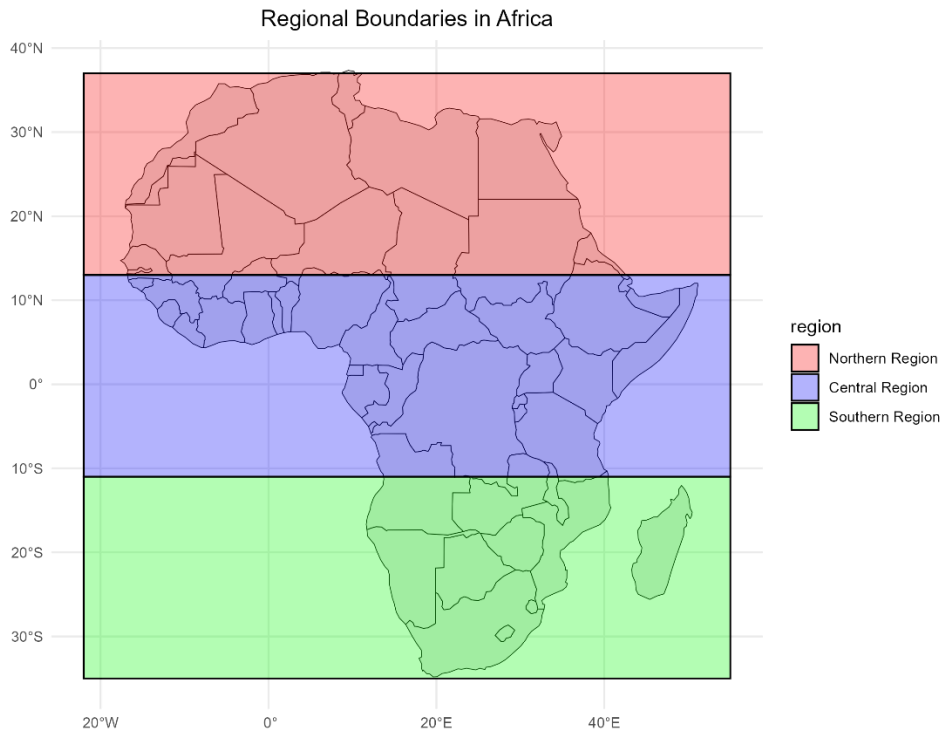


Figure 9. Study Area Regional Boundaries for Dataset Description

a. Northern Region

In the Northern Region (Figure 10), the annual temperature shows a median of around 25°C, with the first quartile around 22°C and the third around 27°C (Figure 10.a). Outliers ranging from about 10°C to 13°C suggest some cooler temperatures in various areas over the years. The precipitation values (Figure 10.b) exhibit a highly skewed distribution, with a long upper whisker and numerous outliers that start from around 2100 mm/year and above, indicating that precipitation in Northern Africa is highly variable, with some locations experiencing extreme rainfall events. The first quartile, close to 1 (all precipitation values below 1 mm/year were removed), indicates regions with low or no precipitation throughout the year. The median, approximately 400 mm/year, and the third quartile, around 900 mm/year, suggest that most of Northern Africa observes low to moderate rainfall values below 1000 mm/year. Mean sea level pressure (Figure 10.c) showed a narrow spread, indicating low variability in atmospheric pressure. The median pressure, close to 101,350 Pa, reflects values near the standard sea-level atmospheric pressure, with no outliers present. Water vapor (Figure 10.d) demonstrates a large spread, showing high variability in concentration, with the first quartile around 1750 ppm, the median near 2400 ppm, and the third quartile at 3350 ppm. With no outliers, some extremely high values above 5000 ppm indicate regions with high humidity. The values for CO₂ and CH₄

(Figure 10.e and f) exhibit highly symmetric patterns, with median values close to 393 ppm for CO₂ and 1.79 ppm for CH₄, showing relatively small variation and no outliers, which suggests that the concentrations of CO₂ and CH₄ were relatively stable across estimations. Ozone (O₃) concentrations (Figure 10.g) demonstrate some extreme values above 295 DU (Dobson Units), indicating regional variations in stratospheric ozone, possibly due to seasonal effects or pollution. The first quartile is close to 265 DU, the median is 269 DU, and the third quartile is approximately 278 DU, reflecting the prevalence of normal, low variability in ozone concentrations over the years. Aerosol properties (Figure 10.h and i), including Aerosol Optical Depth at 550 nm (AOD₅₅₀) and 865 nm (AOD₈₆₅), revealed right-skewed values, with numerous outliers at the upper whisker. The interquartile ranges from about 0.12 to 0.32 for AOD₅₅₀ and from about 0.08 to 0.24 for AOD₈₆₅, with the median close to 0.22 and 0.15, respectively. Outliers indicate that some regions experience significantly higher aerosol pollution, possibly due to wildfires, dust storms, or industrial emissions. The NDVI values (Figure 10.j) primarily range from ~0.20 to ~0.82, with a median around ~0.54, suggesting a mix of moderate to dense vegetation in this region. The wind components U and V values (Figure 10.k and l) show symmetric distributions around 0, with positive and negative outliers, and the V component is predominantly negative, indicating that winds are generally low with some regional or occasional extreme gusts.

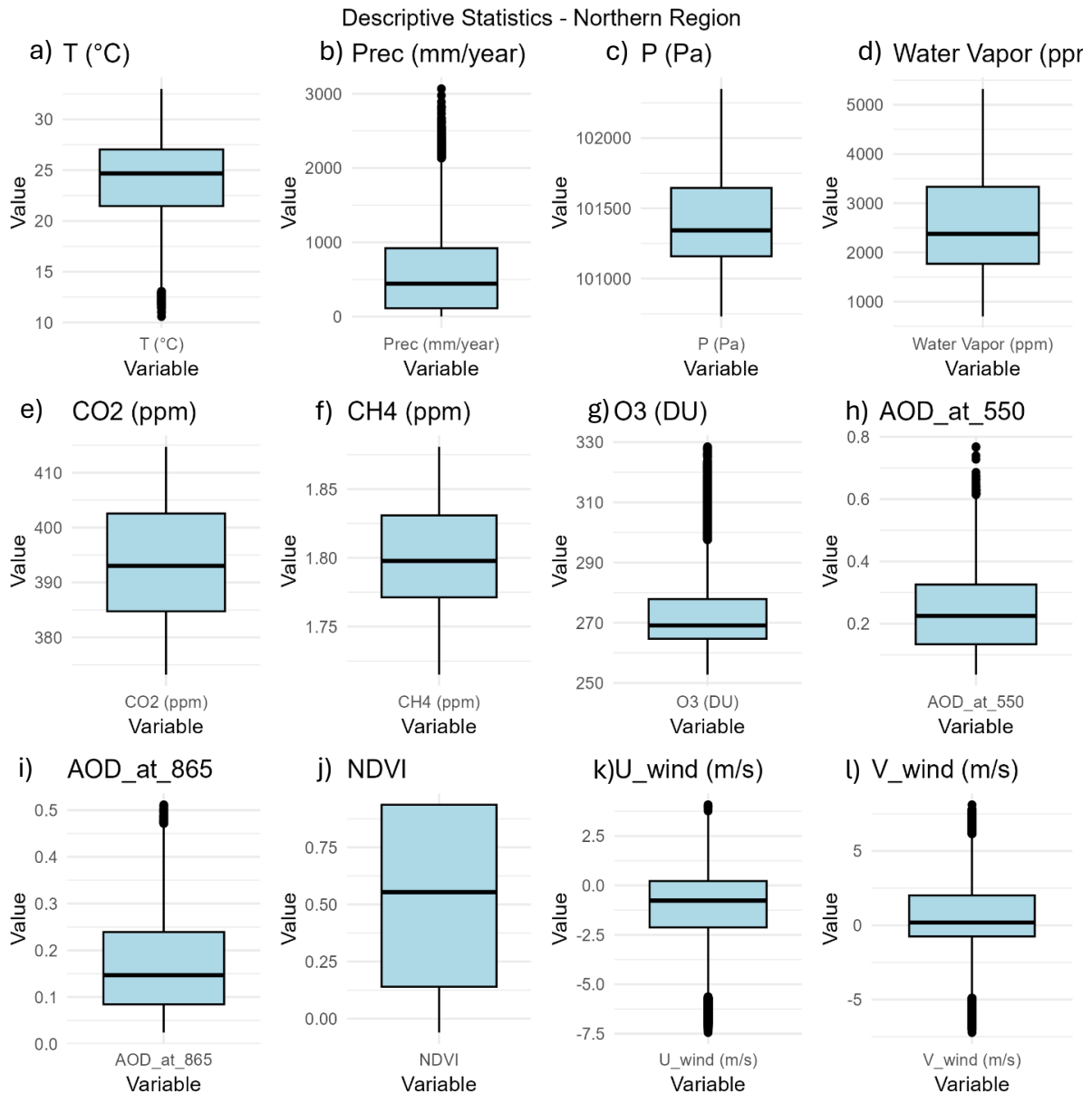


Figure 10. Provide a general description of the dataset in the Northern Region. The signs of U and V wind represent the direction of the wind, and the module represents the strength of that component. For the U wind, the negative sign represents the westward winds, and the positive sign represents the eastward winds. For the V wind, the negative sign represents the southward wind, and the positive sign represents the northward wind.

b. Central Region

A slight change in the boxplots is observed across the central region (Figure 11) across the variables. The temperature variability (Figure 11.a) was similar to that observed in the northern region, with the first quartile around 23°C, the median around 25°C, and the third quartile around 27°C. However, the minimum outlier observed in this region is around 11°C, 1°C higher

than in the northern region. The precipitation pattern (Figure 11.b) also exhibits a highly skewed distribution, with a long upper whisker and numerous outliers that start from around 2100 mm/year and above, with one isolated outlier around 3400 mm/year, suggesting the existence of regions with intense extreme rainfall. With the same interquartile variability as in the northern region, the central region mostly observes low to moderate rainfall values below 1000 mm/year. The mean sea level pressure (Figure 11.c), Water Vapor (Figure 11.d), CO₂ (Figure 11.e), and CH₄ (Figure 11.f) present the most precise similarity with the northern region, with no easily detected differences. Ozone levels (Figure 11.g) show a slight difference compared to the values observed in the northern region. The minimum value around 253 DU is approximately 1 DU higher than the minimum in the northern region (~252 DU). While the interquartile variability is similar, the third quartile is slightly lower (~277 DU), and the maximum outlier also is lower in this region ~328 DU, compared to ~330 DU in the northern region. This pattern suggests a slightly lower variability of ozone concentrations in the central region compared to the northern region. Aerosol Optical Depth at 550nm (AOD_550; Figure 11.h) showed a similar interquartile variability as in the northern region; nevertheless, more outliers in the upper whisker were shown by the increased number of points compared to the northern region. Aerosol Optical Depth at 865nm (AOD_865; Figure 11.i), similarly to the AOD_550, was shown to have the same interquartile variability as the AOD_865 in the northern region, however, with fewer outliers in the upper whisker, where the maximum value was ~0.48. This suggests an increase in the availability of aerosols captured at 865nm and a reduction in those observed at 550nm. The NDVI (Figure 11.j) values show a similar statistical distribution as in the northern region, with almost undetectable changes. However, a slight increase in the first quartile suggests that vegetation in this region is denser than in the northern region. The wind components U and V (Figure 11.k and l) showed a slight change, where the U component showed a slight decrease and the V component increased, mainly for the outliers. The U component observed a maximum outlier slightly above the -0.75m/s mark, which was less than the maximum observed in the northern region, which surpassed this mark (the negative sign in the velocity expresses the direction to the south and the positive to the north). The same pattern was observed in the upper whisker, where the values were more concentrated around the 2.75m/s mark. The V wind, on the other hand, showed an increase in the Eastward winds (positive V wind value), as shown by the outliers that were above 0.6 m/s compared to the northern region, which was closer to 0.5 m/s. The lower outliers did not observe much change, ranging both from ~ -0.5 m/s to ~ -0.7 m/s.

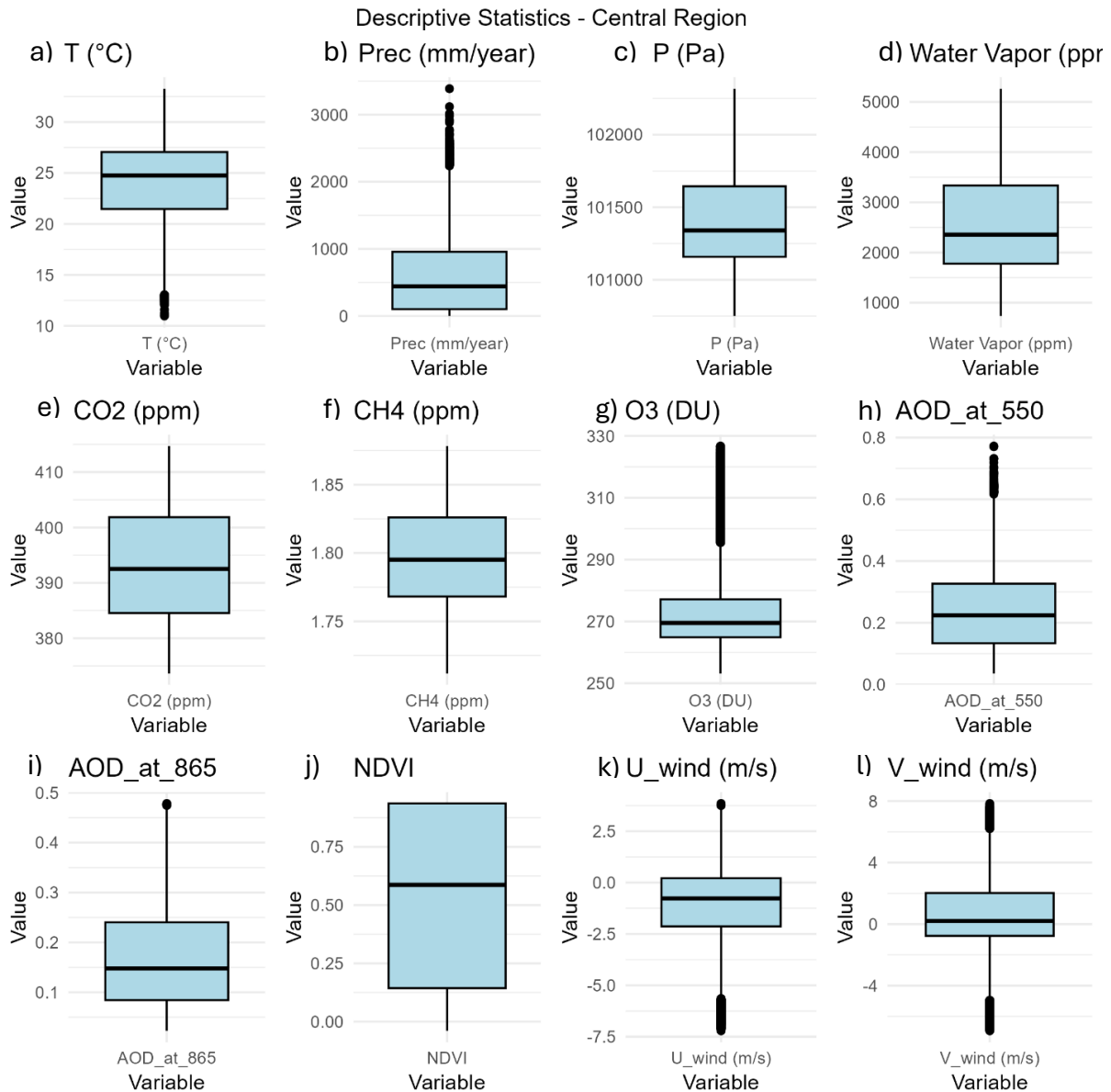


Figure 11. Provide a general description of the dataset in the Central Region. The signs of U and V wind represent the direction of the wind, and the module represents the strength of that component. For the U wind, the negative sign represents the westward winds, and the positive sign represents the eastward winds. For the V wind, the negative sign represents the southward wind, and the positive sign represents the northward wind.

c. Southern Region

In the southern region (Figure 12), a slight change was observed in the statistical variability of the dataset. The temperature values (Figure 12.a), although following the interquartile patterns observed in the northern and central regions, have the lowest outlier touching 10°C , which is the lowest temperature observed in the dataset. The precipitation (Figure 12.b) values with the

same interquartile variability as for the other regions analyzed show a slight difference on the outliers, while they are more concentrated than in the central region, they were less concentrated than in the northern region, suggesting that in the northern and southern region there is more precipitation variability than in the central region. The mean sea level pressure (Figure 12.c) observed a slight decrease in the minimum pressure, which crossed 100750Pa, while in the northern and central regions, the minimum pressure was above this mark. The statistical variability for the Water Vapor (Figure 12.d), CO₂ (Figure 12.e), and CH₄ (Figure 12.f) is similar to that observed in the northern and central regions, with no easily detected changes. Ozone levels (Figure 12.g) showed a similar interquartile variability as observed in the northern and southern regions. However, the outliers observed were lower, ranging from ~ 298DU to ~ 325DU, suggesting a lower variability than the other two regions. AOD₅₅₀ (Figure 12.h) observed a similar pattern in the central region with a slight decrease in the maximum outlier; the same was observed for AOD₈₆₅ (Figure 12.j). The NDVI values (Figure 12.j) show a similar statistical distribution as in the northern region, with almost undetectable changes. However, a slight increase in the first quartile suggests that vegetation in this region is denser than in the northern region. The wind components U and V (Figure 12.k and l) showed a slight change. The U component was similar to that observed in the northern region, slightly surpassing the -0.75m/s mark. Meanwhile, in the upper whisker, the values were more concentrated around the 2.75m/s mark. The V wind, on the other hand, showed a similar pattern to the northern region in the Eastward winds (positive V wind value), as shown by the outliers that were close and above 0.6 m/s. The lower outliers did not observe much change, ranging from ~ -0.48 m/s to ~ -0.78 m/s.

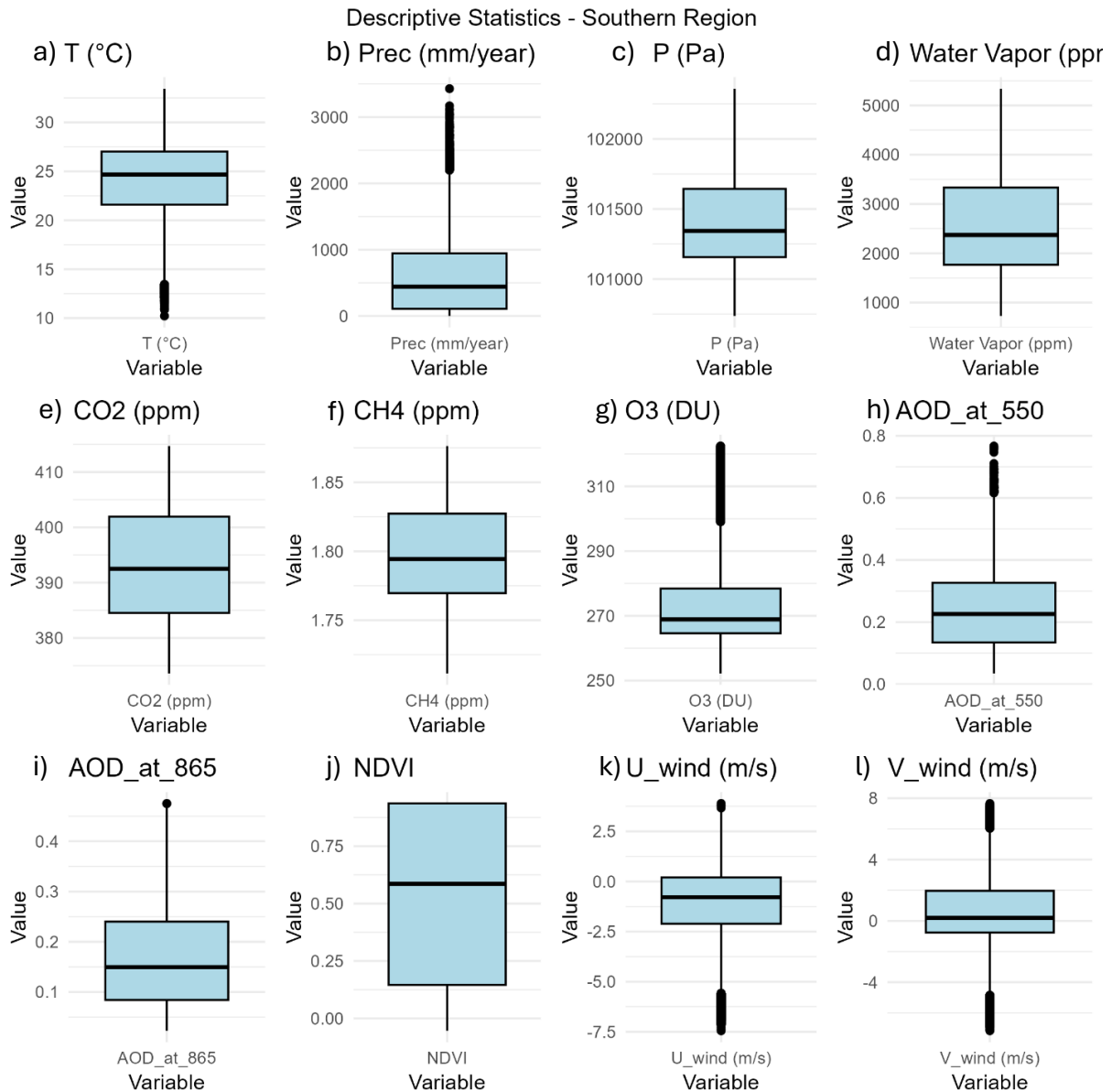


Figure 12. Provide a general description of the dataset in the Southern Region. The signs of U and V wind represent the direction of the wind, and the module represents the strength of that component. For the U wind, the negative sign represents the westward winds, and the positive sign represents the eastward winds. For the V wind, the negative sign represents the southward wind, and the positive sign represents the northward wind.

5.1.3. Spatial Variability

Figure 13 presents a spatial means for the annual values observed from 2003 to 2023. The mean annual temperature (Figure 13.a) values range from 10°C to approximately 32°C. The hottest regions are represented in northern Africa's Sahara and Sahel regions. A small strip in northern Africa experiences annual temperatures close to 16°C. The central region variability of regions

observing high temperatures and regions experiencing low temperatures. In this region the mean annual temperatures are between 16°C and 24°C. The coolest annual temperatures are observed in the southern region, especially in parts of South Africa and Lesotho, with mean annual temperatures below 16°C.

The mean annual precipitation (Figure 13.b) observes a distinct pattern. In the northern parts of southern and eastern central Africa, rainfall is scarce, with precipitation values close to 1mm/year, suggesting that these regions have been experiencing severe droughts during the study period. In the central and western southern regions, mean annual precipitation values range from 500 mm/year to ~2500 mm/year, and the highest mean annual values were observed in central Congo and the last tip of West Africa.

The mean sea level pressure (Figure 13.c) also presented a similar distinct pattern, where the lowest mean annual pressure was observed in parts of Congo and the Sahel region and the horn of Africa, with mean pressure values ranging from 100800Pa to ~101100Pa. High pressure values were observed above the Sahel region and southern Africa, ranging from ~101400Pa and above.

Mean annual water vapor values (Figure 13.d) follow a similar pattern to precipitation with some minor differences. Northern Africa, starting from the Sahel region, the south and west of southern Africa, and parts of West Africa and central Madagascar experience low water vapor values close to 1000ppm to approximately 2000ppm. The highest water vapor values were observed in the central region of Africa and west southern Africa, including Madagascar, with values ranging from ~3000ppm and above, the highest values above 5000ppm observed in west Africa.

The mean CO₂ values (Figure 13ef) show a gradient increasing from south to north, with the minimum values approximately 395 ppm in the southern tip and maximum values 399 ppm in the northern tip. Methane concentrations follow a more local variability, where singular portions in southern Africa, East Africa, and Northern Africa observe CH₄ values below 1.4 ppm. The remaining regions observe CH₄ values (Figure 13.f) ranging from 1.5 ppm to approximately 1.8 ppm.

Mean annual ozone values (Figure 13.g) also follow a gradient distribution, where the lowest values (~259DU) are concentrated in central Africa and increase northwards and southwards. Ozone values in the northern tip are approximately 320DU, and in the southern tip of Africa, they are approximately 280DU.

Mean annual AOD₅₅₀ values (Figure 13.h) follow an apparent gradient pattern, where in the southern and east Africa AOD₅₅₀ values are close to 0.2 and below. The eastern northern region follows this region, registering values ranging from 0.2 to 0.4, and the highest values are observed in the Western Sahara and West Africa, with values ranging from 0.4 and approximately 0.68. A small trip in northern Africa observed values close to 0.2. However, the mean annual AOD₈₆₅ (Figure 13.i) followed a similar pattern to the AOD₅₅₀, with lower values. In the southern and western regions, values ranged from 0.1 to below. Meanwhile, values in the eastern northern region ranged from 0.2 to 0.3, and the maximum values in West Shara, Sahel, and West Africa ranged from 0.3 to approximately 0.44. The small trip observed in northern Africa had AOD₈₆₅ values of approximately 0.15.

NDVI values (Figure 13.j) were observed at their peak in the central region of Africa and southeastern Africa, with NDVI exceeding 0.75. The lowest values were noted in northern Africa, particularly in the Sahel region and northwards, as well as in the western parts of Namibia and South Africa and parts of the Horn of Africa, where NDVI values fell below 0.25. Nevertheless, some areas of the Sahel and northern Africa exhibit very localized high values in the mean annual NDVI of approximately 0.75.

The wind pattern (Figure 13.k) show the predominance of northward and eastward winds. Wind Seep and Direction showed a variable pattern across centers of divergence and convergence. In North Africa, winds are generally in the southwest direction, with high wind speed values in the western and eastern regions of the Sahara Desert, with wind speeds reaching over 5m/s. The upper northern part of Africa wind direction is predominantly southeastward, with wind speed ranging from around 1m/s on the west to around 3m/s. Right below the Sahel region, a small belt that forms a convergence between winds flowing from the north and the winds flowing from the south is observed, forming a wind in the westward direction with wind speeds of approximately 1m/s. The west Africa region observes winds coming from the ocean inside the continent reflecting the West Africa monsoon, with wind speeds of approximately 2m/s. In the central region of Congo, a divergence center is observed with wind speed lower than 1m/s. In the East Africa region, including the horn of Africa and eastern parts of South Africa, wind blows from the Indian ocean westwards with a speed of approximately 2m/s to 4m/s. In northern Southern Africa, westward winds with 4m/s in the interior and 1m/s on the coast are predominant. Finally, in the southern tip of Africa winds are predominantly southeastward with a convergence belt with northeastward winds along the coastline. Wind speed are predominantly between 1m/s to 2m/s.

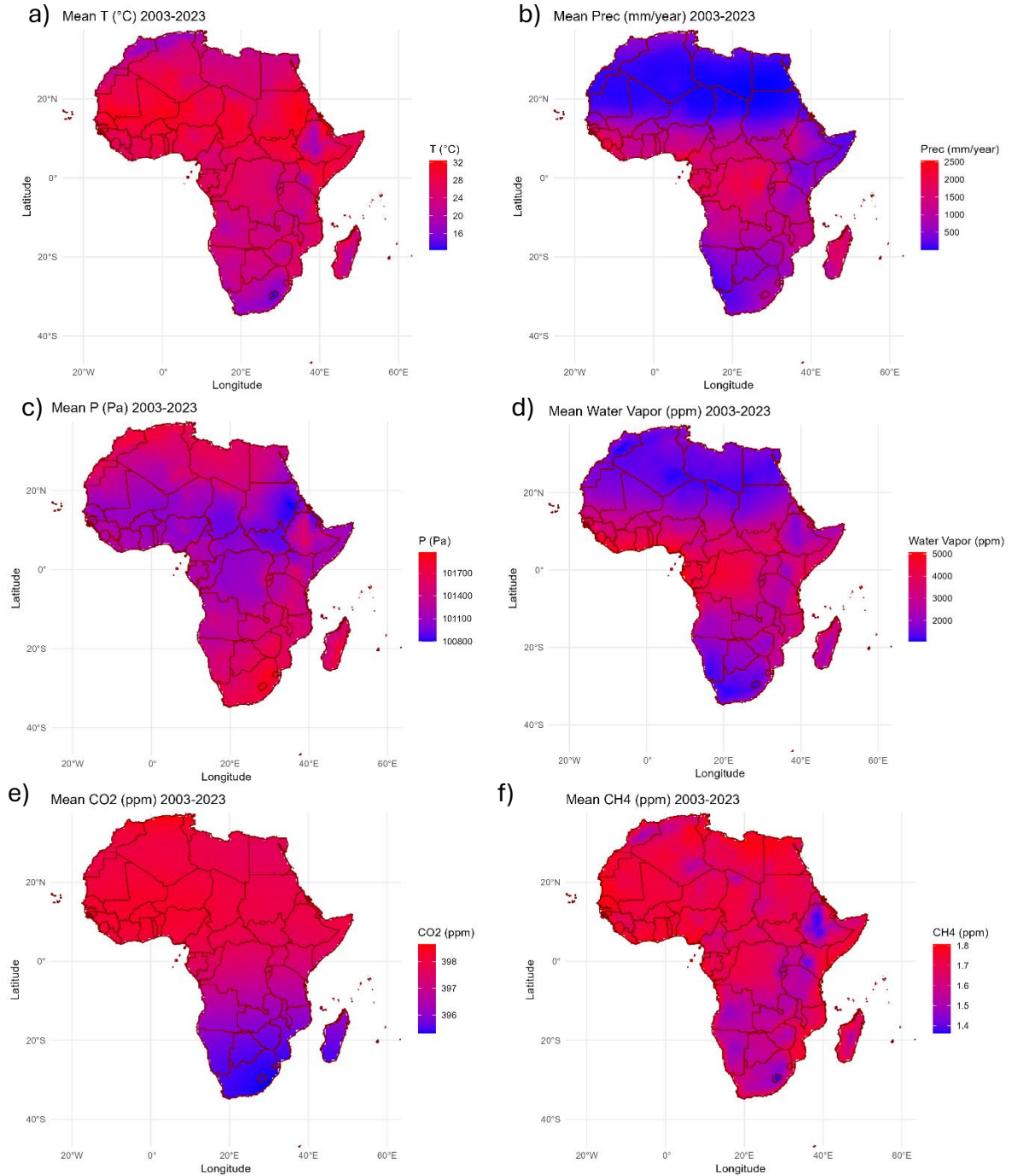


Figure 13. Mean annual values for the variables analyzed are presented. A unique analysis is conducted on the Mean Wind Speed and Direction, where the wind speed is calculated using the formula for vector direction resultant: $w = \sqrt{u^2 + v^2}$, where w represents the wind speed, u is the U wind component, and v is the V wind component (j , in the Figure 13-continued).

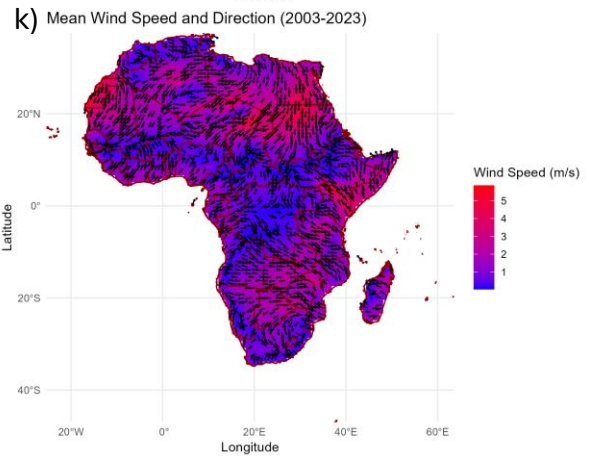
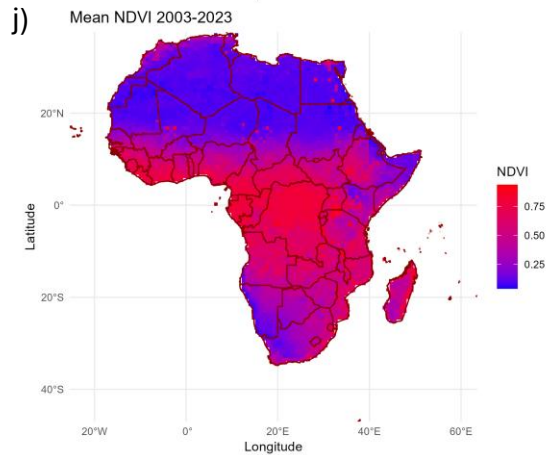
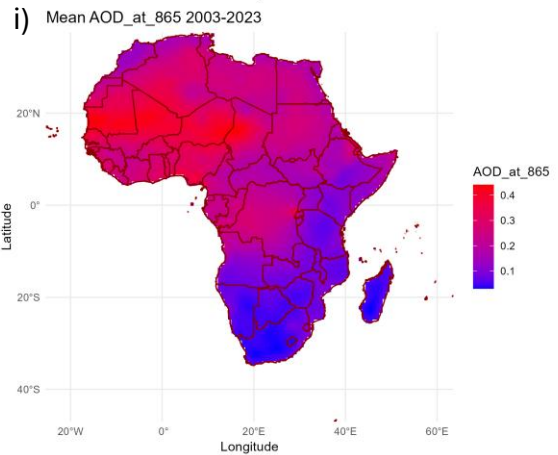
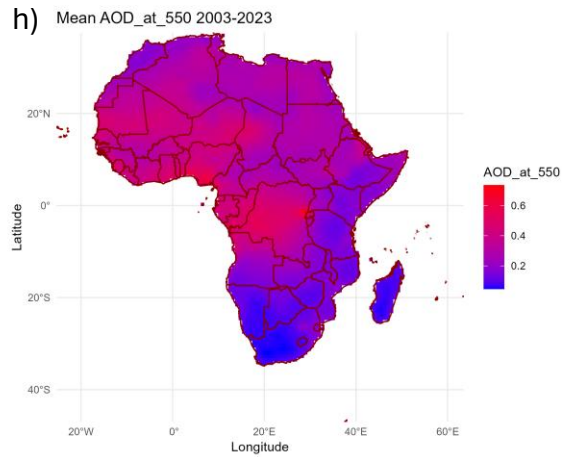
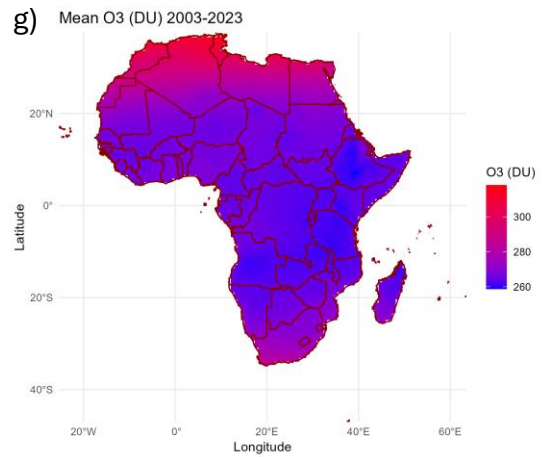


Figure 13. Continued.

5.1.4. Trend Analysis and Homogeneity for Temperature, Rainfall, TCO, and NDVI

a. Annual Mean Temperature

Figure 14 presents trend analyses. We present trend analysis details for only the four main variables of interest: Temperature, rainfall, TCO, and NDVI, arranged in sequence. For Annual mean temperature, the Mann Kendall result (Figure 14.a) showed that the majority (59.21%) of the continent experienced temperature increase comprehending areas in Madagascar, central Africa, the border in southern Africa, and northern Africa. Approximately 40.68% of the continent showed no significant temperature trend, including southern Africa, East Africa, the Sahara Desert, and a small tip of southern Madagascar. Only 0.11% exhibited a decrease in temperature, according to the Mann-Kendall test, corresponding to a small tip in western south Africa, and eastern West Africa.

The results from Sen's Slope analysis (Figure 14.b) indicate significant temperature increases in specific regions, while most areas exhibit minimal or no change. The most notable warming trends are observed in 28.1% of the continent, where temperatures rise between $+0.05$ °C/year and $+0.10$ °C/year. Additionally, a smaller but substantial 0.77% of the territory experiences an increase of $+0.10$ °C/year to $+0.15$ °C/year, with localized hotspots in the eastern Sahara and the western part of southern Africa reaching $+0.15$ °C/year to $+0.20$ °C/year (0.04% of the total area). In contrast, 57.8% of the African territory, primarily covering the Sahara Desert and parts of southern and eastern Africa, shows only a slight warming of 0 to $+0.05$ °C/year. Areas experiencing cooling are negligible, with a minor 0.4% of the continent displaying a weak negative trend, at most -0.05 °C/year.

The Buishand Test for change point detection (Figure 14.c) revealed significant shifts in temperature trends in specific periods and regions. The most notable changes occurred between 2013 and 2018, affecting 35.4% of the continent, including southern Africa, Madagascar, Central Africa, the eastern coast of Africa, the Horn of Africa, and parts of the Sahara and northern Africa. A smaller but still relevant shift was detected between 2008 and 2013, covering 5.2% of the continent, mainly in the interior of East Africa. In contrast, the majority of the continent (59.3%) showed no detected change point, indicating either a long-term temperature increase predating the study period or no significant trend. No temperature trend shifts were observed between 2003 and 2008, and only a negligible 0.11% of the continent experienced a change between 2018 and 2023, mainly in localized areas of the Sahel and northern Algeria.

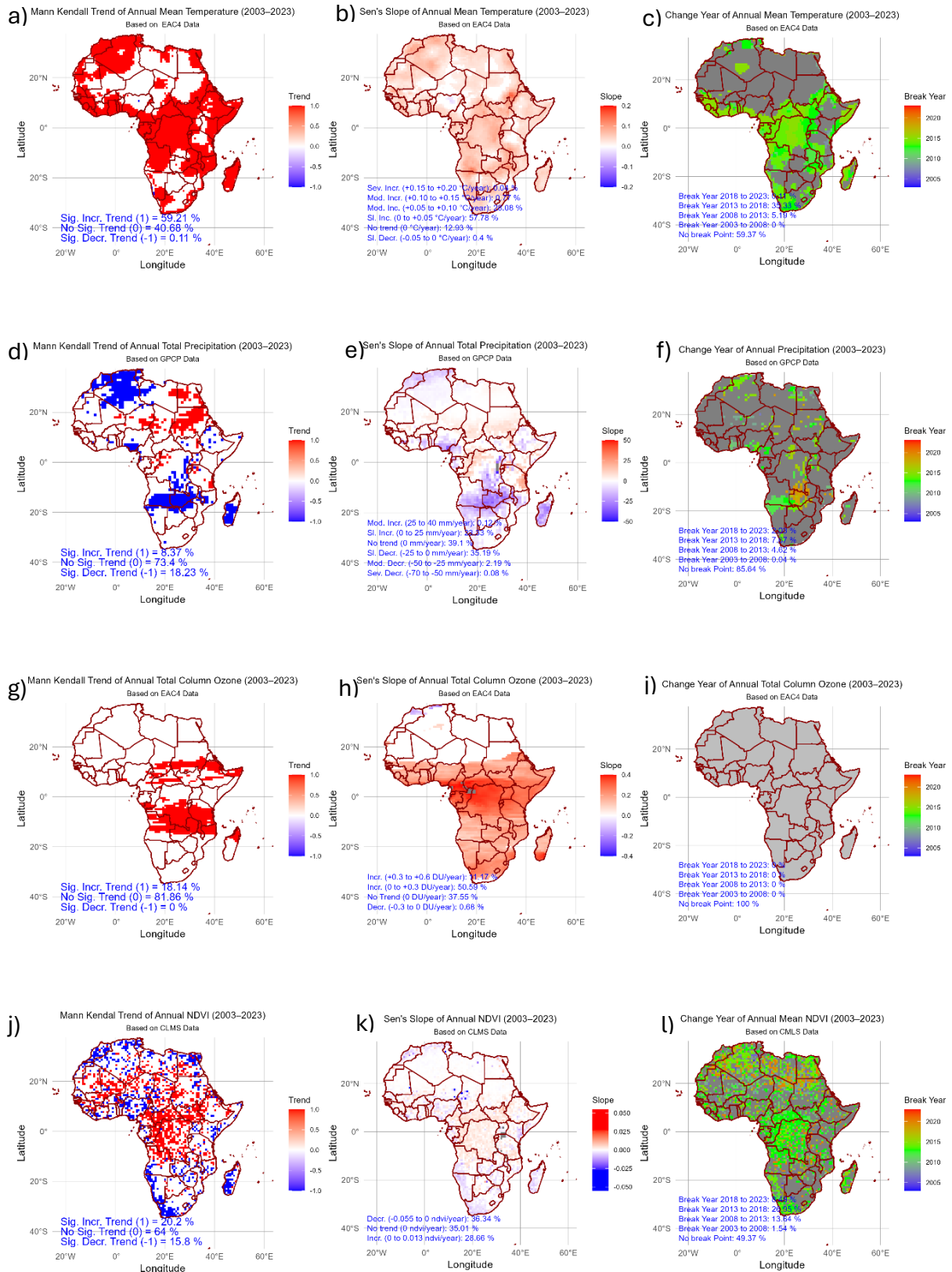


Figure 14. Trend Analysis for Annual Temperature, Precipitation, TCO, and NDVI. For the homogeneity test, the gray color on the map represents homogeneous series that do not exhibit a breakpoint or loss of stationarity.

b. Annual Precipitation

Trend results for the annual precipitation show a variable pattern across the continent (Figure 14.d, e and f). Mann Kendall results (Figure 14.d) show a quasi-even distribution between areas with a significant increasing trend (8.4%) and areas with a significant decreasing trend (18.3%), while areas with no significant trend account for most of the continent with (73.4%). Significant decreases in precipitation were observed in southern Africa, Madagascar, and minor parts of West and East Africa, as well as West North Africa. The areas with significant increases in precipitation include parts of central and eastern Sahara, central Africa, and some regions along the coastal areas of East Africa around Tanzania.

Sen's Slope analysis (Figure 14.e) highlights significant variations in rainfall trends across Africa. The most notable change is the decrease in rainfall, which affects 37.5% of the continent. Within this, 35.2% experienced a decline between 0 and -25 mm/year, while a smaller but substantial 2.2% saw a sharper decline between -25 mm/year and -50 mm/year. Extreme decreases, ranging from -50 mm/year to -70 mm/year, were rare, affecting only 0.08% of the continent.

In contrast, the increase in rainfall was more limited, covering only 23.4% of Africa. The majority of these regions (23.3%) experienced a moderate increase of 0 to +25 mm/year, while a marginal 0.12% observed a more pronounced increase of +25 mm/year to +40 mm/year. Meanwhile, 39.1% of the continent showed no significant trend. The spatial distribution of these trends largely aligns with the Mann-Kendall results, except in the northeastern Sahara, where Sen's Slope detected no significant trend.

The Buishand Test (Figure 14.f) revealed that up to 85.49% did not have a break point during the study period, either related to no trend or the precipitation increase or decrease that started before the study period. Only 0.04% of the continent area observed a change in trend between 2003 and 2008, comprehending a small tip in the central Sahara. 4.6% observed its change between 2008 and 2013, comprehending parts I west and northern east Sahara, and a small tip in coastal east Africa in Tanzania. 7.7% observed its change between 2013 and 2018, comprehending some parts distributed along west southern Africa, Madagascar, central, east, west and northern Africa. 2.2% of the continent observed a change in precipitation between 2018 and 2023, comprehending areas in northwest-southern Africa and the Sahara region.

c. Annual Mean TCO

Mann Kendall results for Annual Mean TCO (Figure 14.g) show a distinct pattern. A positive trend just below the equator and above was observed, encompassing 18.14% of the total African area. The rest of the continent, including Southern Africa, the equatorial region, and Northern Africa, showed no significant trend, corresponding to up to 81.8% of the continent.

However, Sen's slope results (Figure 14.h) showed a slightly different trend, where the areas along the equator showed the most significant increase rate decreasing in the northward and southward direction, with the Sahara Desert with almost no significant trend. A small decrease was observed along a small strip in northern Africa, accounting for 0.7%, with a decrease rate of about 0 to -0.3 DU/year. 37.55% of the continent's total area observed no significant trend, comprehending the Sahara Desert and a small strip in the south tip. 59.54% of the continent observed an increase of 0 to +0.3DU/year, corresponding to areas right above the equator region and below the Sahel, some small tips in the Western Sahara, and areas below the equator. An increase of +0.3 to +0.6DU/year was observed along the equator, southern Madagascar, and Mozambique.

No break year was found in the dataset, indicating that the trends began prior to our analysis period, or that there was no significant change in the trend within the dataset (Figure 14.i).

d. Annual Mean NDVI

Trend analysis for the NDVI (Figure 14.j, k and l) showed a diverse pattern, with trends distributed sporadically across the continent. A positive Mann-Kendall trend (Figure 14.j), accounting for 20.2% of the area, was observed in Central Africa, dominating the Sahara and Western Africa, with a few occurrences in Eastern and Southern Africa. Areas with a negative trend, accounting for 15.8%, were prevalent in Northern Africa, Western Africa, coastal regions in Southern Africa, Madagascar, and small portions in Eastern Africa. Areas with no detected trend were noted throughout the continent, primarily in Southern Africa, accounting for 64% of the total area.

Sen's Slope analysis (Figure 14.k) highlights the most significant changes in vegetation loss, which surpasses recovery both in terms of affected area and NDVI values. Areas with a negative trend (0 to -0.055 NDVI/year) cover 36.3% of the continent, indicating a widespread

decline in vegetation. In contrast, areas with a positive trend (0 to +0.013 NDVI/year) account for only 28.7% of the total area, showing a more limited vegetation recovery. Meanwhile, 35.0% of the continent showed no significant trend. Despite slight differences in the proportion of areas experiencing positive, negative, or no trends, the spatial distribution of these patterns largely aligns with the results of the Mann-Kendall test.

The most significant changes in land cover detected by the Buishand Test occurred between 2008 and 2018, affecting large portions of the continent (Figure 14.1). During 2013-2018, 26.9% of Africa experienced change, particularly in central Africa, southwestern Africa, western and northern Africa, as well as scattered areas in eastern Africa and Madagascar. The 2008-2013 period also saw a substantial shift, with 13.7% of the continent affected, mainly south of the Sahara Desert. More recent changes between 2018 and 2023 were observed in 8.6% of the continent, concentrated in northern Africa, the Sahara, and scattered areas across West Africa, Central Africa, East Africa, and Madagascar. Earlier in the study period, between 2003 and 2008, only 1.5% of the continent exhibited change, mainly in northern Africa, particularly the northern Sahara Desert. Meanwhile, 49.4% of the continent showed no significant change throughout the study period, with these stable areas scattered across Africa.

5.1.5. Multivariate Linear Regression

a. Correlation coefficients

Table 3 presents the correlation coefficients, including their significance values, for Temperature, Precipitation, TCO, and NDVI in relation to the predictor variables. All correlations were statistically significant at the 99% confidence level ($p = 0.01$). Variable combinations with R-squared values close to or above 10% (0.1) indicated a significant relationship. For temperature, the variables that had the highest r coefficient are the Mean Sea Level Pressure with $r = -0.79467$, explaining 63% of the temperature variability, the AOD_550 and AOD_865 with $r=0.58897$ and $r=0.61847$, explaining 35% and 38% of temperature variability respectively Water vapor with $r = 0.39823$ explaining 16% of temperature variability, and NDVI with $r = -0.3212$ explaining 10% of temperature variability. For Precipitation, the variables that explained most of its variability were Water vapor with $r=0.69759$ explaining 49% of precipitation variability, U wind component with $r=0.34182$ explaining 12% of precipitation variability, NDVI with $r=0.30047$ explaining up to 9% of precipitation variability, and TCO (O3) with $r=-0.3107$ explaining up to 9.7% of precipitation variability. For TCO (O3), the variables that influence the most are Temperature, with $r=-$

0.4657 explaining 21.7% of ozone variability in the atmosphere, Latitude with $r=0.40518$ explaining 16% of ozone variability, Mean Sea Level Pressure with $r=0.39047$ explaining 15% of ozone variability, Water Vapor with $r=-0.4894$, explaining 24% of ozone variability, and Precipitation with $r=-0.3107$ explaining 9.7% of ozone variability. For NDVI, the variables that correlate most of its variability are Latitude with $r=-0.5294$ explaining 28% of its variability, Water Vapor with $r=0.52972$ explaining 28% of NDVI variability, Methane (CH₄) with $r=0.49507$ explaining 24.5% of NDVI variability, AOD₈₆₅ with $r=-0.5038$ explaining 25.3% of NDVI variability, V component of wind with $r=0.45624$ explaining 20.8% of NDVI variability, AOD₅₅₀ with $r=-0.3205$ explaining 10.2% of NDVI variability, Temperature with $r=-0.3212$ explaining 10.3% of its variability, and Precipitation with $r=0.30047$ explaining 9% of NDVI variability.

Table 4. Correlation coefficients for the variables analyzed to Temperature, Precipitation, TCO (O₃), and NDVI

		Temperature (°C)	Precipitation (mm/year)	O3 (DU)	NDVI
Year	r	0.10049	-0.0049	0.09303	-0.021
	r ²	0.010098	2.38E-05	0.008654	0.00044
	p	< 0.001	0.03008	< 0.001	< 0.001
Latitude	r	0.34605	-0.2235	0.40518	-0.5294
	r ²	0.119747	0.049957	0.164169	0.280264
	p	< 0.001	< 0.001	< 0.001	< 0.001
Longitude	r	0.13342	0.09557	-0.1375	-0.1751
	r ²	0.017801	0.009133	0.018895	0.030667
	p	< 0.001	< 0.001	< 0.001	< 0.001
Temperature (°C)	r	--	0.12228	-0.4657	-0.3212
	r ²	--	0.014952	0.216839	0.10315
	p	--	< 0.001	< 0.001	< 0.001
Precipitation (mm/year)	r	0.12228	--	-0.3107	0.30047
	r ²	0.014952	--	0.096503	0.09028
	p	< 0.001	--	< 0.001	< 0.001
Mean Sea Level Pressure (Pa)	r	-0.7947	-0.1881	0.39047	0.35641
	r ²	0.6315	0.035367	0.152465	0.127028
	p	< 0.001	< 0.001	< 0.001	< 0.001
Water Vapor (ppm)	r	0.39823	0.69759	-0.4894	0.52972

	r^2	0.15859	0.486628	0.239522	0.280608
	p	< 0.001	< 0.001	< 0.001	< 0.001
CO2 (ppm)	r	0.13538	-0.0114	0.11483	-0.0487
	r^2	0.018329	0.00013	0.013186	0.002368
	p	< 0.001	< 0.001	< 0.001	< 0.001
CH4 (ppm)	r	0.14784	-0.1174	0.22308	0.49507
	r^2	0.021857	0.01378	0.049766	0.245092
	p	< 0.001	< 0.001	< 0.001	< 0.001
O3 (DU)	r	-0.4657	-0.3107	--	-0.0601
	r^2	0.216839	0.096503	--	0.003614
	p	< 0.001	< 0.001	--	< 0.001
AOD_550	r	0.58897	0.18779	-0.119	-0.3205
	r^2	0.346887	0.035265	0.014163	0.102733
	p	< 0.001	< 0.001	< 0.001	< 0.001
AOD_865	r	0.61847	-0.0653	-0.0146	-0.5038
	r^2	0.382504	0.004258	0.000213	0.253855
	p	< 0.001	< 0.001	< 0.001	< 0.001
NDVI	r	-0.3212	0.30047	-0.0601	--
	r^2	0.10315	0.09028	0.003614	--
	p	< 0.001	< 0.001	< 0.001	--
U wind (m/s)	r	0.07132	0.34182	0.2235	-0.2419
	r^2	0.005087	0.116843	0.049954	0.05853
	p	< 0.001	< 0.001	< 0.001	< 0.001
V wind (m/s)	r	-0.0711	0.0731	-0.3304	0.45624
	r^2	0.005054	0.005344	0.109184	0.20815
	p	< 0.001	< 0.001	< 0.001	< 0.001

b. Multivariate Linear Regression Coefficients for Temperature, Precipitation, TCO, and NDVI models

Table 4 presents regression coefficients for the Temperature, Precipitation, Ozone, and NDVI multivariate linear regression. The MLR model was improved using the Variance inflation factor (VIF), where variables with VIF greater than 10 were removed from the regression models to reduce multicollinearity and improve model performance. Two variables were excluded, the Year and the AOD_865. The other variables that present VIF greater than 5 were kept, considering their conceptual impact on the target variables. Following the coefficients, it is possible to determine the variables that had more influence on the predictions than others. For the Temperature model, the variable CH₄ had the most pronounced coefficient (16.81473), followed by NDVI with a negative coefficient (-3.73089), O₃ with -1.0481, and AOD_550 with -1.0481.

For the Precipitation model, the variable CH₄ had the most significant coefficient (-2574.83), showing a strong negative effect, followed by AOD_550 with 569.4127 showing also a strong positive effect, The U and V components of wind with a positive (41.23397) and a negative (-58.2003) effect respectively, NDVI with a negative effect (-35.5086), O₃ with a positive effect (9.126707), and Latitude (-6.78284) showing precipitation decrease with increasing latitudes. For the O₃ model, the variable CH₄ had the most significant coefficient (72.1372), showing the most potent positive effect in ozone distribution, followed by AOD_550 with -13.6589, showing a strong negative effect, NDVI with a negative effect (-4.10509), and Temperature with a negative effect (-1.88971). For the NDVI model, the variable CH₄ had the highest coefficient (1.70), showing the most potent positive effect in NDVI distribution, followed by AOD_550 with a negative effect (-0.31187). The r-squared coefficients show the significance of the models where the temperature model could explain 87% of the temperature variability, the precipitation model could explain 77% of precipitation variability, Ozone model could explain 81% of ozone variability, and NDVI model could explain 74% of the NDVI data variability (refer to figure 15 for comparison).

Table 5. Multivariate Linear Regression Coefficients for Temperature, Precipitation, TCO, and NDVI Models

Variable	Temperature		Precipitation		Ozone		NDVI	
	Estimate	VIF	Estimate	VIF	Estimate	VIF	Estimate	VIF
(Intercept)	607.5751	--	-21329.8	--	-347.319	--	16.33295	--
Latitude	0.011905	5.022904	-6.78284	4.778043	0.398938	2.971553	-0.0013	5.033027
Longitude	0.005735	1.552221	1.190384	1.551228	0.03901	1.538392	0.000526	1.556639
Temperature (°C)	--	--	-8.8193	7.213418	-1.88971	5.780226	-0.06403	5.501286
Precipitation (mm/year)	-0.00023	4.111068	--	--	0.00421	3.961077	-1.58E-05	4.117051
Mean Sea Level Pressure (Pa)	-0.00579	5.786887	0.218996	7.738438	0.005518	7.710235	-0.00016	7.723033
Water Vapor (ppm)	0.000876	7.408644	0.543565	3.699949	-0.00365	7.42066	0.000216	6.357618
CO2 (ppm)	0.011071	1.04997	0.926904	1.056111	-0.01176	1.056997	-0.00073	1.055579
CH4 (ppm)	16.81473	2.636408	-2574.83	3.074949	72.13728	2.60035	1.702668	3.085241
O3 (DU)	-0.10599	4.235722	9.126707	5.093102	--	--	-0.00395	5.210697
AOD_550	-1.0481	3.188221	569.4127	3.132784	-13.6589	3.117002	-0.31187	3.153478
NDVI	-3.73089	2.962821	-35.5086	3.890576	-4.10509	3.829609	--	--
U wind (m/s)	-0.21917	2.018209	41.23397	2.027088	1.107136	1.972704	-0.03012	2.00764
V wind (m/s)	-0.31017	2.044269	-58.2003	2.069422	0.177634	2.321525	-0.01025	2.308749
mae train	1.042766		203.9935		4.604361		0.122027	
mae test	1.113695		195.5279		5.699429		0.136627	
r	0.921958		0.874347		0.894149		0.856385	
r2	0.850007		0.764483		0.799502		0.733395	

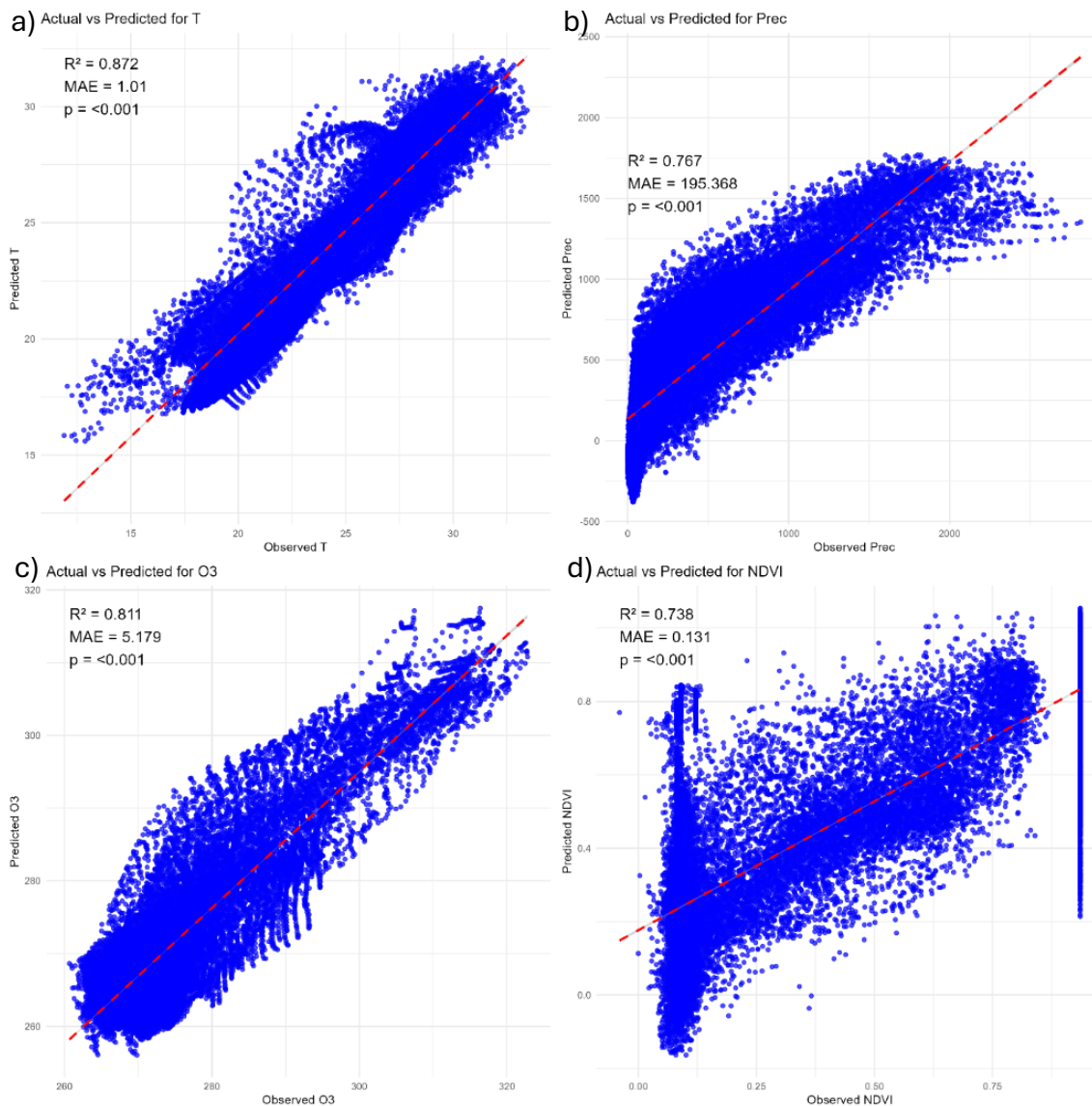


Figure 15. Performance results for Temperature, Precipitation, O₃ and NDVI MLR modes.

5.1.6. Principal Component Analysis (PCA)

The analysis of the principal components (PCs) reveals critical insights into the underlying factors driving variance in the dataset (Table 6). Only the Principal components that had the standard deviation greater than 1 were considered as representative for the data variability, and only the component loadings that were greater than 0.2 (moderate to high influence) were considered as of influence in the variability of the dataset. The first principal component (PC1), which accounts for 27.58% of the total variance, is primarily influenced by AOD_865 (0.4410), AOD_550 (0.4289), Latitude (0.3629), and Temperature (0.3582), highlighting the significant

roles of air quality and temperature in shaping the data's variability. PC2, which explains 19.81% of the variance, is associated with O₃ (0.4200), Water Vapor (-0.5290), and NDVI (-0.3202), indicating an intricate relationship between atmospheric composition and vegetation. PC3, explaining 14.22% of the variance, underscores the strong correlation between greenhouse gases—particularly CO₂ (0.6157) and CH₄ (0.3686)—and precipitation patterns (0.2695), suggesting that changes in these gases may influence rainfall. PC4, which accounts for 10.96% of the variance, reveals the role of CO₂ (0.3158) and precipitation (0.2695), along with U Wind (0.2487), in atmospheric circulation effects, pointing to the complexities of weather systems. PC5 further illustrates this connection by emphasizing the relationship between precipitation (0.5018) and U Wind (0.5580), capturing 9.74% of the variance, reflecting how climate and wind patterns interact. The cumulative analysis shows that the first five PCs account for 82.31% of the total variance, underscoring that most of the dataset's variability can be effectively captured through these components. This suggests a complex interplay of factors, such as climate, wind patterns, and atmospheric dynamics, paving the way for a deeper understanding of climate variability.

Table 6. Loading of Principal Components for the Variables Examined in This Study

	PC1	PC2	PC3	PC4	PC5
Year	0.011403	0.003962	0.61089	0.332014	-0.07092
Latitude	0.362867	0.241002	0.070101	-0.16943	0.065441
Longitude	0.081923	-0.0177	-0.18829	0.509601	-0.12208
Temperature (°C)	0.358193	-0.26094	0.075258	-0.05453	-0.26172
Precipitation (mm/year)	0.049316	-0.34002	-0.09237	0.269485	0.501763
Mean Sea Level Pressure (Pa)	-0.40919	0.213128	0.06377	-0.05703	0.145743
Water Vapor (ppm)	0.044752	-0.52997	0.056439	-0.0302	0.232276
CO2 (ppm)	0.04013	0.011507	0.615668	0.315798	-0.06407
CH4 (ppm)	-0.07849	-0.12884	0.368565	-0.47075	0.139761
O3 (DU)	-0.05299	0.420001	0.167454	-0.1317	0.369664
AOD_550	0.428978	-0.10707	0.040264	-0.17045	0.104538
AOD_865	0.441023	0.02974	0.066142	-0.23486	-0.01555
NDVI	-0.29147	-0.32024	0.105718	-0.18142	0.225001
U wind (m/s)	0.221847	0.090154	-0.06794	0.248721	0.557956
V wind (m/s)	-0.19504	-0.33975	0.016783	-0.06279	-0.21663
Standard Deviation	2.033832	1.723774	1.460656	1.282501	1.208407
Variance	0.275765	0.198093	0.142234	0.109654	0.09735
Cumulative Variance	0.275765	0.473858	0.616092	0.725746	0.823096

5.1.7. Generalized Addictive Model

a) Temperature

The GAM results for temperature are presented in Table 7. The Thin Plate Regression Splines (TPRS) was the smoothing function necessary to capture flexible nonlinear relations amongst the variables. Results show that the most influential parameter is the Latitude with F-statistic equal to 7039.401 and Effective Degrees of Freedom (edf) equal to 8.997106. The following were the variables V component of wind with F= 6569.845 and edf=8.983374, and U component of wind with F=2417.63 and edf=8.961551, suggesting a strong influence of meridional and zonal winds in temperature distribution. The variables CH4 with F=2832.362 and edf=8.990154, and Water vapor with F=2249.652 and edf=8.986959, show a significant influence of GHGs in moderating temperatures. The variables AOD_550 and AOD_865 with F=2103.404 and F=2086 and edf=8.941358 and edf=8.876521, respectively, suggest a moderate influence of atmospheric aerosols in temperature distribution. With moderate influence, Longitude (F=2639.798, edf=8.981346), NDVI (F=2171.807, edf=8.960398), and Mean Sea Level Pressure (F=15088, edf=8.929409). Moreover, with the lowest impact in temperature variability are Precipitation (F=803.6923, edf=8.929409), Year (F=620.1735, edf=8.97574), CO2 (F=573.7875, edf=8.972241), and O3 (F=267.9078, edf=8.919713). The model performance was satisfactory with $r = 0.9673$, explaining 93.6% of the Temperature variability (see Figure 16.a for Temperature GAM model results). The mean absolute error was MAE=0.54 in the training dataset and MAE=0.70 in the test dataset, suggesting difficulties in the model generalization.

Table 7. Summary of the GAM Model for Temperature. The smoothing function used was Thin Plate Regression Splines (TPRS).

Variable	Estimate	edf	Ref.df	F	p-value
(Intercept)	24.2155515	--	--	--	
s(Year)	--	8.97574	8.999688	620.1735	<0.001
s(Latitude)	--	8.997106	8.999979	7039.401	<0.001
s(Longitude)	--	8.981346	8.999872	2639.798	<0.001
s(Precipitation (mm/year))	--	8.955855	8.999443	803.6923	<0.001
s(Mean Sea Level Pressure (Pa))	--	8.929409	8.998608	15088	<0.001
s(Water Vapor (ppm))	--	8.986959	8.999947	2249.652	<0.001
s(CO2 (ppm))	--	8.972241	8.999804	573.7875	<0.001
s(CH4 (ppm))	--	8.990154	8.999971	2832.362	<0.001
s(O3 (DU))	--	8.919713	8.998224	267.9078	<0.001
s(AOD_550)	--	8.941358	8.998235	2103.404	<0.001
s(AOD_865)	--	8.876521	8.994446	2086	<0.001
s(NDVI)	--	8.960398	8.999516	2171.807	<0.001
s(U wind (m/s))	--	8.961551	8.999573	2417.63	<0.001
s(V wind (m/s))	--	8.983374	8.999916	6569.845	<0.001
mae-train	0.54019174				
mae-test	0.70301689				
r	0.96732178				
r2	0.93571142				

b) Precipitation

Table 8 presents the results for the Precipitation GAM model. The same smoothing function (TPRS) was used. Water Vapor with $F=12144.19$ and $edf=8.984541$ showed the highest influence in precipitation moderation. Moderate influence was shown by the variables NDVI ($F=2536.625$, $edf=8.973746$), Latitude ($F=2022.555$, $edf=8.994693$), CH4 ($F=1969.757$, $edf=8.900337$), and V component of wind ($F=1706.47$, $edf=8.982568$). The remaining variables observed low significance in precipitation variability with $F \leq 976.1171$ and $edf \leq 8.985896$. This model can explain 67% of the Precipitation variability, with $r=0.8193982$ (Figure 16.b).

Table 8. Summary of the GAM Model for Precipitation. The smoothing function used was Thin Plate Regression Splines (TPRS).

Variable	Estimate	edf	Ref.df	F	p-value
(Intercept)	555.453981	--	--	--	--
s(Year)	--	8.950623	8.998539	100.4327	<0.001
s(Latitude)	--	8.994693	8.999935	2022.555	<0.001
s(Longitude)	--	8.968788	8.999666	525.149	<0.001
s(Mean Sea Level Pressure (Pa))	--	8.938157	8.998934	407.3058	<0.001
s(Water Vapor (ppm))	--	8.984541	8.999928	12144.19	<0.001
s(CO2 (ppm))	--	8.864237	8.99592	97.36356	<0.001
s(CH4 (ppm))	--	8.900337	8.997227	1969.757	<0.001
s(O3 (DU))	--	8.933745	8.998777	457.9474	<0.001
s(AOD_550)	--	8.989667	8.999951	880.7602	<0.001
s(AOD_865)	--	8.985896	8.999913	976.1171	<0.001
s(NDVI)	--	8.973746	8.999786	2536.625	<0.001
s(U wind (m/s))	--	8.963105	8.99961	312.3895	<0.001
s(V wind (m/s))	--	8.982568	8.99991	1706.47	<0.001
s(Temperature (°C))	--	8.980007	8.999885	689.0379	<0.001
mae-train	132.744374				
mae-test	508.853387				
r	0.8193982				
r2	0.67141341				

c) Ozone

Table 9 presents results for the Ozone GAM model, developed using the same TRPS smoothing function. The variable with the most significant impact on Ozone variation is Year with $F=3032.983$ and $edf=8.995659$. Latitude ($F = 15641.14$, $EDF = 8.993718$) and CO2 ($F = 3032.98$, $EDF = 8.997141$) significantly influence latitudinal variations and GHGs on ozone variations, respectively. Mean Sea Level Pressure ($F=463.0201$, $edf=8.898084$), Water Vapor ($F=852.0008$, $edf=8.939712$), and CH4 ($F=445.4674$, $edf=8.832875$), observed a moderate significance on ozone variability compared to other variables. The remaining variables were observed to have lower significance levels than the rest of the predictors for Ozone variation. The model explained 85.49% of the total ozone variability with $r=0.924633$ (Figure 16.c). MAE for the training dataset was 2.43, and for the test, it was 4.98.

Table 9. Summary of the GAM Model for Ozone. The smoothing function used was Thin Plate Regression Splines (TPRS).

Variable	Estimate	edf	Ref.df	F	p-value
(Intercept)	272.7247	--	--	--	--
s(Year)	--	8.995659	8.999952	3032.983	<0.001
s(Latitude)	--	8.993718	8.999931	15641.14	<0.001
s(Longitude)	--	8.811572	8.990346	222.0457	<0.001
s(Precipitation (mm/year))	--	8.726259	8.979507	109.9132	<0.001
s(Mean Sea Level Pressure (Pa))	--	8.898084	8.997067	463.0201	<0.001
s(Water Vapor (ppm))	--	8.939712	8.998893	852.0008	<0.001
s(CO2 (ppm))	--	8.997141	8.999996	2504.297	<0.001
s(CH4 (ppm))	--	8.832875	8.992206	445.4674	<0.001
s(AOD_550)	--	8.870053	8.994415	376.1891	<0.001
s(AOD_865)	--	8.930936	8.997265	387.894	<0.001
s(NDVI)	--	7.828317	8.646357	51.87354	<0.001
s(U wind (m/s))	--	8.913479	8.997818	161.5243	<0.001
s(V wind (m/s))	--	8.911132	8.997766	156.3947	<0.001
s(Temperature (°C))	--	8.846781	8.993645	65.43158	<0.001
mae-train	2.432554				
mae-test	4.98307				
r	0.924633				
r2	0.854946				

d) NDVI

Table 10 presents the result for the NDVI GAM model, which was developed using TPRS. Overall, the model observed MAE=0.099 for the training set and MAE=0.899, suggesting that the model performs well in the training set but generalizes poorly in the test set, with $r=0.4726$ explaining only 22.33% of the ozone variance (Figure 16.d). However, the p values were <0.001 for all the predictors, confirming the statistical significance of the results. The variable Temperature had the most decisive influence on NDVI based on the edf value (edf=8.967755, $F=2633.044$). CH₄ (EDF = 8.950255, $F = 3279.29$) also had a strong impact, which suggests climate direct feedback on vegetation. Based on F-statistic values, the highest predictors are CH₄ ($F = 3279.29$), Temperature ($F = 2633.04$), Latitude ($F = 1266.11$), Water Vapor ($F = 880.90$), and Year ($F = 361.82$).

Table 10. Summary of the GAM Model for NDVI. The smoothing function used was Thin Plate Regression Splines (TPRS).

Variable	Estimate	edf	Ref.df	F	p-value
(Intercept)	0.604441	--	--	--	--
s(Year)	--	8.995004	8.999948	361.8264	<0.001
s(Latitude)	--	8.996836	8.999985	1266.112	<0.001
s(Longitude)	--	8.971204	8.999748	751.3153	<0.001
s(Precipitation (mm/year))	--	8.737355	8.981289	286.2026	<0.001
s(Mean Sea Level Pressure)	--	8.908437	8.99768	916.5303	<0.001
s(Water Vapor (ppm))	--	8.935027	8.998833	880.9044	<0.001
s(CO2 (ppm))	--	8.871682	8.996617	360.8614	<0.001
s(CH4 (ppm))	--	8.950255	8.999292	3279.288	<0.001
s(O3 (DU))	--	8.974457	8.99981	467.0708	<0.001
s(AOD_550)	--	8.93547	8.99868	132.6359	<0.001
s(AOD_865)	--	8.973633	8.999554	103.9248	<0.001
s(U wind (m/s))	--	8.987083	8.999946	823.6724	<0.001
s(V wind (m/s))	--	8.93832	8.998945	155.6199	<0.001
s(Temperature (°C))	--	8.967755	8.999704	2633.044	<0.001
mae-train	0.099006				
mae-test	0.89984				
r	0.472579				
r2	0.223331				

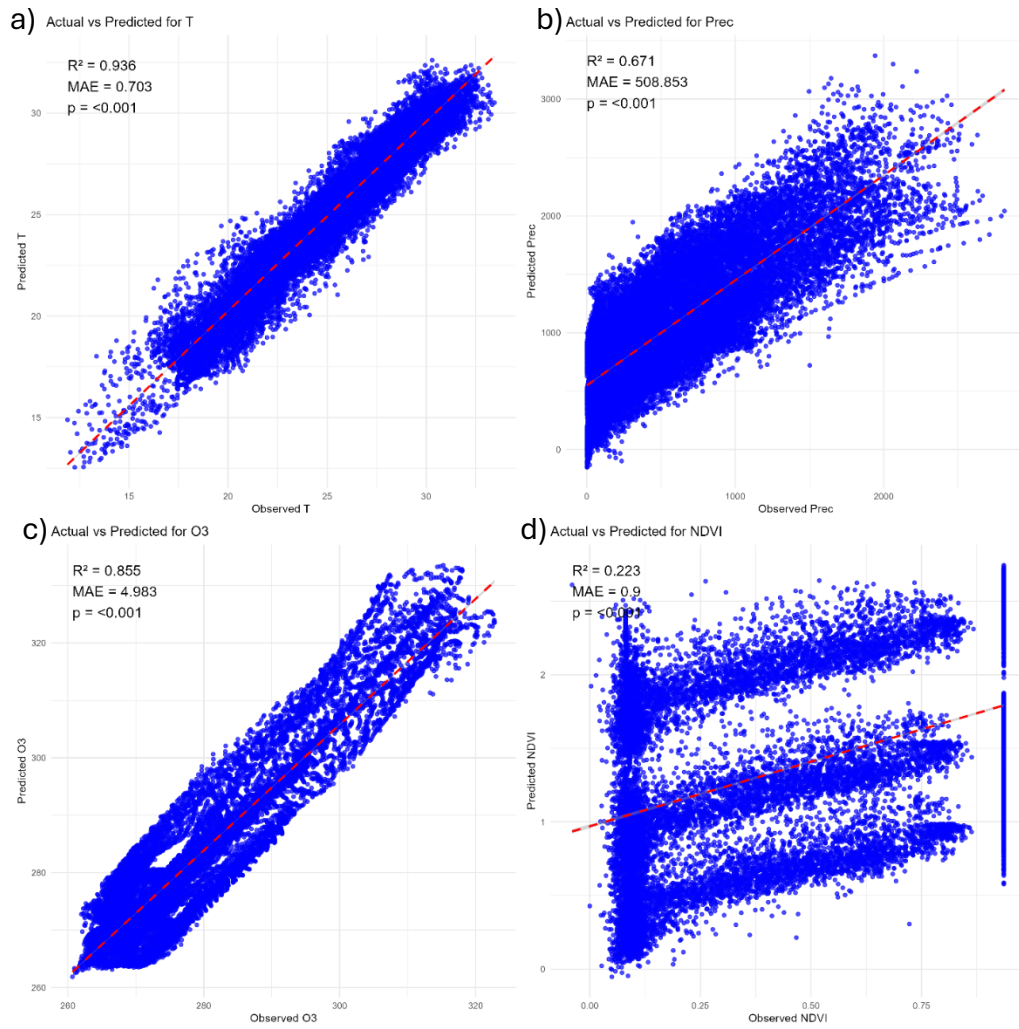


Figure 16. Performance Results for Temperature, Precipitation, O3, and NDVI GAM models.

5.2. Summary and Discussion

5.2.1. Description of the dataset

The general data described across the Northern, Central, and Southern regions, using a comprehensive dataset of climate variables to characterize environmental conditions, revealed slight differences in temperature, precipitation, atmospheric composition, aerosol properties, vegetation indexes, and wind components across these regions, revealing some heterogeneity in climate dynamics in Africa.

The temperature analysis revealed a consistent median temperature of approximately 25 °C across all three regions. Nonetheless, outliers in the lower whisker suggest cooler annual temperatures (10 °C to 15 °C) in the northern and southern regions and localized cooling events or variations in altitude.

These results are consistent with established climate models for regional temperature forecasting, which account for variations in factors such as latitude, elevation, and proximity to water bodies (IPCC, 2021). The precipitation's highly skewed distribution, with a long upper whisker predominance and many outliers above 2100 mm/year, suggests a significant variability in rainfall patterns. Accentuated in the northern region suggests higher frequencies of extreme rainfall and drought events. The low median values (~400 mm/year) and first quartile (~1mm/year) indicate that most regions are arid, which is consistent with previous studies characterizing Africa's climate (e.g., (S. E. Nicholson, 2001a). These results show the importance of considering extreme events when studying climate patterns.

The consistency of mean sea level pressure in the three regions close to standard (~101,350 Pa) suggests a relatively stable atmosphere at the macroscale. Water vapor concentrations with a large spread suggest significant regional variability in humidity. High values of water vapor indicate the presence of localized areas with high humidity, potentially correlated with evapotranspiration from vegetated areas or proximity to water sources. The consistently stable CO₂ (~393ppm) and CH₄ (~1.79ppm) concentrations across all the regions are consistent with global atmospheric mixing and long-term series of these GHGs (IPCC, 2021) The Total Column Ozone (O₃) concentrations showed subtle regional differences, with the northern region exhibiting slightly higher variability and more extreme values. These patterns can be attributed to differences in the regional dynamics of stratospheric ozone, which are influenced by factors such as atmospheric circulation patterns, seasonal variations, and atmospheric composition (Brasseur & Solomon, 2005).

The right-skewed distribution in both AOD_550 and AOD_865, coupled with numerous outliers, suggests the prevalence of aerosol pollution across the continent. The increased number of AOD_550 in the central region and the reduction in AOD_865 outliers indicate a shift in aerosol composition and size distribution. According to Dubovik et al. (2002), these observed patterns can be associated with different aerosol sources, such as industrial emissions, dust storms, or biomass burning, which have distinct characteristics in terms of particle size and optical properties. High AOD values are typically associated with significant air pollution, which has detrimental effects on human health and the regional climate (Charlson et al., 1982). The NDVI values, ranging from 0.20 to 0.82, suggest a general mixture of moderate to dense vegetation cover. The slightly higher first quartile of NDVI in the Central and Southern regions compared to the Northern region suggests potentially denser vegetation in these regions. Our NDVI results are consistent with the expected variations associated with varying aridity and agricultural activity (Tucker, 1979).

The U and V wind components exhibited a predominantly symmetrical distribution centered around 0, indicating low wind speeds. The mainly negative V component implies a dominant southerly direction. The presence of both positive and negative outliers in the U and V components suggests the occurrence of regional or sporadic extreme bursts. A slight reduction in the U component and an increase in the V component in the Central region indicate a subtle shift in wind direction, possibly due to regional topography or pressure gradients.

5.2.2. Spatial Variability

Spatial variability maps for all the variables across Africa from 2003 to 2023 were analyzed, revealing distinct regional patterns and gradients that highlight the continent's complex climate dynamics. Generally, the variables analyzed showed a highly interconnected pattern.

The spatial distribution of mean annual temperature is consistent with established research in the African climate. The high temperatures observed in the Sahara and Sahel regions are consistent with their geographical location in arid areas (NICHOLSON, 2019). Likewise, the cooler regions in southern Africa, especially in regions like Lesotho, reflect the influence of altitude in temperature decrease (Kruger & Shongwe, 2004). The central region's present temperatures are typical of those found at the equator and are influenced by both equatorial and subtropical climate regimes.

Precipitation patterns reveal an enhanced contrast between arid and humid zones. The extremely low precipitation in parts of southern Africa, the Horn of Africa, and the whole Sahara and Sahel region, points towards drought conditions, potentially exacerbating water scarcity challenges (IPCC, 2021). The high values of precipitation along the central region of Congo and coastal West Africa, are characteristic of equatorial rainforest climates influenced mainly by the ITCZ and monsoon systems (Sultan & Janicot, 2003).

The distribution of Mean Sea Level Pressure correlates with the observed precipitation pattern. Low pressure in the Congo and Sahel regions is associated with rising air and increasing rainfall, while high pressure over the Sahara and southern Africa suggests descending air and dry conditions. This dynamic relationship between mean sea level pressure and precipitation constitutes a fundamental aspect of atmospheric circulation (Trenberth et al., 2000).

The spatial variability of water vapor is highly correlated with precipitation patterns, where high values are found in humid regions and low values in arid regions. This strong positive correlation underscores the importance of water vapor as a key component in the hydrological cycle and its role in regulating regional climate (Held & Soden, 2006).

The observed CO₂ spatial variability, which increases northward, reflects both anthropogenic emissions and vegetation distribution. The contrast between the low CO₂ concentrations in the southern Africa and increasing CO₂ concentrations northwards may suggest the impact of industrial activities and deforestation in the northern hemisphere, as well as atmospheric circulation patterns transporting CO₂ from other regions (IPCC, 2021). The localized variability in CH₄ concentrations suggests the influence of specific sources, such as wetlands, livestock, and agricultural activities (Saunois et al., 2020). Further research is required to establish the specific sources responsible for these methane hotspots.

Ozone distribution, observing low values in central Africa along the equator and increasing towards the poles, is consistent with the global ozone distribution observed in another research (Brasseur & Solomon, 2005), with distribution patterns influenced by atmospheric circulation and photochemical processes. The slightly lower ozone levels at the southern tip compared to the northern tip may be linked to the proximity of the Antarctic ozone hole and the effects of polar vortex dynamics.

The spatial variability of AOD₅₅₀ and AOD₈₆₅ reveals significant differences in aerosol loading. The high AOD values in the Western Sahara and West Africa are most probably connected to dust emissions from the Sahara Desert and biomass burning activities (Prospero et al., 2002) possibly influenced by atmospheric circulation patterns. The lower AOD values in southern and eastern Africa suggest relatively low pollution. However, localized sources of aerosol, such as industrial emissions and agricultural activities, may contribute to regional air pollution. The difference in AOD₅₅₀ and AOD₈₆₅ values reflect the distribution of aerosols, with higher values at shorter wavelengths suggesting the abundance of smaller particles.

The NDVI distribution highlights the high variability of vegetation across Africa. The high NDVI values in central and southeastern Africa indicate dense vegetation cover, and low values in the Sahara, Sahel, and parts of southern Africa reflect sparse vegetation cover due to water scarcity and desertification (Tucker, 1979). The localized high NDVI values in the Sahel region might suggest areas of irrigated agriculture or localized rainfall events.

The analysis of wind patterns reveals complex mechanisms of atmospheric circulation systems that drive regional climate. The prevailing northward and eastward winds, along with the observed centers of divergence, agree with the influence of the Hadley cell circulation, monsoon systems, and local topographic features (ADRIAN E. GILL, 1982). The strong winds over the Sahara Desert are probably associated with strong pressure gradients and the absence of vegetation cover.

5.2.3. Trend Analysis and Homogeneity for Temperature, Rainfall, TCO, and NDVI

The trend analysis investigated trends in annual mean temperature, annual cumulative precipitation, annual mean total column ozone (O₃), and NDVI across Africa from 2003 to 2023, employing the Mann Kendall test, Sen's Slope estimator, and the Buishand Test. The results revealed a high degree of heterogeneity among the tests, suggesting that complex environmental factors influence the continent.

The analysis of annual mean temperature revealed a dominant warming trend across Africa, consistent with findings from the intergovernmental Panel on Climate Change (IPCC) reports (IPCC, 2021). The Mann-Kendall test showed a significant portion of the continent (59.21%), particularly in Madagascar, central Africa, the border region in southern Africa, and northern Africa, with temperature increases. This is consistent with studies in global warming trends

highlighting accelerated warming in specific regions in Africa (Hulme et al., 2001; Niang et al., 2014). The Sen's Slope quantifies this trend, showing an increasing trend from 0 to +0.20°C/year. A small percentage (<1%) has observed a slight decrease in temperature, probably due to changes in local conditions throughout the years. The Buishand test identified change points showing that the majority of the continent observed a shift between 2013 and 2018, implying an acceleration of warming during and after this period, possibly related to changes in radiative forcing feedback mechanisms. However, areas showing positive trends in the Mann-Kendall test and Sen's Slope estimator may have warmed before the study period; hence, those areas appear as if there is no change point detected.

The annual precipitation revealed a more complex pattern, with both increasing and decreasing trends observed across Africa. The Mann-Kendall test indicated a quasi-even distribution between areas with significant increasing (8.37%) and decreasing (18.23%) trends, and areas with no trend, accounting for 73.40%. This spatial variability in trend agrees with previous studies that highlighted the diverse rainfall patterns across Africa and the influence of ITCZ and monsoon systems, and regional climate oscillations in precipitation variability (Nicholson, 2000a,b). The observed decreases in precipitation in southern Africa, Madagascar, and parts of West Africa and coastal East Africa suggest implications in potential drought risks and impacts on water resources and agriculture. In contrast, increases in precipitation in parts of the central and eastern Sahara, central Africa, and coastal eastern Africa suggest implications for flood risk and ecosystem dynamics. The Sen's Slope analysis provides insight on the magnitude of increase (0 to ~+40mm/year) and decrease (0 to ~-70mm/year), suggesting that the impact on precipitation abundance is less than in scarcity in rainfall. The Buishand test, which shows that the majority of the continent has no change point detected during the study period, suggests that precipitation patterns may be influenced by long-term climate cycles or that the study period was insufficient to capture a significant trend.

The analysis of annual O₃ showed a predominant positive trend over the continent. The Mann-Kendall test showed a positive trend just below and above the equator, encompassing 18.14% of the African area, and the remaining area showed no trend. However, Sen's slope reveals a more pronounced area of increase in O₃ concentration, with a small area in the northern tip of Africa. O₃/TCO increase is significant in most parts of Africa, suggesting a strong impact of the implementation of the Montreal Protocol (Bandoro et al., 2018; Farman et al., 1985; Solomon, 1999). The spatial pattern of ozone increase aligns with the expected ozone recovery

based on atmospheric circulation patterns and the reduction of ozone-depleting substances. The absence of a detected change year suggests that the observed ozone trends in ozone concentrations are part of an ongoing long-term recovery trajectory.

The NDVI analysis showed a diversified pattern in vegetation change across Africa, with both positive and negative trends observed. The Mann-Kendall test showed a positive trend in Central Africa, parts of the Sahara, and Western Africa, suggesting an increase in vegetation possible due to increased precipitation, improved land management practices, and the recovery of degraded ecosystems. In contrast, negative NDVI trends were observed in Northern Africa, Western Africa, and coastal regions in Southern Africa, as well as in Madagascar and parts of Eastern Africa, suggesting a loss of vegetation or degradation, possibly due to deforestation, overgrazing, drought, or land-use change. The Sen's slope analysis validated the spatial variability of NDVI trends, revealing regions with both vegetation loss (as much as -0.055 NDVI/year) and vegetation gain (up to +0.013 NDVI/year). The Buishand test detected change points in NDVI trends, indicating that a significant portion of the continent changed between 2013 and 2018. This implies that a combination of climate variability, land-use changes, and various environmental factors shape vegetation dynamics.

5.2.4. Statistical Modeling: Multivariate Linear Regression; Principal Component Analysis; Genialized Additive Models.

Interactions were analyzed among Climate, Vegetation, and Ozone (herein referred to as target variables) using a set of Statistical Methods, including multivariate linear regression, Principal Component Analysis, and Generalized additive models, revealing complex relationships between these variables and others.

The multivariate linear regression analysis highlighted significant correlations between various climatic and atmospheric variables and the target variables. The Pearson correlation results showed a strong negative correlation between Mean Sea Level Pressure and Temperature, as well as positive correlations between AOD_550, AOD_865, and temperature, revealing the importance of atmospheric dynamics and air quality in modulating regional temperatures. These findings corroborate with existing literature that emphasizes the role of aerosols in absorbing solar radiation and influencing atmospheric states (IPCC, 2021). The negative correlation between NDVI and temperature suggests a potential feedback mechanism where increased vegetation cover can contribute to localized cooling through evapotranspiration. This relationship is well documented in eco-climatological studies (Bonan, 2008).

Pearson correlation results for precipitation revealed a strong correlation with water vapor, consistent with the key fundamental understanding about the hydrological cycle (Trenberth et al., 2003). The negative correlation between O₃ and precipitation suggests a potential link between ozone formation, especially surface ozone, and precipitation patterns; however, further investigations are required to understand the causal relationships. This finding warrants further exploration, as previous studies have suggested that changes in stratospheric ozone can influence tropospheric circulation patterns, potentially impacting regional precipitation (Thompson et al., 2011)

The Pearson correlation for O₃ showed a significant correlation with temperature and water vapor, suggesting that warmer temperatures and increased atmospheric moisture may contribute to ozone depletion, agreeing with previous studies that stated that higher temperatures can accelerate ozone-depleting chemical reactions in the stratosphere (Ravishankara et al., 2009). The positive correlation between O₃ and latitude is likely reflected in the latitudinal gradient in ozone concentration, which is related to variations in solar radiation and atmospheric circulation.

The Pearson correlation results for NDVI revealed significant correlations with latitude, water vapor, CH₄, and AOD at 550 nm and 865 nm. A negative correlation was observed with latitude, suggesting a decrease in vegetation cover with increasing latitude, possibly due to decreasing temperatures. A positive correlation with water vapor suggests that moisture availability plays an enhanced role in vegetation growth. The positive correlation with CH₄ and negative correlation with AODs suggest complex interactions between GHGs, air quality, and vegetation, where CH₄ can serve as a nutrient for some plants, and high aerosols can reduce solar radiation reaching the surface, thereby inhibiting photosynthesis and reducing NDVI (Chappelka & Samuelson, 1998).

The multivariate linear regression coefficients further elucidated the relative importance of different variables in predicting temperature, precipitation, ozone, and NDVI. The Strong negative coefficient for AOD₅₅₀ in the temperature model suggests a cooling effect of fine particles suspended in the atmosphere, probably through light reflection. The significant coefficient of CH₄ in all four models highlights the pervasive influence of the GHG on climate and vegetation. The r-squared values showed a reliable ability of the models to explain a substantial portion of the variability of temperature (87%), Precipitation (77%), O₃ (*1%), and NDVI (74%).

The PCA results provided a valuable synthesis of the complex interactions between the variables, providing the components and the variables that explain most of the variability in the dataset. PC1, dominated by AOD_865, AOD_550, latitude, and temperature, highlights the importance of air quality and temperature in driving overall variability. PC2, associated with O3, Water Vapor, and NDVI, highlights the profound relationships between atmospheric composition and vegetation. The strong influence of GHGs (CO2 and CH4) on precipitation patterns is highlighted in PC3, which is in line with the growing evidence that correlates climate change to rainfall regimes (IPCC, 2021). The first five components account for 82% of the total variance in the dataset, underscoring the significance of these key drivers in shaping the environmental conditions in Africa.

The GAM results offered a more detailed view of the non-linear connections among variables. Latitude, wind components, CH4, and water vapor have a significant impact on temperature, underscoring the roles of large-scale atmospheric circulation and greenhouse gas (GHG) forcing in shaping temperature trends. For precipitation, the GAM emphasized the crucial impact of water vapor and the moderate effects of NDVI, latitude, CH4, and the meridional (V) wind component. Regarding O3 concentrations, the GAM identified the variable Year as the primary predictor, suggesting a long-term trend in ozone likely attributable to the Montreal Protocol (WMO, 2018). Additionally, the moderate impact of CO2 on ozone fluctuations indicates intricate interactions between GHG forcing and stratospheric chemistry. Notably, the training dataset exhibited a lower mean absolute error (MAE) than the test datasets in GAM models, particularly for the NDVI GAM model, indicating potential overfitting and the necessity for further refinement and validation of the models.

These findings highlight the importance of atmospheric dynamics, air quality, greenhouse gas (GHG) emissions, and vegetation feedback in shaping African environmental conditions. The results have significant implications for climate modeling, potentially enhancing predictions of future climate change impacts across the continent. Further research is necessary to investigate the underlying mechanisms behind the observed correlations and to refine models using extended time series data and higher-resolution datasets. Understanding these intricate interactions is crucial for developing effective strategies to combat climate change and promote sustainable development in Africa.

6. Conclusions and Recommendations

This study examined the yearly trends and complex relationships between the ozone layer, vegetation cover, and climate in Africa from 2003 to 2023. We employed a broad range of statistical and modeling techniques to analyze reanalysis data. Our analysis included descriptive statistics, Mann-Kendall trend tests, Sen's slope estimation, Buishand change point detection, multivariate linear regression, principal component analysis (PCA), and generalized additive models (GAMs), offering an in-depth understanding of the spatiotemporal dynamics that influence these vital environmental variables.

The results indicate significant statistical trends in ozone levels, vegetation indices (such as NDVI), and key climatic factors (including temperature and precipitation) across various regions of the continent. Using the Mann-Kendall and Sen's slope methods, we measured both the strength and direction of these trends, pinpointing regions undergoing ozone loss, vegetation decline, and alterations in climate patterns. Additionally, the Buishand test identified potential breakpoints in these time series, indicating moments of sudden change that warrant further investigation into their causes and potential feedback mechanisms, mainly between 2013 and 2018 for Temperature, Precipitation, and NDVI, showing a recent enhancement of CC and its impacts.

Multivariate linear regression and principal component analysis (PCA) clarified the intricate relationships among ozone, vegetation, and climate. Our findings indicate that alterations in ozone levels, especially in the upper atmosphere, noticeably affect surface temperature and solar radiation (inferred), thereby impacting vegetation productivity. GAMs enhanced this insight by capturing non-linear relationships and determining the ideal ranges for climatic variables vital for healthy vegetation growth. The analysis revealed regional differences in these interactions, underscoring the importance of considering local environmental contexts when assessing ecosystem vulnerability to climate change and ozone depletion.

These findings provide substantial information key for environmental policy and resource management across Africa. Recognizing the connections between ozone, vegetation, and climate is crucial for developing effective strategies to mitigate CC, combat desertification, and promote sustainable land use practices across Africa. The identified trends and interactions can inform targeted interventions, such as afforestation initiatives in regions experiencing vegetation loss or the implementation of stricter emission regulations in areas where ozone depletion is prevalent, especially the northern Africa.

Several potential research paths emerge from this study. First, using higher-resolution data and regional climate models could enhance our understanding of the local-scale effects of ozone depletion and climate change on vegetation. The use of Machine Learning Methods are highly encouraged to account to non-linearities. Second, assessing the influence of specific human activities, like farming practices and industrial emissions, on the observed trends would be beneficial. Third, exploring feedback loops between vegetation cover, surface albedo, and regional climate may refine our insight into the Earth system's intricate interactions. Lastly, broadening the analysis to include data before 2003 would provide a longer-term view of the trends and facilitate a more comprehensive evaluation of human impacts on the ozone layer, vegetation, and climate in Africa. This research contributes to the growing body of knowledge that highlights the vulnerability of African ecosystems to global environmental changes, underscoring the urgent need for collaborative efforts toward sustainable development and environmental stewardship.

7. References

- 3CS. (2021). *Precipitation monthly and daily gridded data from 1979 to present derived from satellite measurement*. Copernicus Climate Change Service (C3S) Climate Data Store (CDS). . 10.24381/cds.c14d9324
- Abera, T. A., Heiskanen, J., Pellikka, P., & Maeda, E. E. (2018). Rainfall–vegetation interaction regulates temperature anomalies during extreme dry events in the Horn of Africa. *Global and Planetary Change*, *167*, 35–45. <https://doi.org/10.1016/j.gloplacha.2018.05.002>
- Adler, R., Sapiiano, M., Wang, J.-J., & University of Maryland College Park. (2017). *Climate Data Record (CDR) Program Climate Algorithm Theoretical Basis Document (C-ATBD) Global Precipitation Climatology Project (GPCP) Daily Analysis Precipitation-GPCP Daily CDR*.
- ADRIAN E. GILL. (1982). *Atmosphere—Ocean Dynamics. International Geophysics Series* (Vol. 30).
- Adzawla, W., Sawaneh, M., & Yusuf, A. M. (2019). Greenhouse gasses emission and economic growth nexus of sub-Saharan Africa. *Scientific African*, *3*, 65. <https://doi.org/10.1016/j.sciaf.2019.e0>
- Aghedo, A. M., Schultz, M. G., & Rast, S. (2007). The influence of African air pollution on regional and global tropospheric ozone. In *Atmos. Chem. Phys* (Vol. 7). www.atmos-chem-phys.net/7/1193/2007/
- Akritas, M. G., Murphy, S. A., & LaValley, M. P. (1995). The Theil-Sen estimator with doubly censored data and applications to astronomy. *Journal of the American Statistical Association*, *90*(429), 170–177. <https://doi.org/10.1080/01621459.1995.10476499>
- Arfasa, G. F., Owusu-Sekyere, E., & Doke, D. A. (2023). Past and future land use/land cover, and climate change impacts on environmental sustainability in Veve catchment, Ghana. *Geocarto International*, *38*(1). <https://doi.org/10.1080/10106049.2023.2289458>
- Arowolo, A. V., & Oluleye, A. (2022). Assessing the influence of intertropical discontinuity on total column ozone variation over West Africa. *Environmental Science and Pollution Research*, *29*(44), 66689–66704. <https://doi.org/10.1007/s11356-022-20460-2>
- Asenso Barnieh, B., Jia, L., Menenti, M., Yu, L., Nyantakyi, E. K., Kobo-Bah, A. T., Jiang, M., Zhou, J., Lv, Y., Zeng, Y., & Bennour, A. (2023). Spatiotemporal Patterns in Land Use/Land Cover Observed by Fusion of Multi-Source Fine-Resolution Data in West Africa. *Land*, *12*(5). <https://doi.org/10.3390/land12051032>
- Baarsch, F., Granadillos, J. R., Hare, W., Knaus, M., Krapp, M., Schaeffer, M., & Lotze-Campen, H. (2020). The impact of climate change on incomes and convergence in Africa. *World Development*, *126*. <https://doi.org/10.1016/j.worlddev.2019.104699>
- Ball, W. T., Chiodo, G., Abalos, M., Alsing, J., & Stenke, A. (2020). Inconsistencies between chemistry-climate models and observed lower stratospheric ozone trends since 1998.

Atmospheric Chemistry and Physics, 20(16), 9737–9752. <https://doi.org/10.5194/acp-20-9737-2020>

- Bandoro, J., Solomon, S., Santer, B. D., Kinnison, D. E., & Mills, M. J. (2018). Detectability of the impacts of ozone-depleting substances and greenhouse gases upon stratospheric ozone accounting for nonlinearities in historical forcings. *Atmospheric Chemistry and Physics*, 18(1), 143–166. <https://doi.org/10.5194/acp-18-143-2018>
- Barnet, C. (2019). *Sounder SIPS: AQUA AIRS IR-only Level 3 CLIMCAPS: Comprehensive Quality Control Gridded Monthly V2*. Goddard Earth Sciences Data and Information Services Center (GES DISC). 10.5067/ZPZ430KOPMIX
- Barnieh, B. A., Jia, L., Menenti, M., Zhou, J., & Zeng, Y. (2020). Mapping land use land cover transitions at different spatiotemporal scales in West Africa. *Sustainability (Switzerland)*, 12(20), 1–52. <https://doi.org/10.3390/su12208565>
- Bauer, S. E., Im, U., Mezuman, K., & Gao, C. Y. (2019). Desert Dust, Industrialization, and Agricultural Fires: Health Impacts of Outdoor Air Pollution in Africa. *Journal of Geophysical Research: Atmospheres*, 124(7), 4104–4120. <https://doi.org/10.1029/2018JD029336>
- Bencherif, H., Tohir, A. M., Mbatha, N., Sivakumar, V., Du Preez, D. J., Bègue, N., & Coetzee, G. (2020). Ozone variability and trend estimates from 20-years of ground-based and satellite observations at irene station, South Africa. *Atmosphere*, 11(11). <https://doi.org/10.3390/atmos11111216>
- Bocci, V. (2002). Physico-Chemical Properties of Ozone. In *Oxygen-Ozone Therapy* (pp. 37–39). Springer Netherlands. https://doi.org/10.1007/978-94-015-9952-8_4
- Boiyo, R., Kumar, K. R., Zhao, T., & Bao, Y. (2017). Climatological analysis of aerosol optical properties over East Africa observed from space-borne sensors during 2001–2015. *Atmospheric Environment*, 152, 298–313. <https://doi.org/10.1016/j.atmosenv.2016.12.050>
- Bonan, G. B. (2008). Forests and Climate Change: Forcings, Feedbacks, and the Climate Benefits of Forests. *Science*, 320(5882), 1444–1449. <http://science.sciencemag.org/>
- Bórnez, K., Descals, A., Verger, A., & Peñuelas, J. (2020). Land surface phenology from VEGETATION and PROBA-V data. Assessment over deciduous forests. *International Journal of Applied Earth Observation and Geoinformation*, 84. <https://doi.org/10.1016/j.jag.2019.101974>
- Bozzo, A., Benedetti, A., Flemming, J., Kipling, Z., & Rémy, S. (2020). An aerosol climatology for global models based on the tropospheric aerosol scheme in the Integrated Forecasting System of ECMWF. *Geoscientific Model Development*, 13(3), 1007–1034. <https://doi.org/10.5194/gmd-13-1007-2020>
- Brasseur, G. P., & Solomon, S. (2005). *Aeronomy of the Middle Atmosphere*.

- Brown, F., Folberth, G. A., Sitch, S., Bauer, S., Bauters, M., Boeckx, P., Cheesman, A. W., Deushi, M., Dos Santos Vieira, I., Galy-Lacaux, C., Haywood, J., Keeble, J., Mercado, L. M., O'connor, F. M., Oshima, N., Tsigaridis, K., & Verbeeck, H. (2022). The ozone-climate penalty over South America and Africa by 2100. *Atmospheric Chemistry and Physics*, 22(18), 12331–12352. <https://doi.org/10.5194/acp-22-12331-2022>
- Brown, L. A., Meier, C., Morris, H., Pastor-Guzman, J., Bai, G., Lerebourg, C., Gobron, N., Lanconelli, C., Clerici, M., & Dash, J. (2020). Evaluation of global leaf area index and fraction of absorbed photosynthetically active radiation products over North America using Copernicus Ground Based Observations for Validation data. *Remote Sensing of Environment*, 247. <https://doi.org/10.1016/j.rse.2020.111935>
- Buchhorn, M., Lesiv, M., Tsendbazar, N. E., Herold, M., Bertels, L., & Smets, B. (2020). Copernicus global land cover layers-collection 2. *Remote Sensing*, 12(6). <https://doi.org/10.3390/rs12061044>
- Bullock, E. L., Healey, S. P., Yang, Z., Oduor, P., Gorelick, N., Omondi, S., Ouko, E., & Cohen, W. B. (2021). Three decades of land cover change in East Africa. *Land*, 10(2), 1–15. <https://doi.org/10.3390/land10020150>
- Bunyangha, J., Majaliwa, M. J. G., Muthumbi, A. W., Gichuki, N. N., & Egeru, A. (2021). Past and future land use/land cover changes from multi-temporal Landsat imagery in Mpologoma catchment, eastern Uganda. *Egyptian Journal of Remote Sensing and Space Science*, 24(3), 675–685. <https://doi.org/10.1016/j.ejrs.2021.02.003>
- C. Sullivan. (2016, January 27). *Human-Made Fires Pollute Air with Ozone Half a World Away*. EOS. <https://eos.org/articles/human-made-fires-pollute-air-with-ozone-half-a-world-away>
- CAMS. (2021). *CAMS global greenhouse gas reanalysis (EGG4)*. ECMWF. <https://ads.atmosphere.copernicus.eu/api/catalogue/v1/collections/cams-global-ghg-reanalysis-egg4>
- Cavalieri, O., Cairo, F., Fierli, F., Di Donfrancesco, G., Snels, M., Viterbini, M., Cardillo, F., Chatenet, B., Formenti, P., Marticorena, B., & Rajot, J. L. (2010). Variability of aerosol vertical distribution in the Sahel. *Atmospheric Chemistry and Physics*, 10(24), 12005–12023. <https://doi.org/10.5194/acp-10-12005-2010>
- Chappelka, A. H., & Samuelson, L. J. (1998). Ambient ozone effects on forest trees of the eastern United States: A review. In *New Phytologist* (Vol. 139, Issue 1, pp. 91–108). <https://doi.org/10.1046/j.1469-8137.1998.00166.x>
- Charlson, R. J., Schwartz, S. E., Hales, J. M., Cess, R. D., Coakley, J. A., Jr, Hansen, J. E., & Hofmann, D. J. (1982). Climate Forcing by Anthropogenic Aerosols. *Science*, 255(5043), 423–430.

- Chase, B. M., Boom, A., Carr, A. S., & Reimer, P. J. (2024). Tropical forcing and ENSO dominate Holocene climates in South Africa's southern Cape. *Quaternary Science Reviews*, 330, 108563. <https://doi.org/10.1016/j.quascirev.2024.108563>
- Clain, G., Baray, J. L., Delmas, R., Diab, R., Leclair De Bellevue, J., Keckhut, P., Posny, F., Metzger, J. M., & Cammas, J. P. (2009). Tropospheric ozone climatology at two Southern Hemisphere tropical/subtropical sites, (Reunion Island and Irene, South Africa) from ozonesondes, LIDAR, and in situ aircraft measurements. In *Atmos. Chem. Phys* (Vol. 9). www.atmos-chem-phys.net/9/1723/2009/
- Coldewey-Egbers, M., Loyola, D. G., Lerot, C., & Van Roozendael, M. (2022). Global, regional and seasonal analysis of total ozone trends derived from the 1995-2020 GTO-ECV climate data record. *Atmospheric Chemistry and Physics*, 22(10), 6861–6878. <https://doi.org/10.5194/acp-22-6861-2022>
- Collins, J. M. (2011). Temperature Variability over Africa. *Journal of Climate*, 24(14), 3649–3666. <https://doi.org/10.1175/2011JCLI3753.1>
- Combrink, J., Diab, R. D., Sokolic, F., & Brunet, E. G. (1995). Atmospheric. In *Ekvier Science Ltd* (Vol. 29, Issue 6).
- Conway, D. (2011). Adapting climate research for development in Africa. In *Wiley Interdisciplinary Reviews: Climate Change* (Vol. 2, Issue 3, pp. 428–450). Wiley-Blackwell. <https://doi.org/10.1002/wcc.115>
- Cooper, O. R., Schultz, M. G., Schröder, S., Chang, K. L., Gaudel, A., Benítez, G. C., Cuevas, E., Fröhlich, M., Galbally, I. E., Molloy, S., Kubistin, D., Lu, X., McClure-Begley, A., Nédélec, P., O'Brien, J., Oltmans, S. J., Petropavlovskikh, I., Ries, L., Senik, I., ... Xu, X. (2020). Multi-decadal surface ozone trends at globally distributed remote locations. *Elementa*, 8(23). <https://doi.org/10.1525/elementa.420>
- Custódio, D., Borrego, C., & Relvas, H. (2022). Worldwide Evaluation of CAMS-EGG4 CO2 Data Re-Analysis at the Surface Level. *Toxics*, 10(6). <https://doi.org/10.3390/toxics10060331>
- D'Adamo, F., Ogutu, B., Brandt, M., Schurgers, G., & Dash, J. (2021). Climatic and non-climatic vegetation cover changes in the rangelands of Africa. *Global and Planetary Change*, 202. <https://doi.org/10.1016/j.gloplacha.2021.103516>
- Dameris, M. (2010). Climate change and atmospheric chemistry: How will the stratospheric ozone layer develop? In *Angewandte Chemie - International Edition* (Vol. 49, Issue 44, pp. 8092–8102). <https://doi.org/10.1002/anie.201001643>
- de Graaf, M., Tilstra, L. G., Aben, I., & Stammes, P. (2010). Satellite observations of the seasonal cycles of absorbing aerosols in Africa related to the monsoon rainfall, 1995-2008. *Atmospheric Environment*, 44(10), 1274–1283. <https://doi.org/10.1016/j.atmosenv.2009.12.038>

- deMenocal, P. B. (2004). African climate change and faunal evolution during the Pliocene-Pleistocene. *Earth and Planetary Science Letters*, 220(1–2), 3–24. [https://doi.org/10.1016/S0012-821X\(04\)00003-2](https://doi.org/10.1016/S0012-821X(04)00003-2)
- Denjean, C., Bourrienne, T., Burnet, F., Mallet, M., Maury, N., Colomb, A., Dominutti, P., Brito, J., Dupuy, R., Sellegri, K., Schwarzenboeck, A., Flamant, C., & Knippertz, P. (2020). Overview of aerosol optical properties over southern West Africa from DACCWA aircraft measurements. *Atmospheric Chemistry and Physics*, 20(8), 4735–4756. <https://doi.org/10.5194/acp-20-4735-2020>
- Dietmuller, S., Garny, H., Eichinger, R., & T. Ball, W. (2021). Analysis of recent lower-stratospheric ozone trends in chemistry climate models. *Atmospheric Chemistry and Physics*, 21(9), 6811–6837. <https://doi.org/10.5194/acp-21-6811-2021>
- Donmez, C., Sahingoz, M., Paul, C., Cilek, A., Hoffmann, C., Berberoglu, S., Webber, H., & Helming, K. (2024). Climate change causes spatial shifts in the productivity of agricultural long-term field experiments. *European Journal of Agronomy*, 155, 127121. <https://doi.org/10.1016/j.eja.2024.127121>
- Dubovik, O., Holben, B. N., Lapyonok, T., Sinyuk, A., Mishchenko, M. I., Yang, P., & Slutsker, I. (2002). Non-spherical aerosol retrieval method employing light scattering by spheroids. *Geophysical Research Letters*, 29(10), 54-1-54–4. <https://doi.org/10.1029/2001gl014506>
- Duveiller, G., Caporaso, L., Abad-Viñas, R., Perugini, L., Grassi, G., Arneth, A., & Cescatti, A. (2020). Local biophysical effects of land use and land cover change: towards an assessment tool for policy makers. *Land Use Policy*, 91. <https://doi.org/10.1016/j.landusepol.2019.104382>
- ECD-GJRC. (2017). *Normalised Difference Vegetation Index 1998-2020 (raster 1 km), global, 10-daily - version 2*. https://globalland.vito.be/geonetwork/srv/api/records/clms_global_ndvi_1km_v2_10daily
- ECD-GJRC. (2021). *Normalised Difference Vegetation Index 2020-present (raster 300 m), global, 10-daily - version 2*. https://globalland.vito.be/geonetwork/srv/api/records/clms_global_ndvi_300m_v2_10daily
- EEA. (2024, December 5). *What is the current state of the ozone layer?* European Environment Agency. <https://www.eea.europa.eu/en/topics/in-depth/climate-change-mitigation-reducing-emissions/current-state-of-the-ozone-layer>
- EPA. (2024, June 27). *Climate Change Indicators: Atmospheric Concentrations of Greenhouse Gases*. United States Environmental Protection Agency. <https://www.epa.gov/climate-indicators/climate-change-indicators-atmospheric-concentrations-greenhouse-gases>
- Ernst, Y., Archibald, S., Balzter, H., Chevallier, F., Ciais, P., Fischer, C. G., Gaubert, B., Higginbottom, T., Higgins, S., Lawal, S., Lacroix, F., Lauerwald, R., Lourenco, M.,

- Martens, C., Mengistu, A. G., Merbold, L., Mitchard, E., Moyo, M., Nguyen, H., ... Scholes, R. J. (2024). The African Regional Greenhouse Gases Budget (2010–2019). *Global Biogeochemical Cycles*, 38(4). <https://doi.org/10.1029/2023GB008016>
- Fang, X., Pyle, J. A., Chipperfield, M. P., Daniel, J. S., Park, S., & Prinn, R. G. (2019). Challenges for the recovery of the ozone layer. In *Nature Geoscience* (Vol. 12, Issue 8, pp. 592–596). Nature Publishing Group. <https://doi.org/10.1038/s41561-019-0422-7>
- Farman, J. C., Gardiner, B. G., & Shanklin, J. D. (1985). Large Losses of total ozone in Antarctica reveal seasonal ClO_x/NO_x interation. *Nature Publishing Group*.
- Fisher, S., Bellinger, D. C., Cropper, M. L., Kumar, P., Binagwaho, A., Koudenoukpo, J. B., Park, Y., Taghian, G., & Landrigan, P. J. (2021). Air pollution and development in Africa: impacts on health, the economy, and human capital. *The Lancet Planetary Health*, 5(10), e681–e688. [https://doi.org/10.1016/S2542-5196\(21\)00201-1](https://doi.org/10.1016/S2542-5196(21)00201-1)
- Fuster, B., Sánchez-Zapero, J., Camacho, F., García-Santos, V., Verger, A., Lacaze, R., Weiss, M., Baret, F., & Smets, B. (2020). Quality assessment of PROBA-V LAI, fAPAR and fCOVER collection 300 m products of copernicus global land service. *Remote Sensing*, 12(6). <https://doi.org/10.3390/rs12061017>
- Gaiduk, A., Yorulmaz, M., Ruijgrok, P. V., & Orrit, M. (2010). Room-temperature detection of a single molecule's absorption by photothermal contrast. *Science*, 330(6002), 353–356. <https://doi.org/10.1126/science.1195475>
- Garland, R. M., Bopape, M.-J., Matooane, M., & Engelbrecht, F. (2014). Projections of heat waves and health impacts in Africa in a changing climate. In S. Piketh, J. Malherbe, M. Josipovic, M. Rouault, S. Venkataraman, C. Wright, & R. Burger (Eds.), *30th Annual conference of South African Society for Atmospheric Sciences - Modeling and Observing the* (pp. 40–44). South African Society for Atmospheric Sciences.
- Garrigues, S., Remy, S., Chimot, J., Ades, M., Inness, A., Flemming, J., Kipling, Z., Laszlo, I., Benedetti, A., Ribas, R., Jafariserajehlou, S., Fougnie, B., Kondragunta, S., Engelen, R., Peuch, V. H., Parrington, M., Bousserez, N., Navarro, M. V., & Agustí-Panareda, A. (2022). Monitoring multiple satellite aerosol optical depth (AOD) products within the Copernicus Atmosphere Monitoring Service (CAMS) data assimilation system. *Atmospheric Chemistry and Physics*, 22(22), 14657–14692. <https://doi.org/10.5194/acp-22-14657-2022>
- Gasse, F. (2000). *Hydrological changes in the African tropics since the Last Glacial Maximum*.
- Gbetibouo, G. A., Hassan, R. M., & Ringler, C. (2010). Modelling farmers' adaptation strategies for climate change and variability: The case of the Limpopo Basin, South Africa. *Agrekon*, 49(2), 217–234. <https://doi.org/10.1080/03031853.2010.491294>
- Gogoi, P. P., Vinoj, V., Swain, D., Roberts, G., Dash, J., & Tripathy, S. (2019). Land use and land cover change effect on surface temperature over Eastern India. *Scientific Reports*, 9(1). <https://doi.org/10.1038/s41598-019-45213-z>

- Goudie, A. S. (2005). The drainage of Africa since the Cretaceous. *Geomorphology*, 67(3–4), 437–456. <https://doi.org/10.1016/j.geomorph.2004.11.008>
- Han, H., Liu, J., Yuan, H., Zhuang, B., Zhu, Y., Wu, Y., Yan, Y., & Ding, A. (2018). Characteristics of intercontinental transport of tropospheric ozone from Africa to Asia. *Atmospheric Chemistry and Physics*, 18(6), 4251–4276. <https://doi.org/10.5194/acp-18-4251-2018>
- Hannaford, M. J., & Nash, D. J. (2016). Climate, history, society over the last millennium in southeast Africa. In *Wiley Interdisciplinary Reviews: Climate Change* (Vol. 7, Issue 3, pp. 370–392). Wiley-Blackwell. <https://doi.org/10.1002/wcc.389>
- Hansen, J. E., Sato, M., Lacis, A., Ruedy, R., Tegen, I., & Matthews, E. (1998). *Perspective Climate forcings in the Industrial era* (Vol. 95). www.pnas.org.
- Haywood, J. (2016). Atmospheric Aerosols and Their Role in Climate Change. In *Climate Change: Observed Impacts on Planet Earth: Second Edition* (pp. 449–463). Elsevier Inc. <https://doi.org/10.1016/B978-0-444-63524-2.00027-0>
- Haywood, J. (2021). Atmospheric aerosols and their role in climate change. In *Climate Change* (pp. 645–659). Elsevier. <https://doi.org/10.1016/B978-0-12-821575-3.00030-X>
- Held, I. M., & Soden, B. J. (2006). *Robust Responses of the Hydrological Cycle to Global Warming*.
- Henderson, J. V., Storeygard, A., & Deichmann, U. (2017). Has climate change driven urbanization in Africa? *Journal of Development Economics*, 124, 60–82. <https://doi.org/10.1016/j.jdeveco.2016.09.001>
- Herrmann, S. M., Brandt, M., Rasmussen, K., & Fensholt, R. (2020). Accelerating land cover change in West Africa over four decades as population pressure increased. *Communications Earth and Environment*, 1(1). <https://doi.org/10.1038/s43247-020-00053-y>
- Hoffman, P. F., Kaufman, A. J., Halverson, G. P., & Schrag, D. P. (1998). A Neoproterozoic Snowball Earth. *SCIENCE*, 281.
- Holmgren, K., & Öberg, H. (2006). Climate change in southern and eastern Africa during the past millennium and its implications for societal development. In *Environment, Development and Sustainability* (Vol. 8, Issue 1, pp. 185–195). <https://doi.org/10.1007/s10668-005-5752-5>
- Huffman, G. J., Adler, R. F., Behrangi, A., Bolvin, D. T., Nelkin, E. J., Guojun, G. U., & Ehsani, M. R. (2023). The New Version 3.2 Global Precipitation Climatology Project (GPCP) Monthly and Daily Precipitation Products. *Journal of Climate*, 36(21), 7635–7655. <https://doi.org/10.1175/JCLI-D-23-0123.1>

- Huffman, G. J., Adler, R. F., Morrissey, M. M., Bolvin, D. T., Curtis, S., Joyce, R., McGavock, B., And, #, & Susskind, J. (2001). *Global Precipitation at One-Degree Daily Resolution from Multisatellite Observations*.
- Huffman, G. J., Behrangi, A., Adler, R. F., Bolvin, D. T., Nelkin, E. J., Song, Y., & Wang, J.-J. (2021). *The Global Precipitation Climatology Project Version 3 Products*. <https://doi.org/10.5194/egusphere-egu21-8468>
- Huijnen, V., Williams, J., Bouarar, I., Belamari, S., Chabrillat, S., Remy, S., & Flemming, J. (2021). *Recent updates to the atmospheric chemistry modeling of the ECMWF IFS in support to CAMS*. <https://doi.org/10.5194/egusphere-egu21-2481>
- Hulme, M., Doherty, R., Ngara, T., New, M., & Lister, D. (2001). *African climate change: 1900–2100*. <http://www.cru.uea.ac.uk>
- Inness, A., Ades, M., Agustí-Panareda, A., Barré, J., Benedictow, A., Blechschmidt, A.-M., Dominguez, J. J., Engelen, R., Eskes, H., Flemming, J., Huijnen, V., Jones, L., Kipling, Z., Massart, S., Parrington, M., Peuch, V.-H., Razinger, M., Remy, S., Schulz, M., & Suttie, M. (2018). *The CAMS reanalysis of atmospheric composition*. <https://doi.org/10.5194/acp-2018-1078>
- Inness, A., Ades, M., Agustí-Panareda, A., Barré, J., Benedictow, A., Blechschmidt, A.-M., Dominguez, J. J., Engelen, R., Eskes, H., Flemming, J., Huijnen, V., Jones, L., Kipling, Z., Massart, S., Parrington, M., Peuch, V.-H., Razinger, M., Remy, S., Schulz, M., & Suttie, M. (2019). The CAMS reanalysis of atmospheric composition. *Atmospheric Chemistry and Physics*, 19(6), 3515–3556. <https://doi.org/10.5194/acp-19-3515-2019>
- IPCC. (2021). *Climate Change 2021: The Physical Science Basis*. (V. Masson-Delmotte, P. Zhai, A. Pirani, S. L. Connors, C. Péan, Y. Chen, L. Goldfarb, M. I. Gomis, J. B. R. Matthews, S. Berger, M. Huang, O. Yelekçi, R. Yu, B. Zhou, E. Lonnoy, T. K. Maycock, T. Waterfield, K. Leitzell, & N. Caud, Eds.). Cambridge University Press.
- Jenkins, G. S., Adamou, G., & Fongang, S. (2002). *THE CHALLENGES OF MODELING CLIMATE VARIABILITY AND CHANGE IN WEST AFRICA*.
- Johnson, T. C., & Odada, E. O. (2019). *The Limnology, Climatology and Paleoclimatology of the East African Lakes; Edition 1*. <https://doi.org/10.4324/9780203748978>
- Kalisa, W., Igbawua, T., Henchiri, M., Ali, S., Zhang, S., Bai, Y., & Zhang, J. (2019). Assessment of climate impact on vegetation dynamics over East Africa from 1982 to 2015. *Scientific Reports*, 9(1). <https://doi.org/10.1038/s41598-019-53150-0>
- Kiage, L. M., Liu, K. B., Walker, N. D., Lam, N., & Huh, O. K. (2007). Recent land-cover/use change associated with land degradation in the Lake Baringo catchment, Kenya, East Africa: Evidence from Landsat TM and ETM+. *International Journal of Remote Sensing*, 28(19), 4285–4309. <https://doi.org/10.1080/01431160701241753>

- Kotir, J. H. (2011). Climate change and variability in Sub-Saharan Africa: a review of current and future trends and impacts on agriculture and food security. *Environment, Development and Sustainability*, 13(3), 587–605. <https://doi.org/10.1007/s10668-010-9278-0>
- Kremser, S., Thomason, L. W., von Hobe, M., Hermann, M., Deshler, T., Timmreck, C., Toohey, M., Stenke, A., Schwarz, J. P., Weigel, R., Fueglistaler, S., Prata, F. J., Vernier, J. P., Schlager, H., Barnes, J. E., Antuña-Marrero, J. C., Fairlie, D., Palm, M., Mahieu, E., ... Meland, B. (2016). Stratospheric aerosol—Observations, processes, and impact on climate. In *Reviews of Geophysics* (Vol. 54, Issue 2, pp. 278–335). Blackwell Publishing Ltd. <https://doi.org/10.1002/2015RG000511>
- Kruger, A. C., & Shongwe, S. (2004). Temperature trends in South Africa: 1960-2003. *International Journal of Climatology*, 24(15), 1929–1945. <https://doi.org/10.1002/joc.1096>
- Laban, T. L., Van Zyl, P. G., Beukes, J. P., Mikkonen, S., Santana, L., Josipovic, M., Vakkari, V., Thompson, A. M., Kulmala, M., & Laakso, L. (2020). Statistical analysis of factors driving surface ozone variability over continental South Africa. *Journal of Integrative Environmental Sciences*, 17(3), 1–28. <https://doi.org/10.1080/1943815X.2020.1768550>
- Lambin, E. F., Geist, H. J., & Lepers, E. (2003). Dynamics of land-use and land-cover change in tropical regions. *Annual Review of Environment and Resources*, 28, 205–241. <https://doi.org/10.1146/annurev.energy.28.050302.105459>
- Langematz, U. (2018). Future ozone in a changing climate. *Comptes Rendus - Geoscience*, 350(7), 403–409. <https://doi.org/10.1016/j.crte.2018.06.015>
- Leah Laban, T., Gideon Van Zyl, P., Paul Beukes, J., Vakkari, V., Jaars, K., Borduas-Dedekind, N., Josipovic, M., Mee Thompson, A., Kulmala, M., & Laakso, L. (2018). Seasonal influences on surface ozone variability in continental South Africa and implications for air quality. *Atmospheric Chemistry and Physics*, 18(20), 15491–15514. <https://doi.org/10.5194/acp-18-15491-2018>
- León-Tavares, J., Roujean, J. L., Smets, B., Wolters, E., Toté, C., & Swinnen, E. (2021). Correction of directional effects in vegetation ndvi time-series. *Remote Sensing*, 13(6). <https://doi.org/10.3390/rs13061130>
- Li, M., Cao, S., Zhu, Z., Wang, Z., Myneni, R. B., & Piao, S. (2023). Spatiotemporally consistent global dataset of the GIMMS Normalized Difference Vegetation Index (PKU GIMMS NDVI) from 1982 to 2022. *Earth System Science Data*, 15(9), 4181–4203. <https://doi.org/10.5194/essd-15-4181-2023>
- Li, Y., Chipperfield, M. P., Feng, W., Dhomse, S. S., Pope, R. J., Li, F., & Guo, D. (2020). Analysis and attribution of total column ozone changes over the Tibetan Plateau during 1979-2017. In *Atmospheric Chemistry and Physics* (Vol. 20, Issue 14, pp. 8627–8639). Copernicus GmbH. <https://doi.org/10.5194/acp-20-8627-2020>

- Lindsey Valich. (2019, June 13). *Ice core data confirms increased tropospheric ozone levels since industrialization*. University of Rochester - Science & Technology. <https://www.rochester.edu/newscenter/new-ice-core-data-tropospheric-ozone-levels-386572/>
- López-Ballesteros, A., Beck, J., Bombelli, A., Grieco, E., Lorencová, E. K., Merbold, L., Brümmer, C., Hugo, W., Scholes, R., Vačkář, D., Vermeulen, A., Acosta, M., Butterbach-Bahl, K., Helmschrot, J., Kim, D. G., Jones, M., Jorch, V., Pavelka, M., Skjelvan, I., & Saunders, M. (2018). Towards a feasible and representative pan-African research infrastructure network for GHG observations. *Environmental Research Letters*, *13*(8). <https://doi.org/10.1088/1748-9326/aad66c>
- Lu, X., Zhang, L., & Shen, L. (2019). Meteorology and Climate Influences on Tropospheric Ozone: a Review of Natural Sources, Chemistry, and Transport Patterns. In *Current Pollution Reports* (Vol. 5, Issue 4, pp. 238–260). Springer. <https://doi.org/10.1007/s40726-019-00118-3>
- Lyu, X., Li, K., Guo, H., Morawska, L., Zhou, B., Zeren, Y., Jiang, F., Chen, C., Goldstein, A. H., Xu, X., Wang, T., Lu, X., Zhu, T., Querol, X., Chatani, S., Latif, M. T., Schuch, D., Sinha, V., Kumar, P., ... Blake, D. R. (2023). A synergistic ozone-climate control to address emerging ozone pollution challenges. In *One Earth* (Vol. 6, Issue 8, pp. 964–977). Cell Press. <https://doi.org/10.1016/j.oneear.2023.07.004>
- Mahmood, R., Pielke, R. A., & McAlpine, C. A. (2016). Climate-relevant land use and land cover change policies. In *Bulletin of the American Meteorological Society* (Vol. 97, Issue 2, pp. 195–202). American Meteorological Society. <https://doi.org/10.1175/BAMS-D-14-00221.1>
- Manatsa, D., & Mukwada, G. (2019). Spring ozone's connection to south africa's temperature and rainfall. *Frontiers in Earth Science*, *7*, 1–16. <https://doi.org/10.3389/feart.2019.00027>
- Marcott, S. A., Shakun, J. D., Clark, P. U., & Mix, A. C. (2013). A reconstruction of regional and global temperature for the past 11,300 years. *Science*, *339*(6124), 1198–1201. <https://doi.org/10.1126/science.1228026>
- Marinou, E., Amiridis, V., Biniotoglou, I., Tsikerdekis, A., Solomos, S., Proestakis, E., Konsta, Di., Papagiannopoulos, N., Tsekeri, A., Vlastou, G., Zanis, P., Balis, Di., Wandinger, U., & Ansmann, A. (2017). Three-dimensional evolution of Saharan dust transport towards Europe based on a 9-year EARLINET-optimized CALIPSO dataset. *Atmospheric Chemistry and Physics*, *17*(9), 5893–5919. <https://doi.org/10.5194/acp-17-5893-2017>
- Marufu, L., Dentener, F., Lelieveld, J., Andreae, M. O., & Helas, G. (2000). Photochemistry of the African troposphere: Influence of biomass-burning emissions. *Journal of Geophysical Research Atmospheres*, *105*(D11), 14513–14530. <https://doi.org/10.1029/1999JD901055>
- Matsuki, A., Quennehen, B., Schwarzenboeck, A., Crumeyrolle, S., Venzac, H., Laj, P., & Gomes, L. (2010). Temporal and vertical variations of aerosol physical and chemical

- properties over West Africa: AMMA aircraft campaign in summer 2006. *Atmospheric Chemistry and Physics*, 10(17), 8437–8451. <https://doi.org/10.5194/acp-10-8437-2010>
- Mccann, J. C. (1999). *CLIMATE AND CAUSATION IN AFRICAN HISTORY* (Vol. 32, Issue 3).
- Meul, S., Langematz, U., Kröger, P., Oberländer-Hayn, S., & Jöckel, P. (2018). Future changes in the stratosphere-to-troposphere ozone mass flux and the contribution from climate change and ozone recovery. *Atmospheric Chemistry and Physics*, 18(10), 7721–7738. <https://doi.org/10.5194/acp-18-7721-2018>
- Meul, S., Oberländer-Hayn, S., Abalichin, J., & Langematz, U. (2015). Nonlinear response of modelled stratospheric ozone to changes in greenhouse gases and ozone depleting substances in the recent past. *Atmospheric Chemistry and Physics*, 15(12), 6897–6911. <https://doi.org/10.5194/acp-15-6897-2015>
- Michigan State University. (n.d.). *Land Use Change*. Global Change Learning Lab in Sub-Saharan Africa. Retrieved January 9, 2025, from <http://globalchangescience.org/eastafricanode/index.php/challenges/land-use-change/>
- Mills, G., Harmens, H., Wagg, S., Sharps, K., Hayes, F., Fowler, D., Sutton, M., & Davies, B. (2016). Ozone impacts on vegetation in a nitrogen enriched and changing climate. *Environmental Pollution*, 208, 898–908. <https://doi.org/10.1016/j.envpol.2015.09.038>
- Minganti, D., Chabrilat, S., Christophe, Y., Errera, Q., Abalos, M., Prignon, M., E. Kinnison, D., & Mahieu, E. (2020). Climatological impact of the Brewer-Dobson circulation on the N₂O budget in WACCM, a chemical reanalysis and a CTM driven by four dynamical reanalyses. *Atmospheric Chemistry and Physics*, 20(21), 12609–12631. <https://doi.org/10.5194/acp-20-12609-2020>
- Mogonong, B. P., Twine, W., Feig, G. T., Van der Merwe, H., & Fisher, J. T. (2024). Influences of Climate Variability on Land Use and Land Cover Change in Rural South Africa. *Remote Sensing*, 16(7). <https://doi.org/10.3390/rs16071200>
- Monarrez, R. (2021). *Sounder SIPS CLIMCAPS Level-3 Products User Guide NASA CLIMCAPS Level 3 Data Product User Guide: File Format and Definition* (Version 2). NASA Goddard Space Flight Center.
- Moore, N., Andresen, J., Lofgren, B., Pijanowski, B., & Kim, D. Y. (2015). Projected land-cover change effects on East African rainfall under climate change. *International Journal of Climatology*, 35(8), 1772–1783. <https://doi.org/10.1002/joc.4117>
- Muthoni, F. K., Odongo, V. O., Ochieng, J., Mugalavai, E. M., Mourice, S. K., Hoesche-Zeledon, I., Mwila, M., & Bekunda, M. (2019). Long-term spatial-temporal trends and variability of rainfall over Eastern and Southern Africa. *Theoretical and Applied Climatology*, 137(3–4), 1869–1882. <https://doi.org/10.1007/s00704-018-2712-1>
- NASA. (n.d.). *World of Change: Antarctic Ozone Hole*. Earth Observatory. Retrieved January 8, 2025, from <https://earthobservatory.nasa.gov/world-of-change/Ozone>

- Neukom, R., Barboza, L. A., Erb, M. P., Shi, F., Emile-Geay, J., Evans, M. N., Franke, J., Kaufman, D. S., Lücke, L., Rehfeld, K., Schurer, A., Zhu, F., Brönnimann, S., Hakim, G. J., Henley, B. J., Ljungqvist, F. C., McKay, N., Valler, V., & von Gunten, L. (2019). Consistent multidecadal variability in global temperature reconstructions and simulations over the Common Era. *Nature Geoscience*, *12*(8), 643–649. <https://doi.org/10.1038/s41561-019-0400-0>
- Niang, I., Ruppel, O. C., Abdrabo, M. A., Essel, A. , L. C., Padgham, J., & Urquhart, P. (2014). Africa. In *Climate Change 2014: Impacts, Adaptation, and Vulnerability. Part B: Regional Aspects. Contribution of Working Group II to the Fifth Assessment Report of the Intergovernmental Panel on Climate Change*. In *Aissa Toure Sarr*. Pieter Pauw.
- Nicholson, S. (2000). Land surface processes and Sahel climate. In *Reviews of Geophysics* (Vol. 38, Issue 1, pp. 117–139). Blackwell Publishing Ltd. <https://doi.org/10.1029/1999RG900014>
- Nicholson, S. E. (2000). The nature of rainfall variability over Africa on time scales of decades to millenia. In *Global and Planetary Change* (Vol. 26). www.elsevier.com/locate/gloplacha
- Nicholson, S. E. (2001a). *Climatic and environmental change in Africa during the last two centuries*.
- Nicholson, S. E. (2001b). *Climatic and environmental change in Africa during the last two centuries*.
- NICHOLSON, S. E. (2019). A Review of Climate Dynamics and Climate Variability in Eastern Africa . In T. C. Johnson, E. O. Odada, & K. T. Whittaker (Eds.), *Limnology, Climatology and Paleoclimatology of the East African Lakes* (pp. 25–56).
- Nicholson, S. E., & Flohn, H. (1980). *AFRICAN ENVIRONMENTAL AND CLIMATIC CHANGES AND THE GENERAL ATMOSPHERIC CIRCULATION IN LATE PLEISTOCENE AND HOLOCENE*.
- Nicholson, S. E., Nash, D. J., Chase, B. M., Grab, S. W., Shanahan, T. M., Verschuren, D., Asrat, A., Lézine, A. M., & Umer, M. (2013). Temperature variability over Africa during the last 2000 years. *Holocene*, *23*(8), 1085–1094. <https://doi.org/10.1177/0959683613483618>
- Nielsen, J., & Reenberg, A. (2010). Temporality and the problem with singling out climate as a current driver of change in a small West African village. *Journal of Arid Environments*, *74*(4), 464–474. <https://doi.org/10.1016/j.jaridenv.2009.09.019>
- Nooni, I. K., Ogou, F. K., Prempeh, N. A., Saidou Chaibou, A. A., Hagan, D. F. T., Jin, Z., & Lu, J. (2024). Analysis of Long-Term Vegetation Trends and Their Climatic Driving Factors in Equatorial Africa. *Forests*, *15*(7). <https://doi.org/10.3390/f15071129>
- Nzabarinda, V., Bao, A., Xu, W., Uwamahoro, S., Jiang, L., Duan, Y., Nahayo, L., Yu, T., Wang, T., & Long, G. (2021). Assessment and evaluation of the response of vegetation dynamics

- to climate variability in Africa. *Sustainability (Switzerland)*, *13*(3), 1–22. <https://doi.org/10.3390/su13031234>
- Ofori, S. A., Cobbina, S. J., & Obiri, S. (2021). Climate Change, Land, Water, and Food Security: Perspectives From Sub-Saharan Africa. In *Frontiers in Sustainable Food Systems* (Vol. 5). Frontiers Media S.A. <https://doi.org/10.3389/fsufs.2021.680924>
- Ogunjo, S., Fuwape, I., Rabi, B., Oluyamo, S., & Owoola, E. (2019). Assessing the impact of vegetation cover on total column ozone over west Africa. In *Advances in Science, Technology and Innovation* (pp. 231–233). Springer Nature. https://doi.org/10.1007/978-3-030-01440-7_54
- Oluleye, A., & Okogbue, E. C. (2013). Analysis of temporal and spatial variability of total column ozone over West Africa using daily TOMS measurements. *Atmospheric Pollution Research*, *4*(4), 387–397. <https://doi.org/10.5094/APR.2013.044>
- Ongoma, V., & Chen, H. (2017). Temporal and spatial variability of temperature and precipitation over East Africa from 1951 to 2010. *Meteorology and Atmospheric Physics*, *129*(2), 131–144. <https://doi.org/10.1007/s00703-016-0462-0>
- Orlov, A., Aunan, K., Mistry, M. N., Lejeune, Q., Pongratz, J., Thiery, W., Gasparri, A., Reed, E. U., & Schleussner, C. F. (2023). Neglected implications of land-use and land-cover changes on the climate-health nexus. *Environmental Research Letters*, *18*(6). <https://doi.org/10.1088/1748-9326/acd799>
- Prospero, J. M., Ginoux, P., Torres, O., Nicholson, S. E., & Gill, T. E. (2002). Environmental characterization of global sources of atmospheric soil dust identified with the Nimbus 7 Total Ozone Mapping Spectrometer (TOMS) absorbing aerosol product. *Reviews of Geophysics*, *40*(1), 2-1-2–31. <https://doi.org/10.1029/2000RG000095>
- Ramanathan, V., Callis, L., Cess, R., Hansen, J., Isaksen, I., Kuhn, W., Lacis, A., Luther, F., Mahlman, J., Reck, L. E., And, T. M., & Schlesinger, M. (1987). Climate-Chemical Interactions and Effects of Changing Atmospheric Trace Gases. In *REVIEWS OF GEOPHYSICS* (Vol. 25, Issue 7).
- Ramanathan, V., & Feng, Y. (2009). Air pollution, greenhouse gases and climate change: Global and regional perspectives. *Atmospheric Environment*, *43*(1), 37–50. <https://doi.org/10.1016/j.atmosenv.2008.09.063>
- Ravishankara, A. R., Daniel, J. S., & Portmann, R. W. (2009). Nitrous oxide (N₂O): The dominant ozone-depleting substance emitted in the 21st century. *Science*, *326*(5949), 123–125. <https://doi.org/10.1126/science.1176985>
- Riebsame, W. E., Meyer, W. B., & Ii, B. L. T. (n.d.). *MODELING LAND USE AND COVER AS PART OF GLOBAL ENVIRONMENTAL CHANGE*.
- Royer, D. L., Berner, R. A., & Park, J. (2007). Climate sensitivity constrained by CO₂ concentrations over the past 420 million years. *Nature*, *446*(7135), 530–532. <https://doi.org/10.1038/nature05699>

- Rupakheti, D., Kang, S., Rupakheti, M., Tripathee, L., Zhang, Q., Chen, P., & Yin, X. (2018a). Long-term trends in the total columns of ozone and its precursor gases derived from satellite measurements during 2004–2015 over three different regions in South Asia: Indo-Gangetic Plain, Himalayas and Tibetan Plateau. *International Journal of Remote Sensing*, 39(21), 7384–7404. <https://doi.org/10.1080/01431161.2018.1470699>
- Rupakheti, D., Kang, S., Rupakheti, M., Tripathee, L., Zhang, Q., Chen, P., & Yin, X. (2018b). Long-term trends in the total columns of ozone and its precursor gases derived from satellite measurements during 2004–2015 over three different regions in South Asia: Indo-Gangetic Plain, Himalayas and Tibetan Plateau. *International Journal of Remote Sensing*, 39(21), 7384–7404. <https://doi.org/10.1080/01431161.2018.1470699>
- Salata, S. (2021). The utilization of supervised classification sampling for environmental monitoring in turin (Italy). *Sustainability (Switzerland)*, 13(5), 1–20. <https://doi.org/10.3390/su13052494>
- Salazar, A., Baldi, G., Hirota, M., Syktus, J., & McAlpine, C. (2015). Land use and land cover change impacts on the regional climate of non-Amazonian South America: A review. In *Global and Planetary Change* (Vol. 128, pp. 103–119). Elsevier. <https://doi.org/10.1016/j.gloplacha.2015.02.009>
- Sanogo, S., Fink, A. H., Omotosho, J. A., Ba, A., Redl, R., & Ermert, V. (2015). Spatio-temporal characteristics of the recent rainfall recovery in West Africa. *International Journal of Climatology*, 35(15), 4589–4605. <https://doi.org/10.1002/joc.4309>
- Saunio, M., R. Stavert, A., Poulter, B., Bousquet, P., G. Canadell, J., B. Jackson, R., A. Raymond, P., J. Dlugokencky, E., Houweling, S., K. Patra, P., Ciais, P., K. Arora, V., Bastviken, D., Bergamaschi, P., R. Blake, D., Brailsford, G., Bruhwiler, L., M. Carlson, K., Carrol, M., ... Zhuang, Q. (2020). The global methane budget 2000-2017. *Earth System Science Data*, 12(3), 1561–1623. <https://doi.org/10.5194/essd-12-1561-2020>
- Saunio, M., Reeves, C. E., Mari, C. H., Murphy, J. G., Stewart, D. J., Mills, G. P., Oram, D. E., & Purvis, R. M. (2009). Factors controlling the distribution of ozone in the West African lower troposphere during the AMMA (African Monsoon Multidisciplinary Analysis) wet season campaign. In *Atmos. Chem. Phys* (Vol. 9). www.atmos-chem-phys.net/9/6135/2009/
- Savi, F., Nemitz, E., Coyle, M., Aitkenhead, M., Frumau, K., Gerosa, G., Finco, A., Gruening, C., Goded, I., Loubet, B., Stella, P., Ruuskanen, T., Weidinger, T., Horvath, L., Zenone, T., & Fares, S. (2020). Neural Network Analysis to Evaluate Ozone Damage to Vegetation Under Different Climatic Conditions. *Frontiers in Forests and Global Change*, 3. <https://doi.org/10.3389/ffgc.2020.00042>
- Scholz, C. A., Johnson, T. C., Cohen, A. S., King, J. W., Peck, J. A., Overpeck, J. T., Talbot, M. R., Brown, E. T., Kalindegafe, L., Amoako, P. Y. O., Lyons, R. P., Shanahan, T. M., Castañeda, I. S., Heil, C. W., Forman, S. L., Mchargue, L. R., Beuning, K. R., Gomez, J., &

- Pierson, J. (2007). *East African megadroughts between 135 and 75 thousand years ago and bearing on early-modern human origins*. www.pnas.org/cgi/content/full/
- Seviour, W. J. M., Butchart, N., & Hardiman, S. C. (2012). The Brewer-Dobson circulation inferred from ERA-Interim. *Quarterly Journal of the Royal Meteorological Society*, *138*(665), 878–888. <https://doi.org/10.1002/qj.966>
- Sievers, G. L. (1978). Weighted rank statistics for simple linear regression. *Journal of the American Statistical Association*, *73*(363), 628–631. <https://doi.org/10.1080/01621459.1978.10480067>
- Sigmond, M., Polvani, L. M., Fyfe, J. C., Smith, C. J., Cole, J. N. S., & England, M. R. (2023). Large Contribution of Ozone-Depleting Substances to Global and Arctic Warming in the Late 20th Century. *Geophysical Research Letters*, *50*(5). <https://doi.org/10.1029/2022GL100563>
- Simpson, D., Arneth, A., Mills, G., Solberg, S., & Uddling, J. (2014). Ozone - the persistent menace: Interactions with the N cycle and climate change. *Current Opinion in Environmental Sustainability*, *9–10*, 9–19. <https://doi.org/10.1016/j.cosust.2014.07.008>
- Smith, N., & Barnet, C. D. (2019). Uncertainty characterization and propagation in the Community Long-Term Infrared Microwave Combined Atmospheric Product System (CLIMCAPS). *Remote Sensing*, *11*(10). <https://doi.org/10.3390/rs11101227>
- Solomon, S. (1999). Stratospheric ozone depletion: A review of concepts and history. In *Reviews of Geophysics* (Vol. 37, Issue 3, pp. 275–316). Blackwell Publishing Ltd. <https://doi.org/10.1029/1999RG900008>
- Spadoni, G. L., Cavalli, A., Congedo, L., & Munafò, M. (2020). Analysis of Normalized Difference Vegetation Index (NDVI) multi-temporal series for the production of forest cartography. *Remote Sensing Applications: Society and Environment*, *20*. <https://doi.org/10.1016/j.rsase.2020.100419>
- Staehelin, J., Viatte, P., Stübi, R., Tummon, F., & Peter, T. (2018). Stratospheric ozone measurements at Arosa (Switzerland): History and scientific relevance. *Atmospheric Chemistry and Physics*, *18*(9), 6567–6584. <https://doi.org/10.5194/acp-18-6567-2018>
- Stanley, S. M., & Luczaj, J. A. (2014). *Earth System History* (4th ed.). Katherine Parker.
- Stenchikov, G. (2021). The role of volcanic activity in climate and global changes. In *Climate Change* (pp. 607–643). Elsevier. <https://doi.org/10.1016/B978-0-12-821575-3.00029-3>
- Sultan, B., & Janicot, S. (2003). *The West African Monsoon Dynamics. Part I: Documentation of Intraseasonal Variability* (Vol. 16, Issue 21).
- Summerhayes, C. P. . (2015). *Earth's evolving climate: A geological perspective*. Hoboken, NJ : Wiley-Blackwell : Published in association with the Scott Polar Research Institute.
- Tadic, I., Nussbaumer, C. M., Bohn, B., Harder, H., Marno, D., Martinez, M., Obersteiner, F., Parchatka, U., Pozzer, A., Rohloff, R., Zöger, M., Lelieveld, J., & Fischer, H. (2021).

- Central role of nitric oxide in ozone production in the upper tropical troposphere over the Atlantic Ocean and western Africa. *Atmospheric Chemistry and Physics*, 21(10), 8195–8211. <https://doi.org/10.5194/acp-21-8195-2021>
- Taupin, F. G., Beekmann, M., Brémaud, P. J., & Randriambelo, T. (2002). *Annales Geophysicae Ozone generation over the Indian Ocean during the South African biomass-burning period: case study of October 1992* (Vol. 20). European Geophysical Society.
- Thompson, D. W. J., Solomon, S., Kushner, P. J., England, M. H., Grise, K. M., & Karoly, D. J. (2011). Signatures of the Antarctic ozone hole in Southern Hemisphere surface climate change. In *Nature Geoscience* (Vol. 4, Issue 11, pp. 741–749). <https://doi.org/10.1038/ngeo1296>
- Tongwane, M. I., & Moeletsi, M. E. (2018). A review of greenhouse gas emissions from the agriculture sector in Africa. In *Agricultural Systems* (Vol. 166, pp. 124–134). Elsevier Ltd. <https://doi.org/10.1016/j.agsy.2018.08.011>
- Trenberth, K. E., Dai, A., Rasmussen, R. M., & Parsons, D. B. (2003). THE CHANGING CHARACTER OF PRECIPITATION. *AMERICAN METEOROLOGICAL SOCIETY*, 1205–1218.
- Trenberth, K. E., Stepaniak, D. P., & Caron, J. M. (2000). *The Global Monsoon as Seen through the Divergent Atmospheric Circulation*.
- Tucker, C. J. (1979). Red and Photographic Infrared Linear Combinations for Monitoring Vegetation. In *REMOTE SENSING OF ENVIRONMENT* (Vol. 8).
- Tuckett, R. (2021). Greenhouse gases and the emerging climate emergency. In *Climate Change* (pp. 19–45). Elsevier. <https://doi.org/10.1016/B978-0-12-821575-3.00002-5>
- Tyson, P. O. (1993). Recent developments in the modelling of the future climate of southern Africa. In *REVIEW ARTICLES South African Journal of Science* (Vol. 89).
- Vakkari, V., Beukes, J. P., Laakso, H., Mabaso, D., Pienaar, J. J., Kulmala, M., & Laakso, L. (2013). Long-term observations of aerosol size distributions in semi-clean and polluted savannah in South Africa. *Atmospheric Chemistry and Physics*, 13(4), 1751–1770. <https://doi.org/10.5194/acp-13-1751-2013>
- Vannest, K. J., Parker, R. I., Davis, J. L., Soares, D. A., & Smith, S. L. (2012). *The Theil-Sen Slope for High-Stakes Decisions from Progress Monitoring*. <http://www.studentpro->
- Verger, A., Baret, F., Weiss, M., Filella, I., & Peñuelas, J. (2015). GEOCLIM: A global climatology of LAI, FAPAR, and FCOVER from VEGETATION observations for 1999–2010. *Remote Sensing of Environment*, 166, 126–137. <https://doi.org/10.1016/j.rse.2015.05.027>
- Wagner, A., Bennouna, Y., Blechschmidt, A. M., Brasseur, G., Chabrillat, S., Christophe, Y., Errera, Q., Eskes, H., Flemming, J., Hansen, K. M., Inness, A., Kapsomenakis, J., Langerock, B., Richter, A., Sudarchikova, N., Thouret, V., & Zerefos, C. (2021).

- Comprehensive evaluation of the Copernicus Atmosphere Monitoring Service (CAMS) reanalysis against independent observations: Reactive gases. *Elementa*, 9(1). <https://doi.org/10.1525/elementa.2020.00171>
- Wang, F., Shao, W., Yu, H., Kan, G., He, X., Zhang, D., Ren, M., & Wang, G. (2020). Re-evaluation of the Power of the Mann-Kendall Test for Detecting Monotonic Trends in Hydrometeorological Time Series. *Frontiers in Earth Science*, 8. <https://doi.org/10.3389/feart.2020.00014>
- Wang, Y., Ma, Y. F., Eskes, H., Inness, A., Flemming, J., & Brasseur, G. P. (2020). Evaluation of the CAMS global atmospheric trace gas reanalysis 2003-2016 using aircraft campaign observations. *Atmospheric Chemistry and Physics*, 20(7), 4493–4521. <https://doi.org/10.5194/acp-20-4493-2020>
- Wang, Y., Ma, Y.-F., Eskes, H., Inness, A., Flemming, J., & Brasseur, G. P. (2019). *Evaluation of the CAMS global atmospheric trace gas reanalysis 2003–2016 using aircraft campaign observations*. <https://doi.org/10.5194/acp-2019-821>
- Wang, Y., Yuan, Q., Li, T., Yang, Y., Zhou, S., & Zhang, L. (2023). Seamless mapping of long-term (2010-2020) daily global XCO₂ and XCH₄ from the Greenhouse Gases Observing Satellite (GOSAT), Orbiting Carbon Observatory 2 (OCO-2), and CAMS global greenhouse gas reanalysis (CAMS-EGG4) with a spatiotemporally self-supervised fusion method. *Earth System Science Data*, 15(8), 3597–3622. <https://doi.org/10.5194/essd-15-3597-2023>
- Xiao, H., Liu, J., He, G., Zhang, X., Wang, H., Long, T., Zhang, Z., Wang, W., Yin, R., Guo, Y., Cheng, B., & Cao, Q. (2022). Data-Driven Forest Cover Change and Its Driving Factors Analysis in Africa. *Frontiers in Environmental Science*, 9. <https://doi.org/10.3389/fenvs.2021.780069>
- Xu, M., Zhang, Z., Wang, Y., & Liu, B. (2023). Quantifying the contributions of climatic and human factors to vegetation net primary productivity dynamics in East Africa. *Frontiers in Forests and Global Change*, 6. <https://doi.org/10.3389/ffgc.2023.1332631>
- Zeng, G., Morgenstern, O., Williams, J. H. T., O'Connor, F. M., Griffiths, P. T., Keeble, J., Deushi, M., Horowitz, L. W., Naik, V., Emmons, L. K., Abraham, N. L., Archibald, A. T., Bauer, S. E., Hassler, B., Michou, M., Mills, M. J., Murray, L. T., Oshima, N., Sentman, L. T., ... Young, P. J. (2022). Attribution of Stratospheric and Tropospheric Ozone Changes Between 1850 and 2014 in CMIP6 Models. *Journal of Geophysical Research: Atmospheres*, 127(16). <https://doi.org/10.1029/2022JD036452>
- Zhang, J., Tian, W., Xie, F., Sang, W., Guo, D., Chipperfield, M., Feng, W., & Hu, D. (2019). Zonally asymmetric trends of winter total column ozone in the northern middle latitudes. *Climate Dynamics*, 52(7–8), 4483–4500. <https://doi.org/10.1007/s00382-018-4393-y>
- Zhang, X. (2015). Reconstruction of a complete global time series of daily vegetation index trajectory from long-term AVHRR data. *Remote Sensing of Environment*, 156, 457–472. <https://doi.org/10.1016/j.rse.2014.10.012>

- Zhang, Y., Cooper, O. R., Gaudel, A., Thompson, A. M., Nédélec, P., Ogino, S. Y., & West, J. J. (2016). Tropospheric ozone change from 1980 to 2010 dominated by equatorward redistribution of emissions. *Nature Geoscience*, 9(12), 875–879. <https://doi.org/10.1038/ngeo2827>
- Zhang, Y., West, J. J., Emmons, L. K., Flemming, J., Jonson, J. E., Lund, M. T., Sekiya, T., Sudo, K., Gaudel, A., Chang, K. L., Nédélec, P., & Thouret, V. (2021). Contributions of World Regions to the Global Tropospheric Ozone Burden Change From 1980 to 2010. *Geophysical Research Letters*, 48(1). <https://doi.org/10.1029/2020GL089184>
- Zhou, P., Wen, Y., Yang, J., Yang, L., Liang, M., Wen, T., & Cai, S. (2022). Spatiotemporal Variation, Driving Mechanism and Predictive Study of Total Column Ozone: A Case Study in the Yangtze River Delta Urban Agglomerations. *Remote Sensing*, 14(18). <https://doi.org/10.3390/rs14184576>
- Zhou, X., Yue, X., Tian, C., & Lu, X. (2024). Global assessment of climatic responses to ozone–vegetation interactions. *Atmospheric Chemistry and Physics*, 24(17), 9923–9937. <https://doi.org/10.5194/acp-24-9923-2024>
- Zougrana, B. J. B., Conrad, C., Amekudzi, L. K., Thiel, M., Da, E. D., Forkuor, G., & Löw, F. (2015). Multi-temporal landsat images and ancillary data for land use/cover change (LULCC) detection in the Southwest of Burkina Faso, West Africa. *Remote Sensing*, 7(9), 12076–12102. <https://doi.org/10.3390/rs70912076>